R.R. Hartmann and M.E. Portnoi
Optoelectronic Properties of Carbon-based Nanostructures:
Steering electrons in graphene by electromagnetic fields
(LAP LAMBERT Academic Publishing, Saarbrücken, 2011)
ISBN-10: 3844328580
ISBN-13: 978-3844328585

Contents

List of Figures

Chapter 1

Introduction

There are several allotropes of carbon, the specific crystallographic structure of each allotropic form leads to drastically different electronic and optical properties. For example, diamond is one of the hardest materials known to man, it is the best naturally occurring thermal conductor and an excellent electronic insulator. In contrast, graphite is opaque, conducting, utilized as a thermal insulator and one of the softest materials known to man. These two allotropes, as well as amorphous carbon, more commonly known as coal, are perhaps the most well known naturally occurring three-dimensional forms of carbon.

Carbon's ability to exist in many different forms is due to the fact that carbon's four valence electrons may hybridize in many ways. This hybridization may be sp, sp^2or sp^3 allowing carbon to form linear chains, planar sheets and tetrahedral structures. sp^2 bonded carbon can form a honeycomb crystal lattice, one atom thick, known as graphene. This one atom thick sheet of carbon is the building block of many carbon allotropes. When these layers are stacked on top of one another they can weakly bond via Van der Waals forces to form graphite; they can be rolled into a seamless cylinder to form carbon nanotubes (CNTs), or fashioned into buckyballs. sp^2 bonded carbon therefore spans the entire spectrum of dimensional kinetics. Of the aforementioned sp^2 bonded forms, only graphite occurs naturally. This mineral was found to be a highly effective writing medium, since its weakly coupled layers easily shear away from one another, so arguably graphene has been fabricated for many years, perhaps by the tips of many a physicists' pencil. For the method of simply rubbing graphite onto any surface is sufficient to produce graphene. The other dimensional forms of sp^2 bonded carbon i.e., the fullerenes (zero dimensional) and carbon nanotubes (one dimensional) are man-made and the recent isolation of graphene [1] completed the full set of dimensional forms of carbon.

This thesis will focus on a diverse range of problems related to the optical and electronic prop-

erties of carbon-based nanostructures. In chapter 2 optical transitions within the frame of a simple nearest-neighbor, orthogonal, π-electron tight-binding model are studied for graphene. This model leads to the discovery of momentum alignment in graphene. Namely, a linearly polarized excitation is shown to create a strongly anisotropic distribution of photoexcited carriers in graphene, where the momenta of photoexcited carriers are aligned preferentially normal to the polarization plane. Hence, one can effectively steer the direction of electrons in graphene by light. The applications of being able to generate highly directional photoexcited carriers are discussed. The depolarization of hot photoluminescence (HPL) is used to study relaxation processes in both free standing graphene and graphene grown epitaxially on silicon carbide. Extending this analysis to include the effect of a magnetic field allows one to obtain the momentum relaxation times of hot electrons. The analysis of momentum alignment in the high frequency regime shows that a linearly polarized excitation allows the spatial separation of carriers belonging to different valleys, therefore opening the door to an optical means of controlling valley polarization (optovalleytronics) and quantum computing in graphene.

In chapter 3 the analysis of optical transitions is extended to one dimensional systems formed from rolled graphene i.e., carbon nanotubes. It is shown how the intrinsic curvature and electric fields can modify the optical selection rules of quasi-metallic carbon nanotubes; making them ideal candidates for the building blocks of terahertz devices. Numerous devices for terahertz emitters and detectors are proposed for both one and two dimensional forms of graphene. The exciton binding energy in narrow-gaps carbon nanotubes is calculated. It is shown that the exciton binding energy scales with the band gap and vanishes as the gap decreases, even for strong electron-hole attraction. Therefore, excitonic effects, including strongly bound dark excitons, which explain the poor electroluminescent properties of semiconducting nanotubes, should not dominate for narrow-gap carbon nanotubes. This opens the possibility of using quasi-metallic carbon nanotubes for various terahertz applications.

There is a widespread belief that the electrostatic confinement of graphene charge carriers, which resemble massless Dirac fermions, is impossible as a result of the Klein paradox. This is often considered a major obstacle to the realization of graphene-based electronic devices. In chapter 4 it is shown that full confinement is indeed possible for zero-energy states in pristine graphene due to the density of states vanishing at the charge neutrality point. An exact analytical solution, a rare breed in twenty first century physics, is found for fully confined modes in a smooth model potential, which provides a good fit to existing top-gate graphene structures. This exact analytical solution reveals a simple relationship between the number of modes within the potential and the product of the potential strength and width. In striking contrast to the non-relativistic Schrödinger

equation, there is a threshold for the appearance of the first bound mode in a symmetric potential. This opens a route to graphene-based devices with high on/off current ratio. The observation of quantized channel conductance should be possible up to room temperature in experimentally attainable electrostatically defined channels.

Chapter 2

Steering electrons in graphene by light

2.1 Introduction

Graphene was first produced by the simple method of mechanical exfoliation: using Scotch tape to peel away stacks of graphene from graphite, which are in turn subdivided down to a single layer of graphene. The flakes are then transferred to a clean substrate by pressing the tape against the substrate [1, 2]. This technique has been refined such that samples of high crystallinity can be made with lengths greater than one hundred micrometers. Despite the simplicity of fabrication, the two-dimensional form of carbon proved to be the most elusive to isolate. The problem lied within isolating an atomically thick sheet. How exactly does one see something only one atom thick? Using techniques such as electron beam microscopy, Raman spectroscopy [3] and atomic force microscopy [1] to find a flake on a substrate are akin to finding a needle in a haystack due to their small read sizes and slow raster speeds. Geim's coup was to use the interference effects between a graphene-$Si0_2$-Si multi-layer to discriminate between single layers of graphene using an optical microscope and the power of the naked eye. This is essentially a multi-layer reflection problem, by using Fresnel theory the contrast can be maximized for a variety of insulator thicknesses and wavelengths [4, 5].

The Weber contrast is defined as $(I_g - I)/I$, where I is the intensity of light observed from the bare substrate and I_g is the intensity of light in the presence of the flake. To make graphene visible one must design the geometry so as to maximize $I_g - I$ and minimize I. This was first achieved by placing a 300nm thick layer of $Si0_2$ between graphene and a silicon substrate. The oxide layer acts as a Fabry-Pérot cavity, such that when light is transmitted resonantly, reflection

is minimized; thereby enhancing optical contrast. Despite only being one atom thick, graphene can absorb 2.4% of incident light [6], this coupled with the change in optical path per layer is sufficient to make graphene visible and create a sufficiently large difference in the interference color between layers of different thicknesses. The most commonly used configuration is a 300nm layer of SiO_2 on top of a Si substrate, in this geometry a 12% contrast is attainable for light of wavelength 550nm [5]. This optical contrast technique has also been implemented to isolate graphene flakes on 50 nm Si_3N_4 using blue light and on 90 nm Poly(methyl methacrylate) using white light [5, 7] as well 72 nm Al_20_3 on a Si wafer [8].

The discovery of graphene by Geim created a proverbial gold rush in both experimental and theoretical fields of semiconductor physics. Though the physical discovery of graphene is a recent one, theoretically this material has been studied for over 60 years in order to understand the properties of its host material, from where it is extracted, graphite [9]. Despite graphene's band structure being well known, it was never considered as a material in its own right, only ever as a sub-component of a bigger crystal. This was partly due to the fact that it was widely believed that any two-dimensional crystal would succumb to thermal fluctuations, thereby destroying any long range order [10, 11].

Unlike conventional systems, whose charge carriers are described by the Schrödinger equation with effective mass, graphene's charge carriers are described by the same equation used to describe two dimensional massless Dirac-fermions, the Dirac-Weyls equation. This opens the door to a rich and fascinating area of physics, the ability to study particles which behave in a quasi-relativistic manner, without the need for exotic conditions or particle accelerators i.e., relativity at sub-light speeds [12, 13]. The consequence of this unusual spectrum is that many effects which were once the realms of high-energy particle physics are now measurable in a solid state system [14, 15].

Graphene exhibits unusual mechanical, thermal and, most of all, electronic properties [13] which allows the observation of interesting effects such as the suppression of backscattering [16], an unconventional quantum Hall effect [12, 17] and a range of effects based on the Klein paradox [14]. One of the trends in graphene research is the study of graphene single and multiple p-n junctions [18, 19, 20, 21, 22, 23, 24]. In such structures the particle properties are dictated by their momentum orientation with respect to the junction, which results in an extremely strong angular dependence of the tunneling probability [18, 25]. However, transport measurements are strongly influenced by contacts, sample geometry and disorder [13]. Therefore it would be beneficial for the study of Klein-paradox-related phenomena to find a way of creating a highly directional distribution of carriers close to the barrier; in this chapter such a method is proposed using linearly polarized light.

Optical properties of graphene have been a subject of extensive research, indeed they helped to isolate graphene flakes in the first instance [4, 5]. Notably, most of the theoretical work deals with either non-polarized or circularly polarized light for both optical and infrared [26] excitation. As we show below a linearly polarized excitation results in strong momentum anisotropy for all excitation energies. Not only can this optically-induced anisotropy be used to create highly directional beams of photoexcited carriers but it also provides a new method to study carrier relaxation in graphene.

The depolarization of hot photoluminescence (HPL) has been used with great success to study relaxation processes in conventional 2D systems [27]. In such systems the alignment is due to the spin-orbit interaction for photoexcited holes [28], whereas in graphene it is due to the pseudo-spin. Namely, the ratio of the two components of the spinor-like graphene wavefunction depends on momentum which influences the optical transition selection rules. Unlike conventional semiconductors, where most optical phenomena are associated with the band edge transitions, photoexcited carriers in graphene are always created with a significant value of momentum. Therefore the momentum alignment phenomena, which was important in conventional semiconductors for the study of hot photoluminescence, becomes essential for graphene, where all optical transitions occur for non-zero momentum. By comparing the depolarization from successive phonon replicas, the mechanisms for phonon relaxation in graphene can be studied. Furthermore, studying the depolarization of HPL in a magnetic field (the Hanle effect) allows one to obtain momentum relaxation times of hot electrons. The effect of momentum alignment in graphene provides a contact-free method of characterizing energy and momentum relaxation.

The conduction and valence bands in graphene touch each other at six points, which lie on the edge of the first Brillouin zone. In pristine, undoped graphene the Fermi surface coincides with these points (known as Dirac points) and at these points the dispersion relation is linear [9]. Two of these points are inequivalent and degenerate in terms of energy. This degree of degeneracy is the so-called valley degree of freedom. It has been proposed that this additional quantum number can be utilized in an analogous manner to spin in semiconductor spintronics [29]. Controlling the valley degree of freedom has been dubbed valley electronics or "valleytronics" and it has been suggested as a basis for carrying information in graphene based devices [30]; providing a method of controlling valley polarization is practically realized. Previous proposals for separating carriers belonging to different valleys are based either on the use of p-n junctions in conjunction with the trigonal warping effect [31, 32] or on edge-related effects in graphene nanoribbons [30, 33, 34]. Both methods have certain difficulties in practical realization, namely the p-n junction based methods require extremely high gate voltages and the nanoribbon-based method needs precise control over the edge type. Our analysis of momentum alignment in the high frequency regime shows that this

phenomenon provides a route to optovalleytronics - the optical control of valley population.

In what follows the background theory is introduced and the energy dispersion is derived using the tight binding method. Next, the selection rules for the interband transitions caused by a linearly polarized excitation are derived. The resulting distribution of photoexcited carriers is calculated for both the low energy regime and for the range in which trigonal warping effects become important. The distribution function obtained in the low energy regime is used to calculate the degree of depolarization of the HPL. This analysis is extended to include the influence of a magnetic field on the depolarization of the HPL. Finally, it is shown that in the presence of warping a linearly polarized excitation will result in the spatial separation of carriers belonging to different valleys.

2.2 Background theory : Graphene

2.2.1 Introduction

In this section, the tight binding method is used to derive the band structure of graphene. We shall see how the symmetry of graphene's lattice results in its charge carriers being described by the Dirac-Weyl equation, the very same equation which describes the motion of two-dimensional massless Dirac fermions. Knowledge of both the tight-binding Hamiltonian and its wave functions are essential for calculating both the optical and electronic properties of graphene.

2.2.2 Graphene's crystallographic structure

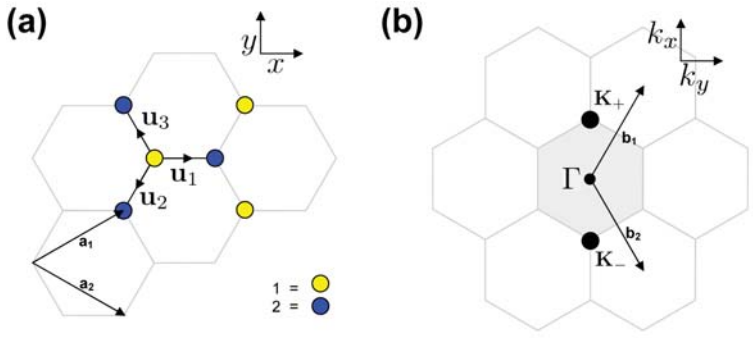

Figure 2.1: (a) The crystallographic structure of graphene ($\mathbf{a_1}$ and $\mathbf{a_2}$ are the lattice unit vectors, and $\mathbf{u}_i$, i=1,2,3 are the nearest neighbor vectors). (b) Graphene's Brillouin zone. $\mathbf{b_1}$ and $\mathbf{b_2}$ are the reciprocal lattice vectors.

Graphene is formed by carbon atoms arranged in a honeycomb crystal lattice as shown in Fig. 2.1. The carbon atom's $2s$, $2p_x$ and $2p_y$ orbitals form σ bonds to their nearest neighbors, these bonds determine the crystal's structural properties. The remaining $2p_z$ orbitals hybridize to form weaker, more delocalized π bonds and these dictate the optical and transport properties of

the material.

Graphene's primitive lattice vectors are given by

$$\mathbf{a_1} = \left(\frac{\sqrt{3}}{2}a, \frac{1}{2}a\right); \qquad \mathbf{a_2} = \left(\frac{\sqrt{3}}{2}a, -\frac{1}{2}a\right), \tag{2.1}$$

where $|\mathbf{a_1}| = |\mathbf{a_2}| = \sqrt{3}a_{CC}$, a_{CC} is the nearest neighbor distance between two carbon atoms which is given as 1.42 Å. The corresponding reciprocal lattice vectors are given by

$$\mathbf{b_1} = \left(\frac{2\pi}{\sqrt{3}a}, \frac{2\pi}{a}\right); \qquad \mathbf{b_2} = \left(\frac{2\pi}{\sqrt{3}a}, -\frac{2\pi}{a}\right) \tag{2.2}$$

and form a hexagonal Brillouin zone as shown in Fig. 2.1 . The high symmetry points shall be referred to as the $\mathbf{K}_+$ and $\mathbf{K}_-$ points and are given by

$$\mathbf{K}_+ = \left(0, \frac{4\pi}{3a}\right); \qquad \mathbf{K}_- = \left(0, -\frac{4\pi}{3a}\right).$$

2.2.3 The tight binding method

Graphene's lattice can be thought of as two overlapping triangular sub-lattices, each one formed by its two inequivalent sets of atoms. These atoms are inequivalent in the sense that a lattice vector cannot map one onto another. Since no lattice vector can translate a type "1" atom to a type "2" atom graphene's electronic wavefunction, ψ, must be constructed from two individual Bloch functions:

$$\psi\left(\mathbf{k}, \mathbf{r}\right) = \sum_{j=1}^{2} C_j\left(\mathbf{k}\right) \Phi_j\left(\mathbf{k}, \mathbf{r}\right), \tag{2.3}$$

where C_j are coefficients to be determined and j denotes the sublattice. The tight binding Bloch functions $\Phi_j\left(\mathbf{k}, \mathbf{r}\right)$ are composed from a linear combination of atomic orbitals φ, which are the $2p_z$ atomic wavefunctions of the carbon atoms located at positions $\mathbf{R}_j$ (where $\mathbf{R}_j$ is a lattice vector). The atomic orbitals, φ, are normalized functions and are assumed to be orthogonal, highly localized functions such that

$$\int \varphi^\star\left(r - \mathbf{R}_j\right) \varphi\left(r - \mathbf{R}_{j'}\right) d^3\mathbf{r} = \delta_{jj'}. \tag{2.4}$$

Note: all results obtained herein can be generalized for the case of an overlap integral matrix, Eq (2.4), containing non-diagonal terms which results in electron-hole asymmetry [13].

The tight binding Bloch functions are given by,

$$\Phi_j(\mathbf{k},\mathbf{r}) = \frac{1}{\sqrt{N}} \sum_{\mathbf{R}_j} e^{i(\mathbf{k}\cdot\mathbf{R}_j)} \varphi(\mathbf{r}-\mathbf{R}_j), \tag{2.5}$$

where N is the number of unit cells in the solid [35]. The sum is performed over all lattice vectors and each atomic orbital is weighted by the phase factor $e^{i(\mathbf{k}\cdot\mathbf{R}_j)}$. Note, for brevity from here on in $\varphi(\mathbf{r}-\mathbf{R}_j)$ shall be referred to as $\varphi(\mathbf{R}_j)$. The wave functions satisfies the Bloch condition:

$$\Phi_j(\mathbf{k},\mathbf{r}+\mathbf{R}) = e^{i(\mathbf{k}\cdot\mathbf{R})}\Phi_j(\mathbf{k},\mathbf{r}), \tag{2.6}$$

where $\mathbf{R} = n\mathbf{a_1} + m\mathbf{a_2}$ and n and m are are any integers (assuming that the lattice is infinite).

$$\begin{aligned}\Phi_j(\mathbf{k},\mathbf{r}+\mathbf{R}) &= \tfrac{1}{\sqrt{N}} \textstyle\sum_{\mathbf{R}_j} e^{i(\mathbf{k}\cdot\mathbf{R}_j)} \varphi(\mathbf{r}+\mathbf{R}-\mathbf{R}_j), \\ &= \tfrac{1}{\sqrt{N}} e^{i(\mathbf{k}\cdot\mathbf{R})} \textstyle\sum_{\mathbf{R}_j} e^{i(\mathbf{k}\cdot(\mathbf{R}_j-\mathbf{R}))} \varphi(\mathbf{r}-(\mathbf{R}_j-\mathbf{R})), \\ &= e^{i(\mathbf{k}\cdot\mathbf{R})}\Phi_j(\mathbf{k},\mathbf{r}).\end{aligned} \tag{2.7}$$

The Born-Von Karman boundary condition, which imposes that the wavefunction must be periodic at any given lattice site is given by

$$\Phi_j(\mathbf{k},\mathbf{r}+\mathbf{R}) = \Phi_j(\mathbf{k},\mathbf{r}). \tag{2.8}$$

Therefore the wave vector, $\mathbf{k}$, is quantized according to

$$k_i = \frac{2\pi}{N_i |\mathbf{a_i}|} p. \tag{2.9}$$

Here, N_i is the total number of carbon atoms along the direction defined by the unit vector $\mathbf{a_i}$ and p is an integer ranging from zero to $N_i - 1$. In this thesis all systems under consideration will be sufficiently large such that one may consider the wave vector, $\mathbf{k}$, as a continuous variable.

2.2.4 The band structure of graphene

To derive the electronic band structure of graphene's π orbitals, we must solve the time independent Schrödinger equation

$$\hat{\mathcal{H}}\psi = E\psi. \tag{2.10}$$

Here ψ is the tight binding wave function of graphene given in Eq. (2.3) and $\hat{\mathcal{H}}$ is Hamiltonian which describes the quantum mechanical hopping of an electron on a planar honeycomb [36]

$$\hat{\mathcal{H}} = t\sum_{\mathbf{R}_1}\sum_{i=1}^{3} a^{\dagger}\left(\mathbf{r}-\mathbf{R}_1\right) b\left(\mathbf{r}-\mathbf{R}_1+\mathbf{u}_i\right) + t\sum_{\mathbf{R}_2}\sum_{i=1}^{3} b^{\dagger}\left(\mathbf{r}-\mathbf{R}_2\right) a\left(\mathbf{r}-\mathbf{R}_2+\mathbf{v}_i\right). \tag{2.11}$$

Here, $t \approx -3\text{eV}$ is the hopping amplitude and is related to the Fermi velocity by

$$v_{\mathrm{F}} = \frac{\sqrt{3}}{2}\frac{a\,|t|}{\hbar}. \tag{2.12}$$

$a^{\dagger}\left(b^{\dagger}\right)$ and $a(b)$ are the creation and annihilation operators acting on sub-lattice 1 (2) . $\mathbf{u}_i(\mathbf{v}_i)$ are the triad of nearest neighbor vectors connecting a carbon atom from sub-lattice 1 (2) to its three nearest neighbors from sub-lattice 2 (1). By symmetry $\mathbf{u}_i = -\mathbf{v}_i$ where,

$$\mathbf{u}_i = \left(\frac{a}{\sqrt{3}}, 0\right), \left(-\frac{a}{2\sqrt{3}}, -\frac{a}{2}\right), \left(-\frac{a}{2\sqrt{3}}, \frac{a}{2}\right). \tag{2.13}$$

The tight-binding Hamiltonian has the following properties:

$$\begin{gathered}\left\langle \varphi\left(\mathbf{R}_1\right)\left|\hat{\mathcal{H}}\right|\varphi\left(\mathbf{R}_1+\mathbf{u}_i\right)\right\rangle = t;\\ \left\langle \varphi\left(\mathbf{R}_2\right)\left|\hat{\mathcal{H}}\right|\varphi\left(\mathbf{R}_2+\mathbf{v}_i\right)\right\rangle = t;\\ \left\langle \varphi\left(\mathbf{R}_j\right)\left|\hat{\mathcal{H}}\right|\varphi\left(\mathbf{R}_j\right)\right\rangle = \epsilon_0,\end{gathered} \tag{2.14}$$

where ϵ_0 is the on site energy. Substituting Eq. (2.3) into Eq. (2.10) yields,

$$\hat{\mathcal{H}}\sum_{j,\mathbf{R}_j} C_j e^{i(\mathbf{k}\cdot\mathbf{R}_j)}\varphi\left(\mathbf{R}_j\right) = E\sum_{j,\mathbf{R}_j} C_j e^{i(\mathbf{k}\cdot\mathbf{R}_j)}\varphi\left(\mathbf{R}_j\right). \tag{2.15}$$

The energy eigenvalues can be found by multiplying Eq. (2.10) by the complex conjugate of the basis Bloch function Eq. (2.5), followed by the integration over all real space, this yields

$$\sum_{j,j',\mathbf{R}_j,\mathbf{R}_{j'}} C_j e^{i\left[\mathbf{k}\cdot\left(\mathbf{R}_j-\mathbf{R}_{j'}\right)\right]}\left\langle \varphi\left(\mathbf{R}_{j'}\right)\left|\hat{\mathcal{H}}\right|\varphi\left(\mathbf{R}_j\right)\right\rangle = E\sum_{j,j',\mathbf{R}_j,\mathbf{R}_{j'}} C_j e^{i\left[\mathbf{k}\cdot\left(\mathbf{R}_j-\mathbf{R}_{j'}\right)\right]}\left\langle \varphi\left(\mathbf{R}_{j'}\right)\mid\varphi\left(\mathbf{R}_j\right)\right\rangle. \tag{2.16}$$

Due to the exponentially decaying nature of the atomic wavefunctions with distance, one can exclude the contributions in the summation which satisfy the condition $|\mathbf{R}_{j'}-\mathbf{R}_j| > |\mathbf{u}_i|$. Using the properties of the tight-binding matrix Eq. (2.14) and recalling that $\int \varphi^{\star}\left(\mathbf{R}_{j'}\right)\varphi\left(\mathbf{R}_j\right)d^3\mathbf{r} = \delta_{jj'}$ Eq. (2.16) can be reduced to

$$t\begin{bmatrix} 0 & f_k \\ f_k^{\star} & 0 \end{bmatrix}\begin{bmatrix} C_1 \\ C_2 \end{bmatrix} = \xi\begin{bmatrix} C_1 \\ C_2 \end{bmatrix}, \tag{2.17}$$

where $\xi = E - \epsilon_0$ and

$$f_k = \sum_i e^{i\mathbf{k}\cdot\mathbf{u}_i} = e^{i\frac{1}{\sqrt{3}}ak_x} + 2e^{-i\frac{1}{2\sqrt{3}}ak_x}\cos\left(\frac{1}{2}ak_y\right). \tag{2.18}$$

The time independent Schrödinger equation, Eq. (2.10) can therefore be replaced by an effective matrix Hamiltonian, H, whose eigenvectors describe the amplitude of the Bloch functions given in Eq. (2.3):

$$H = -|t| \begin{bmatrix} 0 & f_k \\ f_k^\star & 0 \end{bmatrix}. \tag{2.19}$$

The energy eigenvalues are obtained by solving the secular equation $|H - I\varepsilon| = 0$, where I is the identity matrix. The resulting electron energy spectrum is given by the expression

$$\xi_b = s\,|t|\sqrt{|f_k|^2} = s\,|t|\sqrt{1 + 4\cos\left(\frac{\sqrt{3}}{2}ak_x\right)\cos\left(\frac{1}{2}ak_y\right) + 4\cos^2\left(\frac{1}{2}ak_y\right)}. \tag{2.20}$$

Here the index $b = C, V$ denotes the conduction and valence band respectively and when $b = C$, $s = +$; when $b = V$, $s = -$. The corresponding normalized energy eigenvectors are found to be

$$C^b = \frac{1}{\sqrt{2}} \begin{bmatrix} -s\frac{f_k}{\sqrt{|f_k|^2}} \\ 1 \end{bmatrix}. \tag{2.21}$$

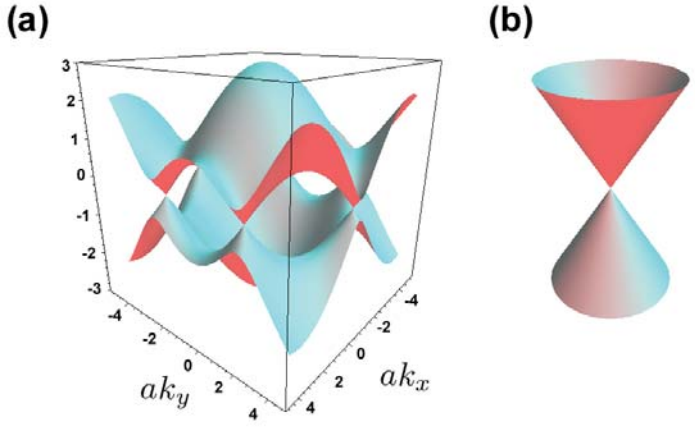

Figure 2.2: (a) Graphene's energy spectrum measured in units of t. (b) The energy spectrum in the vicinity of a Dirac point.

The electron energy dispersion, $\xi(\mathbf{k})$, is plotted in Fig. 2.2. At $\xi(\mathbf{k}) = 0$ the functions Eq. (2.20) coincide with each other exactly at the corners of the Brillouin zone. It is in the vicinity of these points where the most fascinating physics is revealed. These points are also referred to as the "Dirac points" the naming of which will become apparent in the next section.

2.2.4.1 The low energy regime (conical approximation)

In what follows, we shall see that at the high symmetry points the low energy spectrum (i.e. the typical electronic and terahertz regime) is in fact linear. This peculiar band structure gives rise to graphene's novel transport and optical properties.

Graphene's dispersion curve, Eq. (2.20), can be approximated by a Taylor series expansion around the Dirac points $\mathbf{K}_+$ and $\mathbf{K}_-$. Substituting $k_x = q_x$ and $k_y = q_y \pm \frac{4\pi}{3a}$ into Eq. (2.18) and retaining terms up to the first order yields

$$f_k \approx a\frac{\sqrt{3}}{2}\left(\mp q_y + iq_x\right), \tag{2.22}$$

where the plus and minus sign correspond to an expansion about the $\mathbf{K}_+$ and $\mathbf{K}_-$ point respectively. Hence the electron energy spectrum, Eq. (2.20) becomes

$$\xi_b = sa\frac{\sqrt{3}}{2}\left|t\right|\sqrt{q_x^2 + q_y^2}. \tag{2.23}$$

This was first derived by Wallace [9] to explain the transport properties of graphite over 60 years ago. It is evident from the above expression that the dispersion curves form conical shapes centered about the symmetry points $\mathbf{K}_+$ and $\mathbf{K}_-$. It is important to note that graphene's band structure differs from conventional electronic systems in that its dispersion is linear rather than parabolic and it is this linear dispersion which gives rise to graphene novel optical and electronic properties. The constants in Eq. (2.23) can be combined in to a single prefactor; the Fermi velocity, which has an approximate value of $v_F = 10^6\, m/s$. Therefore, in the vicinity of the Dirac points the dispersion relation for graphene has the form

$$\xi_b\left(\mathbf{q}\right) = s\hbar\left|\mathbf{q}\right|v_F = s\left|\mathbf{p}\right|v_F. \tag{2.24}$$

Since graphene's energy is linearly related to its momentum analogies can be drawn with a photon. However, in this instance graphene's electrons are traveling at a speed of 1/300th of the speed of light.

Performing the series expansion of the Hamiltonian, Eq. (2.19), around the symmetry points $\mathbf{K}_+$ and $\mathbf{K}_-$ yields two distinctly different results:

$$H_\pm = a\frac{\sqrt{3}}{2}\left|t\right|\begin{bmatrix} 0 & \pm q_y - iq_x \\ \pm q_y + iq_x & 0 \end{bmatrix}. \tag{2.25}$$

Here the plus and minus sign denotes the result of the Hamiltonian being expanded about the

$\mathbf{K}_+$ and $\mathbf{K}_-$ point respectively. Within this approximation the corresponding eigenvector elements, Eq. (2.21) become

$$C^b = \frac{1}{\sqrt{2}} \begin{bmatrix} s\frac{(\pm q_y - iq_x)}{|\mathbf{q}|} \\ 1 \end{bmatrix}. \tag{2.26}$$

The effective Hamiltonian, Eq. (2.25) can be written in the compact form

$$H_\pm = \hbar v_F \left(\pm\sigma_x q_y + \sigma_y q_x\right), \tag{2.27}$$

where σ_x and σ_y are the Pauli spin matrices given by,

$$\sigma_x = \begin{bmatrix} 0 & 1 \\ 1 & 0 \end{bmatrix}, \quad \sigma_y = \begin{bmatrix} 0 & -i \\ i & 0 \end{bmatrix}. \tag{2.28}$$

Eq. (2.27) can be expressed in operator form as

$$\hat{H}_\pm = \hbar v_F \left(\pm\sigma_x \hat{q}_y + \sigma_y \hat{q}_x\right), \tag{2.29}$$

where $\hat{q}_x = -i\frac{\partial}{\partial x}$ and $\hat{q}_y = -i\frac{\partial}{\partial y}$ and the corresponding eigenvectors are given by

$$C^b = \frac{1}{\sqrt{2}} \begin{bmatrix} s\frac{(\pm q_y - iq_x)}{|\mathbf{q}|} \\ 1 \end{bmatrix} e^{i\mathbf{q}\cdot\mathbf{r}}. \tag{2.30}$$

2.2.4.2 Dirac electrons

By invoking the change of coordinates, $x \to y$ and $y \to x$ the effective Hamiltonian, Eq. (2.29) can be written as

$$\hat{H}_\pm = \hbar v_F \sigma \cdot \hat{\mathbf{q}}, \tag{2.31}$$

where $\sigma = \pm\sigma_x \mathbf{i} + \sigma_y \mathbf{j}$, and the corresponding eigenvectors are given by

$$C^b = \frac{1}{\sqrt{2}} \begin{bmatrix} \pm s e^{\mp i\varphi_q} \\ 1 \end{bmatrix} e^{i\mathbf{q}\cdot\mathbf{r}}. \tag{2.32}$$

In fact Eq. (2.31) is non other than the Dirac-Weyl equation, therefore unlike conventional systems, which are described by the Schrödinger equation with effective mass, graphene's charge carriers are described by the same equation used to describe two dimensional massless Dirac-fermions such as neutrinos. Notably, graphene's spinor-like wavefunction and in particular the

phase relation between it's two components gives rise to many interesting phenomena, which shall be the subject of discussion in the forthcoming sections.

2.3 Selection rules for dipole optical transitions

2.3.1 Introduction

In what follows, the selection rules for interband transitions caused by a linearly polarized excitation are derived, using first order time perturbation theory, within the electric dipole approximation. Next, the distribution of photoexcited carriers is calculated for both the low energy regime and for the range in which trigonal warping effects become important.

2.3.2 Calculating optical transitions: Dipole approximation

Consider a system with a Hamiltonian $\hat{\mathcal{H}}_0$, whose eigenfunctions $|\psi_m\rangle$ satisfy: $\hat{\mathcal{H}}_0 |\psi_m\rangle = \xi_m |\psi_m\rangle$, where $\xi_m = \hbar\omega_m$ and ω_m is the particles angular frequency. At $t = 0$ the system is perturbed such that the new system is described by the Hamiltonian $\hat{\mathcal{H}}_1(t) = \hat{\mathcal{H}}_0 + \hat{\mathcal{H}}'(t)$ where

$$\hat{\mathcal{H}}'(t) = \hat{\mathcal{H}}_+ e^{-i\omega t} \tag{2.33}$$

and ω is the angular frequency of the excitation. The time dependent perturbation causes transitions between states $|\psi_m\rangle$. According to first order time dependent perturbation theory, the transition rate, W_k, of an electron in state $|\psi_i\rangle$ (described by wave vector $\mathbf{k}$) making a direct transition to final state $|\psi_f\rangle$ is

$$W_k = \frac{1}{\hbar^2} \left| \left\langle \psi_f \left| \hat{\mathcal{H}}' \right| \psi_i \right\rangle \right|^2 \frac{1}{\tau} \left\{ \frac{\sin\left[(\omega_f - \omega_i - \omega) \frac{\tau}{2} \right]}{(\omega_f - \omega_i - \omega) \frac{1}{2}} \right\}^2, \tag{2.34}$$

where τ is the time related to the relaxation broadening of optical transitions defined as $\tau \geq 2\pi/\triangle\omega$, where $\triangle\omega$ is the linewidth of the laser. In the limit that τ become large (i.e. a narrow band laser), the Sinc function in Eq. (2.34) can be approximated by a delta function via the relation:

$$\delta(x) = \lim_{\epsilon \to 0} \frac{\epsilon}{\pi} \frac{\sin^2\left(\frac{x}{\epsilon}\right)}{x^2}. \tag{2.35}$$

In this instance the transition rate is given by Fermi's golden rule:

$$W_k = \frac{2\pi}{\hbar} \left| \left\langle \psi_f \left| \hat{\mathcal{H}}' \right| \psi_i \right\rangle \right|^2 \delta(\xi_f - \xi_i - h\nu), \tag{2.36}$$

where ν is the frequency of the excitation.

In what follows we shall derive an expression for $\hat{\mathcal{H}}'$ for the case of an electromagnetic wave (traveling in a vacuum) serving as the time dependent perturbation. We shall assume that this electromagnetic wave will strike the sample at normal incidence (Faraday geometry). The electric and magnetic fields which comprise the electromagnetic wave shall be denoted $\mathbf{E}(\mathbf{r},t)$ and $\mathbf{H}(\mathbf{r},t)$ respectively and are expressed via the magnetic vector potential, $\mathbf{A}(\mathbf{r},t)$, as

$$\mathbf{E}(\mathbf{r},t) = -\frac{1}{c}\frac{\partial \mathbf{A}(\mathbf{r},\mathbf{t})}{\partial t}; \tag{2.37}$$

$$\mathbf{H}(\mathbf{r},t) = \nabla \times \mathbf{A}(\mathbf{r},t). \tag{2.38}$$

For a plane wave, $\mathbf{A}(\mathbf{r},t)$ can be expressed as

$$\mathbf{A} = \mathbf{A}_0 \cos(\mathbf{Q}\cdot\mathbf{r} - \omega t), \tag{2.39}$$

where $\mathbf{Q} = \frac{\omega}{c}\hat{\mathbf{Q}}$ and $\hat{\mathbf{Q}}$ is the unit wave vector of the excitation. $\mathbf{A}_0 = |\mathbf{A}_0|\,\mathbf{e}$, where $\mathbf{e}$ is the unit vector describing the polarization of the electromagnetic wave. In what follows, we will need to be able to express $|\mathbf{A}_0|$ as a function of the intensity of the excitation. Such a relationship can be found via the Poynting vector, which represents the energy flux (energy per unit time per unit area) of an electromagnetic field and is defined as,

$$\mathbf{S}(\mathbf{r},t) = \frac{c}{4\pi}\mathbf{E}\times\mathbf{H}. \tag{2.40}$$

Eqs. (2.37,2.38,2.39,2.40) yield;

$$\mathbf{S}(\mathbf{r},t) = \frac{\omega}{4\pi}\left[\mathbf{Q}(\mathbf{A}_0\cdot\mathbf{A}_0) - \mathbf{A}_0(\mathbf{A}_0\cdot\mathbf{Q})\right]\sin^2(\mathbf{Q}\cdot\mathbf{r}-\omega t). \tag{2.41}$$

Eq. (2.41) can be simplified further. Maxwell's equation for a propagating electromagnetic wave in a vacuum is

$$\nabla\cdot\mathbf{E} = 0. \tag{2.42}$$

Substituting Eq. (2.37) into Eq. (2.42) implies that

$$\nabla\cdot\mathbf{A} = 0. \tag{2.43}$$

It follows from Eq. (2.39) and Eq. (2.43) that $\mathbf{Q}\cdot\mathbf{A}_0$ must also be equal to zero and this allows Eq. (2.41) to be expressed as

$$\mathbf{S}(\mathbf{r},t) = \frac{c}{4\pi}\left(\frac{\omega}{c}\right)^2 |\mathbf{A}_0|^2 \sin^2(\mathbf{Q}\cdot\mathbf{r} - \omega t)\,\hat{\mathbf{Q}}. \tag{2.44}$$

The time averaged power per unit area (i.e. intensity, $I_{\mathbf{e}}$) in the direction of $\mathbf{Q}$ is given by

$$I_{\mathbf{e}} = \langle \mathbf{S}(\mathbf{r},t)\rangle = \frac{c}{8\pi}\left(\frac{\omega}{c}\right)^2 |\mathbf{A}_0|^2 . \tag{2.45}$$

Lets now calculate $\hat{\mathcal{H}}'(t)$ for the electromagnetic wave whose magnetic vector potential is of the form Eq. (2.39). The Hamiltonian of a free electron, $\hat{\mathcal{H}}_0$, is given by

$$\hat{\mathcal{H}}_0 = \frac{1}{2m_0}\hat{\mathbf{p}}^2, \tag{2.46}$$

where $\hat{\mathbf{p}} = -i\hbar\left(\frac{\partial}{\partial x}\mathbf{i} + \frac{\partial}{\partial x}\mathbf{j}\right)$ and m_0 is the mass of the electron. In the presence of an electromagnetic field the particles momentum is modified such that $\mathbf{p} \to \mathbf{p} + \frac{q}{c}\mathbf{A}$, therefore the Hamiltonian Eq. (2.46) becomes,

$$\hat{\mathcal{H}}_1(t) = \hat{\mathcal{H}}_0 + \frac{q}{2m_0 c}(\mathbf{A}\cdot\hat{\mathbf{p}} + \hat{\mathbf{p}}\cdot\mathbf{A}) + \left(\frac{q}{c}\right)^2 \mathbf{A}\cdot\mathbf{A}. \tag{2.47}$$

Making use of the commutator relation $[\mathbf{A}(\mathbf{r}), \hat{\mathbf{p}}] = i\hbar\nabla\cdot\mathbf{A}(\mathbf{r})$ and Eq. (2.43), $\mathbf{A}\cdot\hat{\mathbf{p}}$ must be equivalent to $\hat{\mathbf{p}}\cdot\mathbf{A}$, therefore, Eq. (2.47) can be re-expressed as

$$\hat{\mathcal{H}}_1(t) = \hat{\mathcal{H}}_0 + \frac{q}{m_0 c}(\mathbf{A}\cdot\hat{\mathbf{p}}) + \left(\frac{q}{c}\right)^2 \mathbf{A}\cdot\mathbf{A}. \tag{2.48}$$

Assuming that $\left(\frac{q}{c}\right)^2 \mathbf{A}\cdot\mathbf{A} \ll \frac{q}{m_0 c}(\mathbf{A}\cdot\hat{\mathbf{p}})$ the Hamiltonian can be approximated by:

$$\hat{\mathcal{H}}_1(t) \approx \hat{\mathcal{H}}_0 + \frac{q}{c}\mathbf{A}\cdot\hat{\mathbf{v}}, \tag{2.49}$$

where $\hat{\mathbf{v}}$ is the velocity operator. Eq. (2.49) can be expressed in the form:

$$\hat{\mathcal{H}}_1(t) = \hat{\mathcal{H}}_0 + \hat{\mathcal{H}}_+ e^{-i\omega t} + \hat{\mathcal{H}}_- e^{i\omega t}, \tag{2.50}$$

where

$$\hat{\mathcal{H}}_\pm = \frac{q}{2c}|\mathbf{A}_0|\, e^{\pm i\mathbf{Q}\cdot\mathbf{r}}\mathbf{e}\cdot\hat{\mathbf{v}}. \tag{2.51}$$

Here $\hat{\mathcal{H}}_+$ corresponds to an incoming photon, while $\hat{\mathcal{H}}_-$ corresponds to an outgoing photon. Since we are interested in absorption we shall, from here on in, drop the $\hat{\mathcal{H}}_-$ term from Eq. (2.51).

To simplify the analysis of the optical selection rules we shall consider the long wavelength limit

i.e., $\mathbf{Q}\cdot\mathbf{r} \ll 1$. In this instance we can expand the exponential term, $e^{i\mathbf{Q}\cdot\mathbf{r}}$ appearing in Eq. (2.51):

$$e^{i\mathbf{Q}\cdot\mathbf{r}} \approx 1 + i\frac{\omega}{c}\hat{\mathbf{Q}}\cdot\mathbf{r} + \ldots \tag{2.52}$$

Since $\mathbf{Q}\cdot\mathbf{r} \ll 1$ the exponential term can be approximated by the first term. This approximation is known as the electric dipole approximation and within this approximation, Eq. (2.51) becomes

$$\hat{\mathcal{H}}_+ = \frac{q}{2c}\left|\mathbf{A}_0\right|\mathbf{e}\cdot\hat{\mathbf{v}}. \tag{2.53}$$

Substituting Eq. (2.45), Eq. (2.53) and $q = e$, where e is the charge of an electron, into Eq. (2.36) yields

$$W_k = \frac{2\pi e^2 I_{\mathbf{e}}}{ch\nu^2}\left|\mathbf{e}\cdot\langle\psi_f\left|\hat{\mathbf{v}}\right|\psi_i\rangle\right|^2\delta\left(\xi_f - \xi_i - h\nu\right). \tag{2.54}$$

2.3.3 Selection rules for dipole optical transitions in graphene

Let us now consider optical transitions in graphene within the electric dipole approximation. We shall consider an electron in the valence band with energy ξ_V , making a direct transition into the conduction band, with new energy ξ_C. Here, the electron energies correspond to those found in Eq. (2.20). Let the valence (conduction) band electrons be described by the tight-binding wavefunction given in Eq. (2.3):

$$\psi^V(\mathbf{k},\mathbf{r}) = \sum_{j=1}^{2} C_j^V(\mathbf{k})\,\Phi_j(\mathbf{k},\mathbf{r}), \tag{2.55}$$

$$\psi^C(\mathbf{k},\mathbf{r}) = \sum_{j=1}^{2} C_j^C(\mathbf{k})\,\Phi_j(\mathbf{k},\mathbf{r}); \tag{2.56}$$

where ψ^V (ψ^C) corresponds to the valence (conduction) band wavefunction and the coefficients C_j^b are those given in Eq. (2.21). It has been shown that a simplified, single electron picture is a reasonable description of graphene optics and that many-body effects can be incorporated into a modified parameter in a simple tight-binding model [37].

For graphene, Eq. (2.54) can be written as

$$W_k = \frac{2\pi e^2 I_{\mathbf{e}}}{ch\nu^2}\left|\mathbf{e}\cdot\left\langle\psi^C\left|\hat{\mathbf{v}}\right|\psi^V\right\rangle\right|^2\delta\left(\xi_C - \xi_V - h\nu\right). \tag{2.57}$$

Let us first consider the velocity matrix element, $\left\langle\psi^C\left|\hat{\mathbf{v}}\right|\psi^V\right\rangle$. Using the velocity operator in commutator form $\hat{\mathbf{v}} = \frac{i}{\hbar}\left[\hat{\mathcal{H}},\mathbf{r}\right]$ one can re-express the velocity matrix element as:

$$\frac{i}{\hbar}\left\langle \psi^C \left| \hat{\mathcal{H}}\mathbf{r} \right| \psi^V \right\rangle - \frac{i}{\hbar}\left\langle \psi^C \left| \mathbf{r}\hat{\mathcal{H}} \right| \psi^V \right\rangle. \tag{2.58}$$

The unit operator given by, $\sum_{m\in\mathbb{N}} |\Phi_m\rangle\langle\Phi_m| = \hat{1}$ can be employed to re-cast the above equation in a more convenient form:

$$\sum_{m\in\mathbb{N}} \frac{i}{\hbar}\left\langle \psi^C \left| \hat{\mathcal{H}} \right| \Phi_m \right\rangle \langle \Phi_m |\mathbf{r}| \psi^V \rangle - \frac{i}{\hbar}\langle \psi^C |\mathbf{r}| \Phi_m \rangle \left\langle \Phi_m \left| \hat{\mathcal{H}} \right| \psi^V \right\rangle. \tag{2.59}$$

Here Φ_m are the tight binding Bloch functions given in Eq. (2.5). Substituting Eq. (2.55), Eq. (2.56) and Eq. (2.5) into Eq. (2.59) and treating the atomic orbital wavefunctions as delta functions, i.e. $\langle \varphi(\mathbf{r}-\mathbf{R}_m)|\mathbf{r}|\varphi(\mathbf{r}-\mathbf{R}_n)\rangle = \mathbf{R}_n\delta_{n,m}$, allows Eq. (2.59) to be expressed as

$$\frac{i}{\hbar N}\left[\sum_{j,\mathbf{R}_j} C_j^V \mathbf{R}_j \sum_{j',\mathbf{R}_{j'}} \left(C_{j'}^C\right)^\star e^{i\mathbf{k}\cdot\left(\mathbf{R}_j-\mathbf{R}_{j'}\right)} \left\langle \varphi(\mathbf{R}_{j'}) \left| \hat{\mathcal{H}} \right| \varphi(\mathbf{R}_j) \right\rangle \right.$$

$$\left. - \sum_{j',\mathbf{R}_{j'}} \left(C_{j'}^C\right)^\star \mathbf{R}_{j'} \sum_{j,\mathbf{R}_j} C_j^V e^{i\mathbf{k}\cdot\left(\mathbf{R}_j-\mathbf{R}_{j'}\right)} \left\langle \varphi(\mathbf{R}_{j'}) \left| \hat{\mathcal{H}} \right| \varphi(\mathbf{R}_j) \right\rangle \right]. \tag{2.60}$$

By making use of the properties of the tight-binding Hamiltonian given in Eq. (2.14), Eq. (2.60) becomes

$$i\frac{t}{\hbar}\left[\left(C_1^C\right)^\star C_2^V \sum_{i=1}^{3} e^{i\mathbf{k}\cdot\mathbf{u}_i}\mathbf{u}_i - \left(C_2^C\right)^\star C_1^V \sum_{i=1}^{3} e^{-i\mathbf{k}\cdot\mathbf{u}_i}\mathbf{u}_i\right]. \tag{2.61}$$

Since $\left(C_1^C\right)^\star C_2^V = -\left[\left(C_2^C\right)^\star C_1^V\right]^\star$ the velocity matrix element, Eq (2.61) can be written as:

$$-i\frac{2t}{\hbar}\Re\left[\left(C_2^C\right)^\star C_1^V \sum_{i=1}^{3} e^{-i\mathbf{k}\cdot\mathbf{u}_i}\mathbf{u}_i\right]. \tag{2.62}$$

Eq (2.62) results in the same selection rules as those employed in the treatment of optical transitions in carbon nanotubes [38, 39].

Upon substitution of Eq. (2.13) and Eq. (2.21) into Eq. (2.62), for a given in-plane polarization vector $\mathbf{e} = (e_x, e_y) = (\cos(\varphi_\mathbf{e}), \sin(\varphi_\mathbf{e}))$, the matrix element $\left|\mathbf{e}\cdot\langle\psi^C|\hat{\mathbf{v}}|\psi^V\rangle\right|^2$, which enters Eq. (2.57) is given by:

$$\frac{4}{9}\frac{v_\mathrm{F}^2}{f_q^2}\left|\cos(\varphi_\mathbf{e})\cos\left[\frac{\pi}{3}\pm qa\sin(\varphi_\mathbf{q})\right] - \cos\left(\frac{\pi}{3}+\varphi_\mathbf{e}\right)\cos\left[\frac{\pi}{3}\mp qa\sin\left(\varphi_\mathbf{q}+\frac{\pi}{3}\right)\right]\right.$$

$$\left. - \cos\left(\frac{\pi}{3}-\varphi_\mathbf{e}\right)\cos\left[\frac{\pi}{3}\mp aq\sin\left(\varphi_\mathbf{q}-\frac{\pi}{3}\right)\right]\right|^2, \tag{2.63}$$

where $\varphi_\mathbf{q}$ and $\varphi_\mathbf{e}$ are the polarization and momentum angles as measured from the x-axis respec-

tively, the top / bottom sign corresponds to the $\mathbf{K}_+$ / $\mathbf{K}_-$ valley and

$$\begin{aligned} |f_q|^2 &= 3 - 2\cos\left(\frac{\pi}{3} \mp qa\sin\left(\varphi_{\mathbf{q}} - \frac{\pi}{3}\right)\right) - 2\cos\left(\frac{\pi}{3} \mp qa\sin\left(\varphi_{\mathbf{q}} + \frac{\pi}{3}\right)\right) \\ &- 2\cos\left(\frac{\pi}{3} \pm q\sin\left(\varphi_{\mathbf{q}}\right)\right). \end{aligned} \tag{2.64}$$

Note that the full derivation of Eq. (2.63) and Eq. (2.64) is given in Appendix A.2 and Appendix A.1 respectively. Eq. (2.57) thus becomes,

$$\begin{aligned} W_k = \frac{16\pi^2\hbar e^2 I_{\mathbf{e}} v_{\mathrm{F}}^2}{9ch^2\nu^2}\frac{1}{f_q^2}\Big|\cos\left(\varphi_{\mathbf{e}}\right)\cos\left[\frac{\pi}{3} \pm qa\sin\left(\varphi_{\mathbf{q}}\right)\right] - \cos\left(\frac{\pi}{3} + \varphi_{\mathbf{e}}\right)\cos\left[\frac{\pi}{3} \mp qa\sin\left(\varphi_{\mathbf{q}} + \frac{\pi}{3}\right)\right] \\ - \cos\left(\frac{\pi}{3} - \varphi_{\mathbf{e}}\right)\cos\left[\frac{\pi}{3} \mp aq\sin\left(\varphi_{\mathbf{q}} - \frac{\pi}{3}\right)\right]\Big|^2 \delta\left(2\xi_C - h\nu\right). \end{aligned} \tag{2.65}$$

2.3.3.1 The low energy regime (conical approximation)

In the low-energy regime, the effective matrix Hamiltonians Eq. (2.29) and their corresponding wavefunctions, Eq. (2.30), are sufficient to obtain the selection rules which govern interband transitions within this limit. Using the commutator form of the velocity operator the velocity matrix element can be written as:

$$\frac{i}{\hbar}\left(C^C\right)^\dagger\left(\hat{H}_{\pm}\mathbf{r}\right)C^V. \tag{2.66}$$

Evaluating $\hat{H}_{\pm}\mathbf{r}$ yields

$$\hat{H}_{\pm}\mathbf{r} = \hbar v_{\mathrm{F}}\begin{bmatrix} 0 & -\mathbf{i} \mp i\mathbf{j} \\ \mathbf{i} \mp i\mathbf{j} & 0 \end{bmatrix}, \tag{2.67}$$

where $\mathbf{i}$ and $\mathbf{j}$ are the Cartesian unit vectors. Upon substitution of Eq. (2.30) and Eq. (2.67) into Eq. (2.66) we obtain

$$\left\langle \psi^C \left|\hat{\mathbf{v}}\right| \psi^V \right\rangle = \mp i v_{\mathrm{F}}\left(\mathbf{i}\frac{q_y}{|\mathbf{q}|} - \mathbf{j}\frac{q_x}{|\mathbf{q}|}\right). \tag{2.68}$$

For a given in-plane polarization vector $\mathbf{e} = (e_x, e_y) = (\cos(\varphi_{\mathbf{e}}), \sin(\varphi_{\mathbf{e}}))$, the matrix element $\left|\mathbf{e}\cdot\left\langle \psi^C \left|\hat{\mathbf{v}}\right| \psi^V \right\rangle\right|^2$, which enters Eq. (2.57), is given by:

$$v_{\mathrm{F}}^2\frac{1}{q^2}\left|\left(e_y q_x - e_x q_y\right)\right|^2 = v_{\mathrm{F}}^2\sin^2\left(\varphi_{\mathbf{e}} - \varphi_{\mathbf{q}}\right). \tag{2.69}$$

It should be noted that Eq. (2.69), contains only one single phenomenological parameter v_{F}. Similar analysis can be performed for a circularly polarized excitation which results in an angularly-independent carrier distribution. Eq. (2.57) in the low energy regime thus becomes

$$W_k = \frac{2\pi e^2 I_{\mathbf{e}} v_{\mathrm{F}}^2}{ch\nu^2} \sin^2\left(\varphi_{\mathbf{e}} - \varphi_{\mathbf{q}}\right) \delta\left(2\xi_C - h\nu\right). \tag{2.70}$$

2.3.4 Distribution of photoexcited carriers

The angular generation density, $g\left(\varphi_{\mathbf{q}}\right)$, for a given valley, is defined such that $g\left(\varphi_{\mathbf{q}}\right) d\varphi_{\mathbf{q}}$ gives the number of carriers created in the angle range $\varphi_{\mathbf{q}}$ to $\varphi_{\mathbf{q}} + d\varphi_{\mathbf{q}}$. For a single valley and spin the angular generation density is given by

$$g\left(\varphi_{\mathbf{q}}\right) = \left(\frac{1}{2\pi}\right)^2 \int_0^\infty W_k\left(q, \varphi_q\right) q dq \tag{2.71}$$

which in the low-energy regime becomes:

$$g\left(\varphi_{\mathbf{q}}\right) = \frac{\hbar e^2 I_e v_{\mathrm{F}}^2}{ch^2\nu^2} \int_0^\infty \sin^2\left(\varphi_{\mathbf{e}} - \varphi_{\mathbf{q}}\right) \delta\left(2\xi_C - h\nu\right) q dq. \tag{2.72}$$

Changing this to an integral over equi-energy surfaces by the substitution $\xi_C = v_{\mathrm{F}}\hbar\left|\mathbf{q}\right|$ and subsequent integration yields:

$$g\left(\varphi_{\mathbf{q}}\right) = \frac{e^2}{4\hbar c}\frac{I_e}{h\nu} \sin^2\left(\varphi_{\mathbf{e}} - \varphi_{\mathbf{q}}\right) \equiv \frac{e^2}{8\hbar c}\frac{I_e}{h\nu}\left[1 - \cos\left(2\varphi_{\mathbf{e}} - 2\varphi_{\mathbf{q}}\right)\right] \tag{2.73}$$

It should be noted that the angular generation density is the same for both valleys. By integrating this expression over all directions of electron momentum and summing over valley and spin indices, one can easily recover the results obtained within the optical conductivity formalism [40, 41, 42, 43] including the universal value of single layer absorption [6].

In the low energy regime, the distribution function of the photoexcited carriers, generated by a linearly polarized excitation, at the instant of photogeneration (i.e. before relaxation) is defined by

$$\mathcal{F}_0\left(\mathbf{q}\right) = F_0\left(\nu\right)\left[1 - \cos\left(2\theta\right)\right], \tag{2.74}$$

where θ is the angle between $\hat{\mathbf{e}}$ and wave vector $\mathbf{q}$. Thus, the illumination of graphene with linearly polarized radiation results in an anisotropic momentum distribution of photoexcited carriers, with the preferential direction of propagation normal to the excitation's polarization plane. Hence, one can effectively steer the direction of electrons by light. In Fig. 2.3 a polar plot of $\mathcal{F}_0$ is shown for light of normal incidence and the polarization angle, $\varphi_{\mathbf{e}} = 0$.

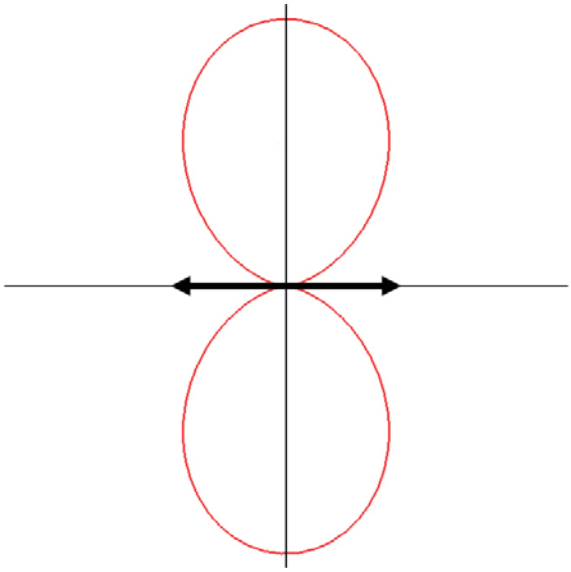

Figure 2.3: A polar plot of the momentum distribution of photo-excited carriers in the low-energy regime for $\varphi_{\mathbf{e}} = 0$. Here, the black arrow represents the polarization of the excitation.

In a more general form Eq. (2.74) may be written as,

$$\mathcal{F}_0(\mathbf{q}) = F_0(\nu)\left[1 + \alpha_0 \cos(2\theta)\right], \tag{2.75}$$

where α_0 defines the degree of alignment. Unlike conventional systems, in graphene $\alpha_0 = -1$ and is not a function of the excitation energy.

Let us now analyze the angular generation density in the range in which trigonal warping effects become important, in this regime Eq. (2.71) is given by

$$g(\varphi_{\mathbf{q}}) = \frac{4\hbar e^2 v_{\mathrm{F}}^2 I}{9ch^2\nu^2} \int \frac{1}{|f_q|^2} q dq \delta(2\xi_C - h\nu) \times$$

$$\left|\cos(\varphi_{\mathbf{e}}) \cos\left(\frac{\pi}{3} \pm qa\sin(\varphi_{\mathbf{q}})\right) - \cos\left(\varphi_{\mathbf{e}} + \frac{\pi}{3}\right) \cos\left[\frac{\pi}{3} \mp aq\sin\left(\varphi_{\mathbf{q}} + \frac{\pi}{3}\right)\right]\right.$$

$$\left. - \cos\left(\varphi_{\mathbf{e}} - \frac{\pi}{3}\right) \cos\left[\frac{\pi}{3} \mp aq\sin\left(\varphi_{\mathbf{q}} - \frac{\pi}{3}\right)\right]\right|^2, \tag{2.76}$$

The contributions to the momentum distribution function, Eq. (2.76), from the $\mathbf{K}_+$ and $\mathbf{K}_-$ valleys are inequivalent. Alone the individual valley contributions do not preserve the required symmetry of the distribution function. Only when both valley contributions are taken into account the symmetry of $g(\varphi_{\mathbf{q}}) = g(\varphi_{\mathbf{q}} + \pi)$ is restored, as can be seen from Fig. 2.4. One should note that

to obtain the plots presented in Fig. 2.4 the delta function has been approximated by

$$\delta\left(2\xi_C - h\nu\right) = \frac{1}{\pi}\lim_{\ell\to 0}\frac{\ell}{\left(2\xi_C - h\nu\right)^2 + \ell^2}. \tag{2.77}$$

Therefore, two **K** points are required to describe the optical properties of the system and as soon as trigonal warping becomes important the one-valley picture provides an insufficient description. The majority of publications on graphene are restricted to a single-valley picture, although inter-valley scattering and valley mixing are essential for explaining weak localization data [44, 45] and are used in the study of graphene nano-ribbons [46]. This effect serves as an example of a completely "bulk" phenomena, in a clean graphene system, in which disregarding one of the two valleys gives an unphysical result.

The difference between the $\mathbf{K}_+$ and $\mathbf{K}_-$ valley's angular generation density can be understood in a simple manner. The conservation of energy during an optical transition maps out an equi-energy-contour in k-space which represents all the allowed values of q which can take part in the transition. In the low energy regime this contour has a constant radius of $q = h\upsilon/\hbar$, however in the high energy regime the magnitude of the allowed q-vectors is angle dependent, q being maxima at those angles directed towards the apexes of the triangles and minima in those directions directed towards the triangles bases (see Fig. 2.5). Since the probability of absorption is dependent on the size of the integral element, qdq, the probability of absorption is maximized along those angles directed towards the apexes of the triangles. This is manifested in the momentum distribution by an elongation of the lobes along such directions. The difference between the two valleys occurs because the two valley's equi-energy-contours are orientated differently with respect to one another, therefore each valley will have different preferential angles of absorption, as can be seen from Fig. 2.5.

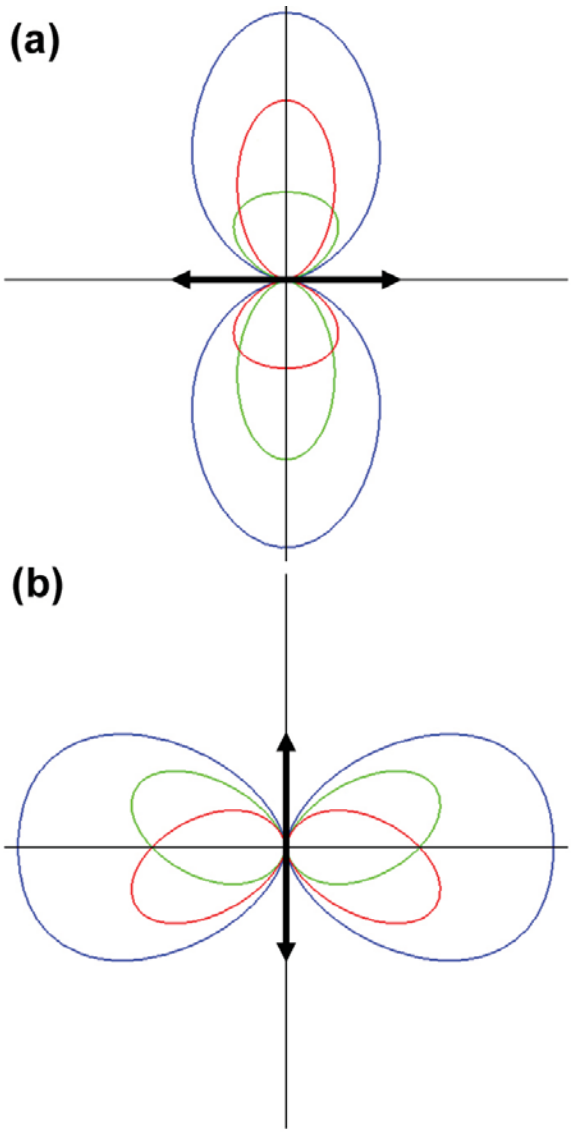

Figure 2.4: A polar plot of the momentum distribution of photo-excited carriers for $h\nu = 0.6\,|t|$ and (a) $\varphi_{\mathbf{e}} = 0$; (b) $\varphi_{\mathbf{e}} = \pi/2$. Here, the red and green lines represent the contributions from the $\mathbf{K}_+$ and $\mathbf{K}_-$ points respectively, and the black arrows represent the polarization of the excitations.

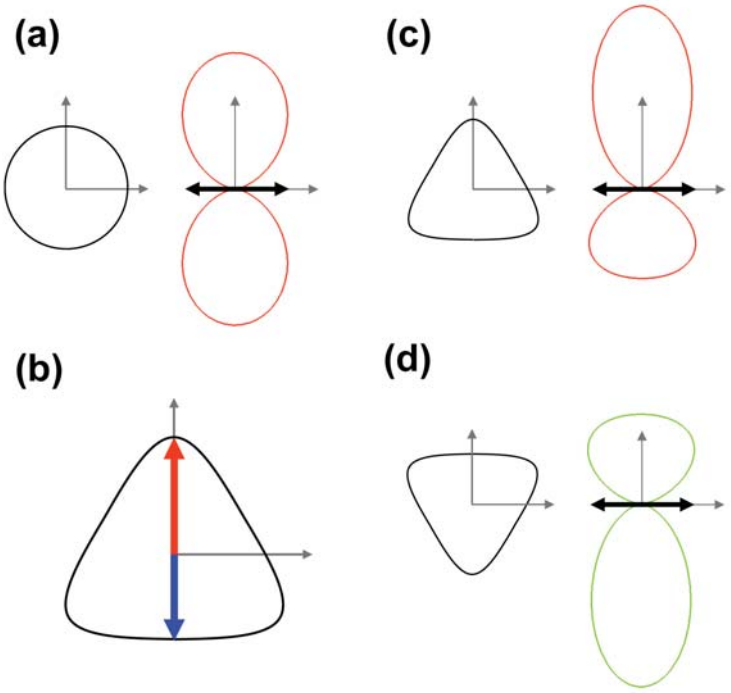

Figure 2.5: (a) A polar plot of the momentum distribution of photo-excited carriers in the low-energy regime for $\varphi_{\mathbf{e}} = 0$. (b) The equi-energy-contour around the $\mathbf{K}_+$ point (black line), in the regime where trigonal warping becomes important. Here, the red line indicates a direction in k-space where q is a maxima, while the blue line indicates a direction in k-space where q is a minima. The contribution to the momentum distribution of photo-excited carriers from the (c) $\mathbf{K}_+$ point and (d) $\mathbf{K}_-$ is shown. In both instances $\varphi_{\mathbf{e}} = 0$ and $h\nu = 0.6\,|t|$. As a guide to the eye, the corresponding equi-energy contours are drawn next to each distribution function and the black arrows represent the polarization of the excitations.

2.4 The depolarization of photoluminescence in phonon replicas

As was mentioned in the introduction, the main manifestation of the alignment phenomena in conventional semiconductors was the polarization of the hot photoluminescence, which was a major tool in the study of relaxation processes. In the following section we shall see how the same alignment phenomena which was so useful in conventional semiconductors can be applied to graphene.

The intensity of photoluminescence is given by the expression

$$I\left(\varphi_{\mathbf{e}},\varphi_{\mathbf{e}'}\right)\propto\int\left|M\left(\varphi_{\mathbf{q}},\varphi_{\mathbf{e}'}\right)\right|^{2}f_{e}\left(\varphi_{\mathbf{q}},\varphi_{\mathbf{e}}\right)f_{h}\left(\varphi_{\mathbf{q}},\varphi_{\mathbf{e}}\right)d\varphi_{\mathbf{q}}, \tag{2.78}$$

where $\varphi_{\mathbf{e}'}$ is the detector polarization angle, f_e and f_h are the momentum distribution functions of the electrons and holes respectively and $\left|M\left(\varphi_{\mathbf{q}},\varphi_{\mathbf{e}'}\right)\right|^{2}$ is the matrix element of optical transition which was studied in the previous section.

The degree of the linear polarization, P, of the luminescence can be described by the following expression:

$$P=\frac{I_{\parallel}-I_{\perp}}{I_{\parallel}+I_{\perp}}=\frac{I\left(\varphi_{\mathbf{e}},\varphi_{\mathbf{e}}\right)-I\left(\varphi_{\mathbf{e}},\varphi_{\mathbf{e}}+\frac{\pi}{2}\right)}{I\left(\varphi_{\mathbf{e}},\varphi_{\mathbf{e}}\right)+I\left(\varphi_{\mathbf{e}},\varphi_{\mathbf{e}}+\frac{\pi}{2}\right)}, \tag{2.79}$$

where $I_{\parallel}$ and $I_{\perp}$ are the HPL intensities of the luminescence peak, for the detector polarization, $\hat{\mathbf{e}}'$, parallel and perpendicular to the incident polarization, $\hat{\mathbf{e}}$.

In conventional semiconductors, photoexcited carriers recombine with the acceptor level to produce a luminescence peak occurring at a different energy to that of the excitation energy. However, graphene's linear band structure means that direct recombination will result in a luminescence peak occurring at the same frequency as the excitation, making such a luminescence peak indistinguishable from specular reflection. Therefore, to observe any luminescence electrons must relax in energy before recombining with holes to luminescence.

The main relaxation mechanism in graphene is phonon scattering. When hot electrons scatter with phonons their energies will reduce in discretized steps. After each phonon interaction, the relaxed electron may either combine with a hole, to luminescence, or suffer subsequent interactions. There will therefore be several peaks (known as phonon-replicas) in the HPL spectrum, each corresponding to an electron whose energy is $n\times E_{ph}$ below $h\nu/2$, where E_{ph} is the energy of the phonon and n is the number of phonon interactions suffered.

It was shown in the previous section that photoexcited carriers generated by a linearly polarized excitation are distributed anisotropically in momentum space. We shall assume that the momentum

distribution function of the n^{th} phonon replica, $\mathcal{F}_n(\mathbf{q}')$, can be written in the same form as Eq. (2.74):

$$\mathcal{F}_n(\mathbf{q}') \propto \left[1 + \alpha_n \cos\left(2\varphi_{\mathbf{e}'} - 2\varphi_{\mathbf{q}'}\right)\right]. \tag{2.80}$$

This assumption will be justified later. The degree of linear polarization of the HPL corresponding to the n^{th} phonon replica is

$$P_n = \frac{I_{n,\parallel} - I_{n,\perp}}{I_{n,\parallel} + I_{n,\perp}} = \frac{I_n(\varphi_{\mathbf{e}}, \varphi_{\mathbf{e}}) - I_n\left(\varphi_{\mathbf{e}}, \varphi_{\mathbf{e}} + \frac{\pi}{2}\right)}{I_n(\varphi_{\mathbf{e}}, \varphi_{\mathbf{e}}) + I_n\left(\varphi_{\mathbf{e}}, \varphi_{\mathbf{e}} + \frac{\pi}{2}\right)}, \tag{2.81}$$

where $I_{n,\parallel}$ and $I_{n,\perp}$ are the intensities of photoluminescence of the n_{th} phonon replicas, for the detector polarization, $\hat{\mathbf{e}}'$, parallel and perpendicular to the incident polarization, $\hat{\mathbf{e}}$.

Each phonon interaction causes the momentum distribution function of photoexcited carriers to deviate further from the initial anisotropic distribution, this degradation will result in a reduction in the degree of linear polarization with every phonon interaction suffered. This degradation is quantified by the degree of linear depolarization, ρ, and is defined as the ratio of the degree of linear polarization of the $(n+1)^{th}$ HPL peak to that of the n^{th} peak:

$$\rho = \frac{P_{n+1}}{P_n}. \tag{2.82}$$

It shall be shown that by comparing the depolarization from successive phonon replicas, the mechanisms for phonon relaxation can be studied. Furthermore, by studying the depolarization of HPL in a magnetic field (the Hanle effect) one can obtain the phonon emission times of hot electrons. We shall consider the depolarization of photoluminescence in two distinct cases: Firstly, we consider the case where the Fermi-level (ϵ_F) lies below the charge neutrality point (p-doped) with the requirement that $nE_{ph} > |\epsilon_F|$. Secondly, we shall analyze the case of undoped graphene, where the Fermi-level lies at the charge neutrality point. Both cases are illustrated in Fig. 2.6.

For the case of p-doped graphene where $nE_{ph} > |\epsilon_F|$, photoexcited electrons can recombine with equilibrium holes, in this instance f_h is isotropic and the intensity of HPL is given by,

$$I_n(\varphi_{\mathbf{e}}, \varphi_{\mathbf{e}'}) \propto \int_{-\pi}^{\pi} \left[1 - \cos\left(2\varphi_{\mathbf{e}'} - 2\varphi_{\mathbf{q}'}\right)\right] \left[1 + \alpha_n \cos\left(2\varphi_{\mathbf{e}} - 2\varphi_{\mathbf{q}'}\right)\right] d\varphi_{\mathbf{q}'}. \tag{2.83}$$

From Eq. (2.79) and Eq. (2.83) the degree of linear polarization is found to be:

$$P_n = -\frac{\alpha_n}{2} \tag{2.84}$$

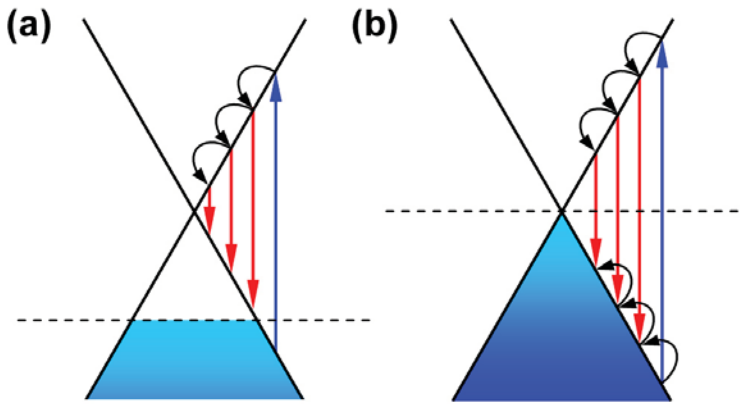

Figure 2.6: The relaxation of hot electrons via the interaction with optical phonons. After each phonon interaction, the relaxed electron may either luminescence due to the recombination with: (a) an equilibrium hole, in the case of the Fermi-level (dashed line) lying below the charge neutrality point; or (b) a non-equilibrium hole, in the case of undoped graphene. Alternatively, the hot electron may suffer subsequent interactions. The blue line represents the electron transition caused by the linearly polarized excitation and the red line represents electron-hole recombination. The black line represents an intraband transition caused by an electron-phonon interaction.

and the degree of linear depolarization in this instance is

$$\rho_n = \frac{\alpha_{n+1}}{\alpha_n}. \tag{2.85}$$

Lets now consider the case where the Fermi-level lies at the charge neutrality point. Electron-hole symmetry requires $f_e = f_h = \mathcal{F}_n$ thus the intensity of hot electron luminescence is given by

$$I_n\left(\varphi_{\mathbf{e}}, \varphi_{\mathbf{e}'}\right) \propto \int_{-\pi}^{\pi} \left[1 - \cos\left(2\varphi_{\mathbf{e}'} - 2\varphi_{\mathbf{q}'}\right)\right] \left[1 + \alpha_n \cos\left(2\varphi_{\mathbf{e}} - 2\varphi_{\mathbf{q}'}\right)\right]^2 d\varphi_{\mathbf{q}'}. \tag{2.86}$$

From Eq. (2.79) and Eq. (2.86) the degree of linear polarization for the case of the Fermi-level lying at the charge neutrality point is

$$P_n = -\frac{2\alpha_n}{2 + \alpha_n^2} \tag{2.87}$$

and the degree of linear depolarization is given by

$$\rho_n = \frac{\alpha_{n+1}}{\alpha_n}\left[\frac{2 + \alpha_n^2}{2 + \alpha_{n+1}^2}\right]. \tag{2.88}$$

Defining $w\left(\mathbf{q}, \mathbf{q}'\right)$ as the probability of a transition (per unit time) of an electron from a state with wave vector $\mathbf{q}$ at energy E_0 to state $\mathbf{q}'$ at energy $E_1 = E_0 - E_{ph}$, we can then write the distribution function after one transition as follows:

$$\mathcal{F}_1(\mathbf{q}') \propto \sum_{\mathbf{q}} w(\mathbf{q},\mathbf{q}')\,\mathcal{F}_0(\mathbf{q})\left[1-\mathcal{F}_1(\mathbf{q}')\right]. \tag{2.89}$$

In the weak pumping regime, where $\mathcal{F}_1(\mathbf{q}') \ll 1$ Eq. (2.89), becomes

$$\mathcal{F}_1(\mathbf{q}') \propto \int_{-\pi}^{\pi} w(\mathbf{q},\mathbf{q}')\left[1+\alpha_0\cos\left(2\varphi_{\mathbf{e}}-2\varphi_{\mathbf{q}}\right)\right]d\varphi_{\mathbf{q}} \tag{2.90}$$

Defining ϕ_1 as the angle between $\hat{\mathbf{e}}$ and $\mathbf{q}'$ and θ as the angle between $\mathbf{q}$ and $\mathbf{q}'$ Eq. (2.90) can be expressed as

$$\mathcal{F}_1(\mathbf{q}') \propto \int_{-\pi}^{\pi} w(\mathbf{q},\mathbf{q}')\left[1+\alpha_0\cos\left(2\phi_1-2\theta\right)\right]d\theta. \tag{2.91}$$

If $w(\mathbf{q},\mathbf{q}')$ is an even function of the angle θ (which is true with the emission of an optical phonon by an electron) one obtains

$$\mathcal{F}_1(\mathbf{q}') \propto \int_{-\pi}^{\pi} w(\mathbf{q},\mathbf{q}')\left[1+\alpha_0\cos\left(2\phi_1\right)\cos\left(2\theta\right)\right]d\theta. \tag{2.92}$$

Since $\mathcal{F}_1(\mathbf{q}')$ can be written in the same form as Eq. (2.75):

$$\mathcal{F}_1(\mathbf{q}') \propto \left[1+\alpha_1\cos\left(2\phi_1\right)\right]. \tag{2.93}$$

Eqs. (2.75, 2.92, 2.93) yield;

$$\frac{\alpha_1}{\alpha_0} = \frac{\int_{-\pi}^{\pi} w(\mathbf{q},\mathbf{q}')\cos\left(2\theta\right)d\theta}{\int_{-\pi}^{\pi} w(\mathbf{q},\mathbf{q}')\,d\theta}. \tag{2.94}$$

Similarly the ratio of the $(n+1)^{th}$ and n^{th} anisotropy parameters is found to be

$$\frac{\alpha_{n+1}}{\alpha_n} = \frac{\alpha_1}{\alpha_0}. \tag{2.95}$$

2.4.1 Phonon induced transitions in graphene

Graphene was first isolated by mechanically exfoliating graphene sheets from bulk graphite [1]. This method of production produces limited sample sizes (up to a millimeter in size) and has a low production yield and is thus unsuitable for technological applications. Graphene can however be grown epitaxially on silicon carbide (SiC), by vacuum graphitization [47] due to the Si depletion of the SiC surface. The surface of SiC used for graphitization (silicon-terminated or carbon-terminated) strongly dictates the thickness, mobility and carrier density of the graphene. For example, the Fermi level of graphene grown on Si-terminated SiC lies approximately $0.3-0.45\,eV$

above the Dirac point [48, 49]. This method of growth allows the production of centimeter size graphene mono- or bilayer samples [50, 51, 52, 53]. Moreover, graphene on SiC retains its linear spectrum, allowing the observation of the anomalous quantum Hall effect [54, 55, 56, 57] and weak anti-localization [58]. The production of large scale graphene flakes gives rise to the possibility of large area integrated electronics [59, 60, 61].

In what follows we shall consider the relaxation of photoexcited carriers in epitaxial graphene on SiC, restricting ourselves to intravalley transitions due to optical phonons. Indeed, intervalley transitions are important and they shall be a subject of future study. However, these transitions correspond to luminescence peaks occurring at noticeably different frequencies to that of intravalley transitions.

There are three optical phonon modes in graphene: longitudinal (LO), transverse (TO) and flexural (ZO, which we shall assume are suppressed due to the underlying substrate). We shall first consider the relaxation of photoexcited carriers due to phonons which are intrinsic to graphene. We shall then consider the coupling of photoexcited carriers in graphene to bulk optical phonons in silicon carbide, this coupling occurs via the Fröhlich interaction. The two cases will result in drastically different depolarizations. Namely, in the weak pumping regime, the momentum distribution function corresponding to an energy of one graphene long-wavelength optical phonon energy below $h\nu/2$ is completely isotropic; whereas the momentum distribution function corresponding to an energy due to an interaction with SiC bulk optical phonons below $h\nu/2$ results in an anisotropic momentum distribution function.

2.4.2 Relaxation of hot electrons in free standing graphene

For the **K** point the electron wavefunction in graphene is given by [62]:

$$\frac{1}{\sqrt{2}}\begin{bmatrix} s \\ e^{i\varphi_{\mathbf{q}}} \end{bmatrix} e^{i\mathbf{q}\cdot\mathbf{r}}, \tag{2.96}$$

where $s = +1$ and -1 denote the conduction and valence bands, respectively. For long-wavelength optical phonons, the electron-phonon interaction Hamiltonian for the **K** point is given by [62]:

$$\mathcal{H}_{\text{int}} = -\sqrt{\frac{\hbar}{2NM\omega_0}} \sum_{\mathbf{p},\mu} \sqrt{2}\frac{\beta t'}{b^2} V_\mu(\mathbf{p})\, e^{i\mathbf{p}\cdot\mathbf{r}} \left(b_{\mathbf{p}\mu} + b^\dagger_{-\mathbf{p}\mu}\right) \tag{2.97}$$

where

$$V_l(\mathbf{p}) = \begin{bmatrix} 0 & -e^{-i\varphi_{\mathbf{p}}} \\ e^{i\varphi_{\mathbf{p}}} & 0 \end{bmatrix}, \tag{2.98}$$

and

$$V_t(\mathbf{p}) = \begin{bmatrix} 0 & ie^{-i\varphi_{\mathbf{p}}} \\ ie^{i\varphi_{\mathbf{p}}} & 0 \end{bmatrix}. \tag{2.99}$$

ω_0 is the phonon frequency at the Γ point, $\mathbf{p}$ is the phonon wave-vector, $\mu = l$ and t denote the transverse and longitudinal modes respectively, and $b^{\dagger}_{\mathbf{p}\mu}$ and $b_{\mathbf{p}\mu}$ are the creation and annihilation operators. N is the number of unit cells, M is the mass of a carbon atom, $b = a/\sqrt{3}$ is the equilibrium bond length, β is given by

$$-\frac{d\ln t}{d\ln b} \tag{2.100}$$

and $t' = \frac{\sqrt{3}}{2}t$.

The probability of a phonon-induced transition, $w_\mu(\mathbf{q}, \mathbf{q}')$, from a state $|s\mathbf{q}\rangle$ at energy E_0 to a state $|s'\mathbf{q}'\rangle$ at energy $E_1 = E_0 - \hbar\omega_0$, caused by the phonon of type μ, is proportional to $\left|\langle s'\mathbf{q}' \left|V^{\mathbf{K}}_{\mu}\right| s\mathbf{q}\rangle\right|^2$. Eqs. (2.96, 2.97, 2.98, 2.99) yield;

$$w_\mu(\mathbf{q}, \mathbf{q}') \propto \left[1 - ss's_\mu \cos\left(\varphi_{\mathbf{q}} + \varphi_{\mathbf{q}'} - 2\varphi_{\mathbf{p}}\right)\right] \delta_{\mathbf{q},\mathbf{q}'+\mathbf{p}}, \tag{2.101}$$

with $s_\mu = +1$ for the longitudinal mode and -1 for the transverse mode and $\delta_{\mathbf{q},\mathbf{q}'+\mathbf{p}}$ reflects momentum conservation. c.f. Ref. [62] where the matrix element is obtained for "direct" phonon-induced transitions.

It follows from Eq. (2.101) that the probability of a intraband transition (per unit time) of an electron from a state with wave vector $\mathbf{q}$ at energy E_0 to state $\mathbf{q}'$ at energy $E_1 = E_0 - E_{ph}$ is:

$$w(\mathbf{q}, \mathbf{q}') \propto \sum_{\mu} A_\mu \left[1 - s_\mu \cos\left(\varphi_{\mathbf{q}} + \varphi_{\mathbf{q}'} - 2\varphi_{\mathbf{p}}\right)\right] \delta_{\mathbf{q},\mathbf{q}'+\mathbf{p}}, \tag{2.102}$$

where A_μ is a weighting coefficient. In the low temperature regime, $A_\mu = 1$ and the total transition rate due to phonons at the Γ point is given by, $w(\mathbf{q}, \mathbf{q}') = Constant$. In this instance Eq. (2.94) $= 0$ and hence after one transition the momentum distribution function becomes completely isotropic. However, away from the Γ point the optical phonon branches differ in energy [63, 64] and in what follows we shall see that longitudinal and transverse phonons result in different degrees of polarization of the HPL. Indeed, since each optical phonon branch differs in energy, one should expect each HPL peak to split into two separate peaks, which should be resolvable in detector polarization .

In what follows, we shall analyze the individual effects of transverse and longitudinal optical phonons, calculating the degree of polarization of the HPL due to each phonon type in isolation.

The transition rate due to transverse optical phonons is

$$w_t\left(\mathbf{q},\mathbf{q}'\right) \propto \left(1-r\right)\frac{1+\cos\left(\theta\right)}{1-r\cos\left(\theta\right)}, \tag{2.103}$$

where $r = 2qq'/(q^2+q'^2)$. It should be noted that in the limit that $q' \to q$, there is a complete suppression in the emission of transverse optical phonons. From Eq. (2.94) and Eq. (2.103) the ratio of the anisotropy parameters of successive phonon replicas is found to be

$$\frac{\alpha_1}{\alpha_0} = \frac{1}{2}\left(\frac{q'}{q}\right)\frac{1-\left(\frac{q'}{q}\right)^2}{1-\left(\frac{q'}{q}\right)}. \tag{2.104}$$

Therefore, transverse optical phonons result in a momentum distribution function which is maximum when the momentum of the electron is aligned perpendicularly to the polarization of the excitation.

We shall now consider solely the effect of longitudinal optical phonons, in this instance the transition rate is given by:

$$w_l\left(\mathbf{q},\mathbf{q}'\right) \propto \left(1+r\right)\frac{1-\cos\left(\theta\right)}{1-r\cos\left(\theta\right)} \tag{2.105}$$

and from Eq. (2.94) and Eq. (2.105) the ratio of the anisotropy parameters of successive phonon replicas is found to be

$$\frac{\alpha_1}{\alpha_0} = -\frac{1}{2}\left(\frac{q'}{q}\right)\frac{1-\left(\frac{q'}{q}\right)^2}{1+\left(\frac{q'}{q}\right)}. \tag{2.106}$$

Hence, longitudinal optical phonons result in a momentum distribution function which is maximum when the momentum of the electron is aligned with the polarization of the excitation. Note that the full derivation of w_t, w_l and their corresponding ratios of the anisotropy parameters is given in Appendix A.3.

2.4.3 Phonon induced transitions on epitaxial graphene on silicon carbide

Let us now consider the coupling of electrons in graphene to bulk optical phonons in silicon carbide. The coupling to optical phonons occurs through the Fröhlich interaction. In this instance, the probability of a transition from a state with wave vector $\mathbf{q}$ to a state with wave vector $\mathbf{q}'$, when an electron interacts with a bulk LO phonon, is described by the expression

$$w\left(\mathbf{q},\mathbf{q}'\right) \propto \frac{2\pi}{p_z^2+p_{||}^2} \tag{2.107}$$

where p_z and $p_{\shortparallel}$ are the components of the phonon wave vector normal to, and in the plane of, the graphene sheet respectively. $\mathbf{q}$ and $\mathbf{q}'$ are related by the energy conservation law

$$E_0 = E_1 + \hbar\omega_0 \tag{2.108}$$

and conservation of in-plane momentum requires $\mathbf{p}_{\shortparallel} = \mathbf{q} - \mathbf{q}'$ hence,

$$p_{\shortparallel} = \sqrt{q^2 + q'^2 - 2qq'\cos(\theta)}. \tag{2.109}$$

The ratio of the anisotropy parameters is found to be:

$$\frac{\alpha_1}{\alpha_0} = \int_0^{\frac{\pi}{2}} \frac{\cos(4\Theta)}{\sqrt{1 - R^2\sin^2(\Theta)}} d\Theta \Big/ \int_0^{\frac{\pi}{2}} \frac{1}{\sqrt{1 - R^2\sin^2(\Theta)}} d\Theta, \tag{2.110}$$

where $R^2 = \frac{4qq'}{(q+q')^2}$ and $\Theta = \left(\frac{\pi}{2} - \frac{\theta}{2}\right)$. Both integrals in Eq. (2.110) can be expressed in terms of elliptic integrals of the first ($\boldsymbol{K}$) and second kind ($\boldsymbol{E}$):

$$\frac{\alpha_1}{\alpha_0} = \frac{1}{3q^2q'^2}\left[\left(q^2 + q'^2\right)^2 - q^2q'^2 - \left(q^2 + q'^2\right)(q + q')^2 \frac{\boldsymbol{E}(R)}{\boldsymbol{K}(R)}\right]. \tag{2.111}$$

The full derivation is given in Appendix A.4. It can be seen from the above expression that electrons which relax via the interaction with optical phonons in SiC maintain their anisotropic momentum distribution function. In Fig. 2.7, we plot the ratio of the anisotropy parameters given in Eq. (2.111) as a function of x, where

$$x = \frac{q'}{q} = 1 - \frac{\hbar\omega_0}{E_0} = 1 - 2\frac{\hbar\omega_0}{h\nu}. \tag{2.112}$$

For a red light laser, $h\nu \approx 1.8\,\text{eV}$, and taking $\hbar\omega_0 \approx 190\,\text{meV}$ [64] the ratio of the anisotropy parameters is found to be

$$\frac{\alpha_1}{\alpha_0} \approx 0.26 \tag{2.113}$$

The resulting momentum distribution of photoexcited carriers after the interaction with one bulk optical phonon in silicon carbide is shown in Fig. 2.8. This result is a stark contrast to the case of photoexcited carriers which have relaxed via long-wavelength optical phonons intrinsic to graphene, which resulted in the complete depolarization of the HPL. Therefore, by looking at the degree of polarization of the HPL, one should be able to determine the dominant relaxation mechanism for graphene on SiC.

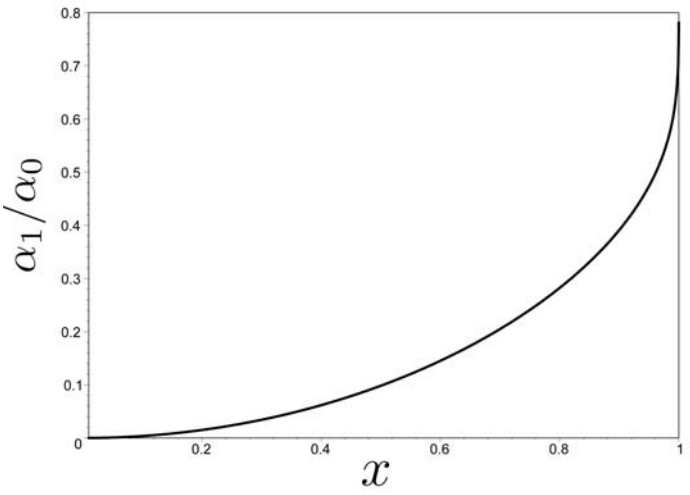

Figure 2.7: The dependence of α_1/α_0 on x (where $x = q'/q$) due to the coupling of electrons in graphene to bulk optical phonons in silicon carbide.

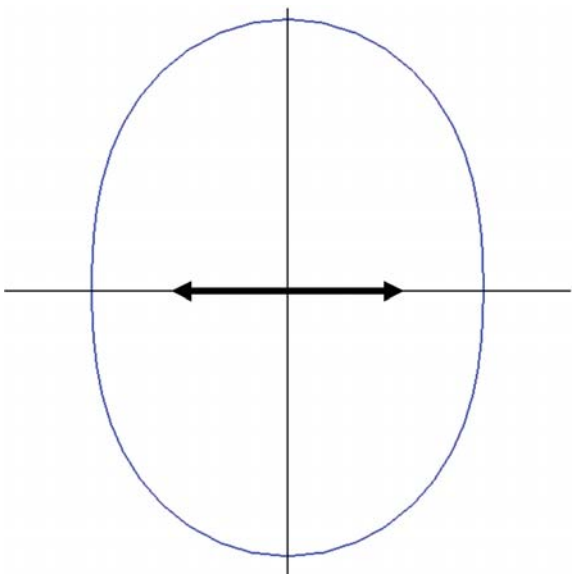

Figure 2.8: A polar plot of the momentum distribution function of photoexcited carriers, generated by a linear excitation of energy $h\nu = 1.8$ eV and polarization, $\varphi_{\mathbf{e}} = 0$, after the interaction with one bulk optical phonon in silicon carbide ($E_{ph} \approx 190$ meV). Here, the black arrow represents the polarization of the excitation.

2.4.4 Depolarization of photoluminescence in a magnetic field

We shall now consider the influence of a magnetic field on the linear polarization of the luminescence. It shall be assumed that the magnetic field, B, is applied normal to the graphene sheet (Faraday geometry). The influence of the field is due to the the Lorentz force, which rotates the momentum of the hot electrons thereby causing the momentum distribution to rotate. t is the time as measured from the moment of photocreation. In this time the distribution would have rotated by an angle $\omega_C t$, where ω_C is the cyclotron frequency which in graphene is given by $\omega_C = v_{\mathrm{F}}^2 eB/(c\xi)$, where e and ξ are the charge and energy of the particle respectively. Notably, in this classical regime the cyclotron frequency is energy dependent and the energy of the particle plays the role of the cyclotron mass. The probability that in the time t the electron does not lose its energy is $\exp\left(-\frac{t}{\tau}\right)$, where τ is the lifetime of the electron. We shall now consider low pumping, such that the electron-electron interaction can be neglected. In this regime one can assume that $\tau \approx \tau_0$, where τ_0 is the emission time for a phonon. The intensity of luminescence in a magnetic field when the Fermi-level lies at the charge neutrality point is given by [65]

$$I_n^M\left(\varphi_{\mathbf{e}}, \varphi_{\mathbf{e}'}\right) \propto \int_{-\pi}^{\pi} \int_{0}^{\infty} \left|M\left(\varphi_{\mathbf{q}}, \varphi_{\mathbf{e}'}\right)\right|^2 f_e\left(\varphi_{\mathbf{q}} - 2\omega_C t, \varphi_{\mathbf{e}}\right) f_h\left(\varphi_{\mathbf{q}}, \varphi_{\mathbf{e}}\right) \exp\left(-\frac{t}{\tau}\right) dt d\varphi_{\mathbf{q}} \tag{2.114}$$

and below the charge neutrality point subject to the requirement that $nE_{ph} > |\epsilon_F|$ is

$$I_n^M\left(\varphi_{\mathbf{e}}, \varphi_{\mathbf{e}'}\right) \propto \int_{-\pi}^{\pi} \int_{0}^{\infty} \left|M\left(\varphi_{\mathbf{q}}, \varphi_{\mathbf{e}'}\right)\right|^2 f_e\left(\varphi_{\mathbf{q}} - \omega_C t, \varphi_{\mathbf{e}}\right) \exp\left(-\frac{t}{\tau}\right) dt d\varphi_{\mathbf{q}}. \tag{2.115}$$

Note, the factor of $2\omega_C t$ appearing in Eq. (2.114) accounts for the counter-rotation of the electron and hole distribution functions. From Eq. (2.79) and Eq. (2.114) the degree of linear polarization in a magnetic field $\left(P_n^M\right)$ for the Fermi-level at the charge neutrality point is:

$$P_n^M = -2\alpha_n \left(\frac{1 + 8\tau^2\omega_C^2}{2 + \alpha_n^2 + 32\tau^2\omega_C^2}\right)\left(\frac{1}{1 + 4\tau^2\omega_C^2}\right) \tag{2.116}$$

and the dependence of the degree of linear polarization of the HPL on B, is given by:

$$\frac{P_n(B)}{P_n(0)} = \left(2 + \alpha_n^2\right)\left(\frac{1 + 8\tau^2\omega_C^2}{2 + \alpha_n^2 + 32\tau^2\omega_C^2}\right)\left(\frac{1}{1 + 4\tau^2\omega_C^2}\right). \tag{2.117}$$

For the case of p-doped graphene where $nE_{ph} > |\epsilon_F|$, from Eq. (2.79) and Eq. (2.115) the degree of linear polarization in a magnetic field is found to be

$$P_n^M = -\frac{\alpha_n}{2}\left(\frac{1}{1+4\tau^2\omega_C^2}\right) \tag{2.118}$$

and in this instance the dependence of the degree of linear polarization of the HPL on B, is

$$\frac{P_n(B)}{P_n(0)} = \left(\frac{1}{1+4\tau^2\omega_C^2}\right). \tag{2.119}$$

Notably this is the same result obtained in GaAs / AlGaAs quantum wells in the isotropic valance band, no warping approximation. This result was used with great success to study the kinetic and band structure properties of GaAs, InP and some alloys [27] and was used to obtain the emission of LO phonons in GaAs.

2.5 Optovalleytronics

Within the trigonal warping regime a linearly polarized excitation could be utilized as a means of breaking valley degeneracy and as a control mechanism in valleytronic devices. It can be seen from Fig. 2.4 that for a given polarization, the asymmetry between each valley's contribution to the momentum distribution is maximized for preferential directions. Along such directions there is a net difference between carriers generated from the $\mathbf{K}_+$ and $\mathbf{K}_-$ valleys. To quantify this effect we introduce the degree of valley polarization, $S_{\mathbf{K}_+\mathbf{K}_-}$, defined as

$$S_{\mathbf{K}_+\mathbf{K}_-} = \frac{F_{\mathbf{K}_+} - F_{\mathbf{K}_-}}{F_{\mathbf{K}_+} + F_{\mathbf{K}_-}}. \tag{2.120}$$

It can be seen from Fig. 2.9, that it is possible to manipulate the degree of valley polarization along a given direction by changing the polarization of the excitation. Furthermore, since it is possible for different directions to have both different valley polarizations and different momentum, a linearly polarized excitation will result in the spatial separation of carriers belonging to different valleys. This fact coupled with the suppression of inter-valley and backscattering, should result in the accumulation of photo-excited carriers belonging to different valleys at different edges of a light spot from an illuminating laser beam.

This effect can be measured by applying an electric field in the graphene plane. This will enhance (retard) the motion of electrons aligned parallel (anti-parallel) to the field which will in turn break the $g(\varphi_{\mathbf{q}}) = g(\varphi_{\mathbf{q}} + \pi)$ symmetry of the momentum distribution function. The resulting weak birefringence can be detected by a linearly polarized probe pulse whose polarization

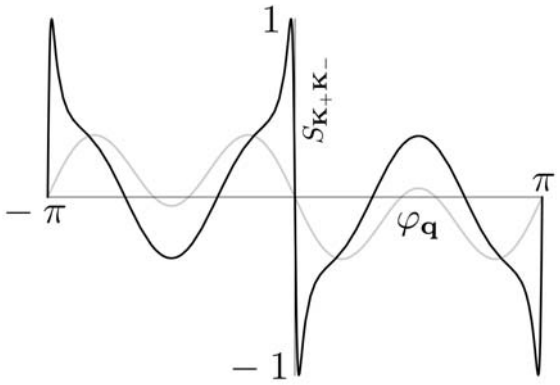

Figure 2.9: For the fixed frequency of excitation, $\nu = 0.6\,|t|\,/h$, the degree of valley polarisation for two different polarisation angles $\varphi_{\mathbf{e}} = 0$ (black line) and $\varphi_{\mathbf{e}} = \pi/2$ (grey line) is shown. (Note, though it is possible to achieve full valley polarsation i.e. $S_{\mathbf{KK'}} = 1$, at such values of $\varphi_{\mathbf{q}}$ the angular generation density is limited.)

axis is orientated 45 degrees to the pump. This is somewhat similar to using the Faraday effect to detect spin orientation along different edges of the sample in the spin Hall effect [66, 67] or the optical spin Hall effect [68].

2.6 Conclusion

In conclusion, we have calculated the momentum distribution function of photo-excited carriers created by linearly polarized light in single layer graphene. The momentum distribution function is highly anisotropic and the alignment is dictated by the orientation of the polarization vector. This phenomena offers an experimental tool to generate highly directional photo-excited carriers within the bulk which would assist in the investigation of "direction dependent phenomena". It was shown that, in the weak pumping regime, the HPL is completely depolarized after relaxing via the interaction with long-wavelength optical phonons intrinsic to graphene; whereas the relaxation of hot electrons via the coupling to bulk optical phonons in silicon carbide does not. Therefore by looking at the degree of polarization of the HPL one should be able to determine the dominant relaxation mechanism for graphene on SiC. Furthermore, by studying the depolarization of HPL in a magnetic field allows one to obtain the momentum relaxation times of hot electrons. It is predicted that the depolarization of hot photoluminescence will be as useful to graphene as it was to studying relaxation processes in conventional 2D systems. It has also been shown that in the high energy regime, i.e. in the presence of trigonal warping, one must take into account contributions from both Dirac points to achieve a physically meaningful result. This warping has also been shown to be a means to spatially separate carriers belonging to different valleys, therefore opening the door to an optical means of controlling valley polarization (optovalleytronics) and quantum

computing in graphene.

Chapter 3

Carbon-based nanostructures as terahertz emitters and detectors

3.1 Introduction

A single wall nanotube (SWNT) is formed by rolling a graphene sheet into a seamless cylinder [35, 69, 70, 71]. The length to diameter ratios are such that these nanostructures (in terms of kinetics) can be considered as one dimensional systems. The manner in which the tube is rolled strongly dictates its electronic properties; the SWNT can either be metallic, a narrow-gap semiconductor or semiconducting with a band gap of the order of 1 eV.

Within the frame of a simple zone-folding model of the π-electron graphene spectrum, armchair and quasi-metallic carbon nanotubes can be considered as one-dimensional analogs of graphene, since in this model the electron low-energy spectrum is linearly dependent on the electron wave vector. The electron energy spectrum, $\xi(q_T)$, of the aforementioned SWNTs is given by $\xi(q_T) = \pm\hbar v_{\mathrm{F}} |q_T|$, where q_T is measured from where the conduction and valence bands coincide and $v_{\mathrm{F}} \approx 9.8 \times 10^5$ m/s is the Fermi velocity of graphene. However, due to curvature effects quasi-metallic SWNTs are in fact narrow-gap semiconductors whose band gaps can be of the order of terahertz.

Terahertz radiation lies between its better studied counterparts; microwave and infrared radiation, in the electromagnetic spectrum. Filling the so-called "terahertz gap" is a challenging area in modern device physics [72] for this region of the electromagnetic spectrum presents difficulties in both generating coherent sources and creating sensitive detectors. However the rewards of exploiting this gap are great, owing to the diverse applications of terahertz radiation. Potential applications range from medical imagining, security and communication through to astrophysics. The

unique position of the terahertz range, in the gap between the parts of electromagnetic spectrum which are accessible by either electronic or optical devices, leads to an unprecedented diversity in approaches to bridging this gap [73, 74, 75, 76]. One approach is to utilize graphene and its one dimensional counterpart, the carbon nanotube [77] whose optical and electronic properties are as interesting and diverse as their potential applications. In the presence of applied magnetic and electric fields, certain types of SWNTs develop strong terahertz optical transitions, giving rise to the possibility of utilizing them as highly tunable, optically-active materials for terahertz applications [39, 78, 79, 80, 81, 82]. One may envisage, for example, a terahertz laser based on a SWNT gain material - a tantalizing prospect given the dearth of current light-weight, compact terahertz sources.

In this chapter the terahertz optical properties of carbon nanostructures are investigated and numerous devices for terahertz emitters and detectors are proposed for both the one and two dimensional forms of graphene. The variety of approaches proposed is a testament to the broad breadth of novel properties these allotropic forms of carbons have. The first scheme is based upon the electric-field induced heating of the electron gas in quasi-metallic carbon nanotubes resulting in a population inversion of optically active states with an energy difference within the terahertz spectrum range. In the ballistic transport regime their spontaneous emission spectra have a universal frequency and bias voltage dependence, which raises the possibility of utilizing this effect for high-frequency nanoelectronic devices.

The second scheme utilizes the inherent curvature of carbon nanotubes. Namely, the same intrinsic curvature which opens the gap in the quasi-metallic carbon nanotubes spectrum also allows optical transitions in the terahertz range. The influence of curvature on the band structure of quasi-metallic nanotubes is analogous to the role of the magnetic field from Ref. [81]. The means by which the intrinsic curvature of semi-metallic carbon nanotubes could be utilized to generate terahertz radiation is discussed.

Many-body (excitonic) effects, which dominate the optical properties of semiconducting SWNTs [83], are also important in narrow-gap nanotubes. However, it is shown that due to the quasi-relativistic character of the free-particle dispersion near the band edge of the narrow-gap SWNTs, there is a spectacular decrease in the exciton binding energy, thus these effects do not alter significantly the main results of the aforementioned scheme.

After the discussion of excitonic effects we return back to graphene. As a gapless semiconductor with ultra-high carrier mobility, graphene is a natural material for detecting terahertz radiation. The third proposal utilizes the effect of momentum alignment of photo-excited carriers in graphene, in conjunction with an electrostatically defined potential, to form a graphene-based polarization

sensitive terahertz detector with sub-wavelength resolution.

3.2 The crystallographic structure of carbon nanotubes

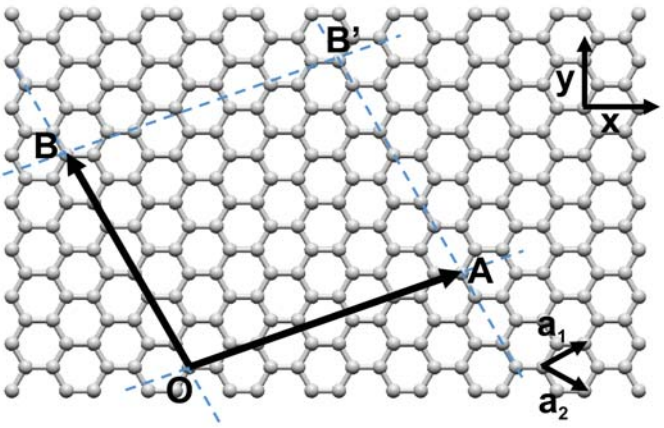

Figure 3.1: An unrolled carbon nanotube. The cylinder is formed by rolling the graphene sheet such that points O and A and points B and B' coincide with one another. The vectors OA and OB' define the vectors $\mathbf{C_h}$ and $\mathbf{T}$ respectively. $\mathbf{a_1}$ and $\mathbf{a_2}$ are the graphene primitive lattice vectors.

The primitive unit cell of a SWNT is defined by the primitive lattice vectors $\mathbf{C_h}$ and $\mathbf{T}$, which are called the chiral and translation vector respectively. The former is the vector which traverses the circumference, the latter is the vector which runs along the seam. These vectors can be most easily seen by unrolling the tube into a rectangular sheet as shown in Fig. 3.1. Two of its edges are defined by the vector $\mathbf{C_h}$ whereas the remaining two are defined by the vector $\mathbf{T}$.

The chiral vector, $\mathbf{C_h}$, is defined via the graphene primitive lattice vectors ($\mathbf{a_1}$, $\mathbf{a_2}$) given in Eq. (2.1):

$$\mathbf{C_h}\,(n,m) = n\mathbf{a_1} + m\mathbf{a_2} \equiv (n,m)\,, \tag{3.1}$$

where n and m are integers. The armchair and zig-zag SWNT chiral vectors are given by $\mathbf{C_h} = (n,n)$ and $\mathbf{C_h} = (n,0)$ respectively. The magnitude of the chiral vector,

$$|\mathbf{C_h}| = a\sqrt{n^2 + m^2 + nm}, \tag{3.2}$$

defines the circumferential length of the tube and hence $|\mathbf{C_h}|/\pi$ defines the tubes diameter. Here $a = \sqrt{3}a_{CC}$, where a_{CC} is the nearest neighbor distance between two carbon atoms which is given as 1.42 Å. For example, a SWNT defined by $(10,10)$ has a diameter of 1.4 nm.

The translational vector, $\mathbf{T}$, is defined as the vector which starts from one corner of the rectangle

and ends on the first lattice point which repeats the cross-section defined by $\mathbf{C_h}$, and is defined via the graphene primitive lattice vectors given in Eq. (2.1) as:

$$\mathbf{T}\left(t_1, t_2\right) = t_1\mathbf{a_1} + t_2\mathbf{a_2}. \tag{3.3}$$

t_1 and t_2 are found by the condition that $\mathbf{C_h} \cdot \mathbf{T} = 0$, therefore

$$t_1 = 2m + n; \qquad t_2 = -\left(2n + m\right) \ . \tag{3.4}$$

Since $\mathbf{T}$ is a primitive lattice vector, we require the smallest combination of m and n which satisfies the above relation, hence

$$t_1 = \left(2m + n\right)/d_R; \qquad t_2 = -\left(2n + m\right)/d_R \ , \tag{3.5}$$

where d_R is the greatest common divisor (i.e. the highest common factor) of $2m + n$ and $2n + m$. The magnitude of $\mathbf{T}$ can be expressed in terms of the circumferential length of the tube via the relation

$$\begin{aligned} |\mathbf{T}| &= a\sqrt{t_1^2 + t_2^2 + \tfrac{1}{2}t_1 t_2}, \\ &= a\sqrt{3\left(m^2 + n^2 + nm\right)}/d_R, \\ &= \sqrt{3}\left|\mathbf{C_h}\right|/d_R. \end{aligned} \tag{3.6}$$

The primitive unit cell contains N hexagons, where

$$N = \frac{|\mathbf{T} \times \mathbf{C_h}|}{|\mathbf{a_1} \times \mathbf{a_2}|} = \frac{\left|\mathbf{C_h}\right||\mathbf{T}|}{a^2 \sin\left(\frac{\pi}{3}\right)} = \frac{2}{a^2 d_R}\left|\mathbf{C_h}\right|^2 \tag{3.7}$$

Since each hexagon contains two carbon atoms there are thus a total of $2N$ carbon atoms per unit cell. The highest symmetry tubes (i.e. those which have the smallest unit cell) are the armchair and zig-zag SWNTs, they are so named due to the resemblance of their cross-sections as shown in Fig. 3.2. These tubes are crucial in studying how the band structure of SWNTs can be modified for device applications. Owing to the fact that they admit simple analytic solutions due to their symmetry and therefore offer invaluable insights. Furthermore, their results can often be generalized to SWNTs with similar spectra.

The reciprocal lattice vectors corresponding to the vectors $\mathbf{C_h}$ and $\mathbf{T}$ are

$$\mathbf{K_C} = \frac{2\pi}{aN}\left(\frac{1}{\sqrt{3}}\left(t_1 - t_2\right), -\left(t_1 + t_2\right)\right) \tag{3.8}$$

and

$$\mathbf{K_T} = \frac{2\pi}{aN}\left(\frac{1}{\sqrt{3}}\left(n - m\right), -\left(n + m\right)\right) \tag{3.9}$$

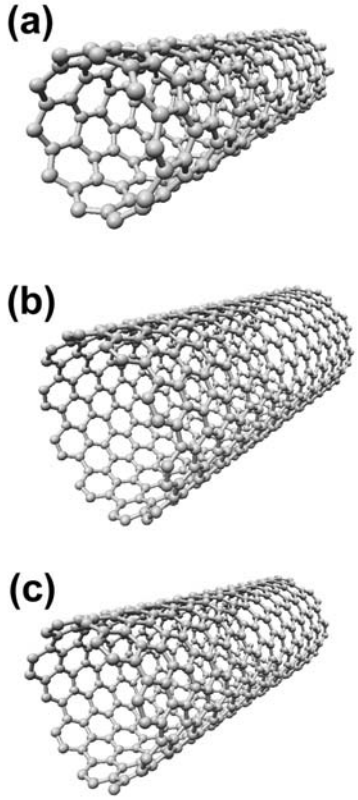

Figure 3.2: A selection of single-walled carbon nanotubes, each formed by rolling a graphene sheet in a different way. (a) is a (10,0) zig-zag nanotube, (b) is a (10,10) armchair nanotube and (c) is a (7,10) chiral nanotube.

respectively, and can be defined via the graphene reciprocal lattice vectors given in Eq. (2.2) as [69]

$$\mathbf{K_C} = \frac{1}{N}\left(-t_2\mathbf{b_1} + t_1\mathbf{b_2}\right); \qquad \mathbf{K_T} = \frac{1}{N}\left(-m\mathbf{b_1} + n\mathbf{b_2}\right). \tag{3.10}$$

In rolling graphene to form a tube, motion is quantized along the circumferential direction, one can therefore decompose the electron wave vector, $\mathbf{k}$, into two projections. One along the circumference (that which is quantized) and one along the nanotube axis (that which is free), these components shall be called $\mathbf{k_C}$ and $\mathbf{k_T}$ respectively. The projection of the wave vector along the circumference is given by the expression

$$k_C = \mathbf{k} \cdot \frac{\mathbf{C_h}}{|\mathbf{C_h}|} \tag{3.11}$$

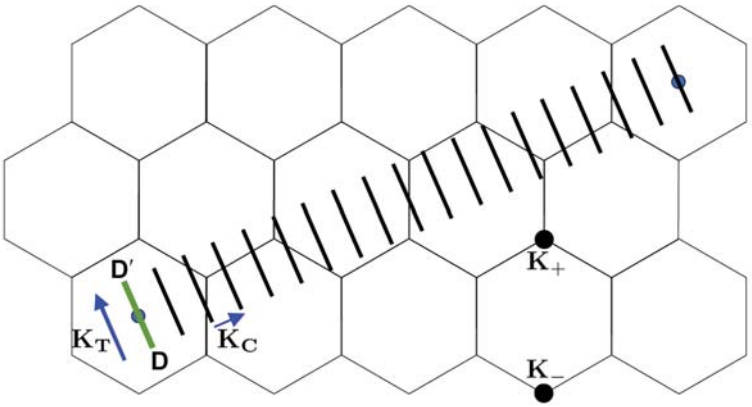

Figure 3.3: The Brillouin zone of a carbon nanotube is represented by the line $\mathbf{DD'}$. The blue arrows represent the vectors $\mathbf{K_C}$ and $\mathbf{K_T}$, which are the reciprocal lattice vectors corresponding to the vectors $\mathbf{C_h}$ and $\mathbf{T}$ respectively.

and the projection of the wave vector along translational vector is

$$k_T = \mathbf{k} \cdot \frac{\mathbf{T}}{|\mathbf{T}|} \tag{3.12}$$

Let us first consider the quantized component. The periodic boundary condition imposed on the wavefunction leads to the condition,

$$k_C = l\frac{2\pi}{|\mathbf{C_h}|}, \tag{3.13}$$

where l plays the role of the particles angular momentum and is an integer number ranging from 1 to $2N$. Therefore, the wave vector $\mathbf{k_C}$ can be expressed as

$$\mathbf{k_C} = l\mathbf{K_C} = \frac{l}{N}\left(-t_2\mathbf{b_1} + t_1\mathbf{b_2}\right), \tag{3.14}$$

where t_1 and t_2 are integers which do not share a common divisor greater than unity. Therefore the quantity l/N is always fractional except for the case of $l = N$. When this condition is met, $\mathbf{k_c}$ corresponds to a graphene reciprocal lattice point, whereas none of the remaining $N-1$ possible wave vectors lie on a lattice point. For the unbounded component of momentum, the projection of the wave vector along the nanotube axis is continuous and along the $\mathbf{K_T}$ direction. As can be seen from Fig. 3.3 the wave vectors describing electron motion form a set of 1D lines directed along the $\mathbf{K_T}$ direction, separated by $2\pi/|\mathbf{C_h}|$ in the $\mathbf{K_C}$ direction. There are therefore $2N$ distinct bands (i.e. N conduction bands and N valence bands) which lie within the SWNT 1st Brillouin zone, each of length $\frac{2\pi}{|\mathbf{T}|}$. In some SWNTs, finite length-quantization has been experimentally observed [84]. However, in this thesis all the tubes considered are sufficiently long such that k_T can be treated as a continuous variable.

3.3 The band structure of carbon nanotubes

3.3.1 Introduction

By rolling graphene into a cylinder, one reduces the dimensionality in k-space, and as mentioned in the introduction, the manner in which the tube is rolled strongly dictates the carbon nanotubes band structure. In this thesis the tubes of the foremost interest are the so called armchair and quasi-metallic classes of SWNTs, the former is defined by $n = m$ and the later by $n - m = 3p$, where p is a non-zero integer. They are both gapless within the frame of a simple zone-folding model of the π-electron graphene spectrum and their low electron energy spectrum is linearly dependent on the electron wave vector. Therefore, within this model the charge carriers behave as one dimensional massless Dirac fermions. However, due to curvature effects, quasi-metallic SWNTs are in fact narrow-gap semiconductors and thus their charge carriers behave as massive one dimensional Dirac fermions.

In what follows, the electron energy spectrum for a (n, m) nanotube is derived using the zone folding model of the π-electron graphene spectrum. From this result, the low energy spectrum for quasi metallic nanotubes is obtained. Finally, the effective matrix Hamiltonian which describes quasi-metallic tubes is found.

3.3.2 The zone-folding model

From chapter one, Eq. (2.20), the energy spectrum of graphene's charge carriers was found to be:

$$\xi_b = s\,|t|\sqrt{1 + 4\cos\left(\frac{\sqrt{3}}{2}ak_x\right)\cos\left(\frac{1}{2}ak_y\right) + 4\cos^2\left(\frac{1}{2}ak_y\right)} \tag{3.15}$$

Due to the manner in which motion is quantized, it is more convenient to resolve the electron's wave vector into components directed along the primitive unit vectors of the SWNT. k_x and k_y are related to k_C and k_T via the relation:

$$k_x\mathbf{i} + k_y\mathbf{j} = k_C\frac{\mathbf{C_h}}{|\mathbf{C_h}|} + k_T\frac{\mathbf{T}}{|\mathbf{T}|}. \tag{3.16}$$

Using the identity Eq. (3.6) and equating the Cartesian projections of Eq. (3.16), k_x and k_y can be expressed in terms of k_C and k_T by:

$$k_x = \frac{a}{2\,|\mathbf{C_h}|}\left[\sqrt{3}k_C\,(n+m) + k_T\,(m-n)\right]; \tag{3.17}$$

$$k_y = \frac{a}{2\,|\mathbf{C_h}|}\left[k_C\,(n-m) + \sqrt{3}k_T\,(m+n)\right]. \tag{3.18}$$

To obtain the electron energy spectrum for a carbon nanotube defined by (n, m), one must substi-

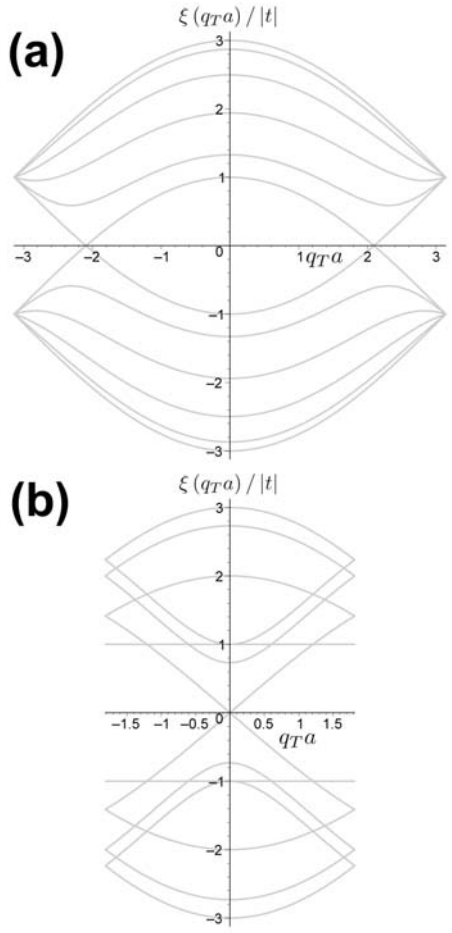

Figure 3.4: The electron energy spectrum for: (a) an armchair SWNT, with (n,m) = (5,5), (b) a zig-zag SWNT, with (n,m) = (6,0).

tute the definitions of k_x, k_y and k_C from Eq. (3.17), Eq. (3.18) and Eq. (3.13) respectively, into graphene's energy spectrum:

$$\xi_b = s\,|t| \left\{ 1 + 4\cos^2\left(\frac{1}{4}\frac{a^2}{|\mathbf{C_h}|}\left[\frac{2\pi\,(n-m)}{|\mathbf{C_h}|}l + \sqrt{3}\,(m+n)\,k_T\right]\right) + 4\cos\left(\frac{\sqrt{3}}{4}\frac{a^2}{|\mathbf{C_h}|}\left[\frac{2\pi\,(n+m)\,\sqrt{3}}{|\mathbf{C_h}|}l + (m-n)\,k_T\right]\right)\cos\left(\frac{1}{4}\frac{a^2}{|\mathbf{C_h}|}\left[\frac{2\pi\,(n-m)}{|\mathbf{C_h}|}l + \sqrt{3}\,(m+n)\,k_T\right]\right)\right\}^{\frac{1}{2}} \tag{3.19}$$

From Eq. (3.19), the electron energy spectrum of an armchair and zig-zag nanotube, denoted by $\xi_{\mathrm{arm}}\,(k_T)$ and $\xi_{\mathrm{zig}}\,(k_T)$ respectively, are found to be

$$\xi_{\mathrm{arm}}\,(k_T) = s\,|t| \sqrt{1 + 4\cos\left(\pi\frac{l}{n}\right)\cos\left(k_T\frac{a}{2}\right) + 4\cos^2\left(k_T\frac{a}{2}\right)}; \tag{3.20}$$

$$\xi_{\text{zig}}\left(k_T\right) = s\left|t\right|\sqrt{1+4\cos\left(\frac{\sqrt{3}a}{2}k_T\right)\cos\left(\pi\frac{l}{n}\right)+4\cos^2\left(\pi\frac{l}{n}\right)}, \tag{3.21}$$

and are plotted in Fig. 3.4. Note, that for convenience the zig-zag SWNT was defined by $(n,-n)$.

3.3.3 Narrow gap nanotubes

In rolling graphene to form a SWNT, the available electron wave vectors become restricted, forming continuous parallel lines separated by a distance $2\pi/\left|\mathbf{C_h}\right|$ in k-space. Each line cuts through the manifold defined by $\xi_b = s\left|t\right|\sqrt{\left|f_k\right|^2}$, the projection of each cut forms the N conduction (valence) bands. In the low energy regime, graphene's electron energy spectrum is conical, therefore the lines must intersect the Dirac point to result in a truly linear nanotube spectrum. This criteria is satisfied by the condition $n-m=3p$.

From the above consideration, to obtain a linear spectrum by crossing the $\mathbf{K}_\pm$ point, the components k_x and k_y must satisfy the following relations:

$$k_x = \frac{a}{2\left|\mathbf{C_h}\right|}\left[\sqrt{3}k_C\left(n+m\right)+k_T^{min}\left(m-n\right)\right]=0; \tag{3.22}$$

$$k_y = \frac{a}{2\left|\mathbf{C_h}\right|}\left[k_C\left(n-m\right)+\sqrt{3}k_T^{min}\left(m+n\right)\right]=\pm\frac{4\pi}{3a}, \tag{3.23}$$

where the value of k_T for which the bands cross is denoted by $k_T = k_T^{\min}$. The above conditions are met when

$$l = \pm\frac{(n-m)}{3}. \tag{3.24}$$

This gives the band index that corresponds to the highest occupied (lowest unoccupied) valence (conduction) band and hence the crossing point occurs at

$$k_T^{min} = \pm\frac{2\pi\left(n+m\right)}{\sqrt{3}\left|\mathbf{C_h}\right|}. \tag{3.25}$$

Notably, this point shifts depending on the values of n and m, except for the case of the zig-zag quasi-metallic nanotube, where the crossing point is always at $k_T = 0$. As in the case of graphene, it is the behavior of the spectrum around these crossing points which is of the foremost interest since we are interested in terahertz applications. Therefore, it is more appropriate to measure momentum relative to these points, namely, $q_T = k_T - k_T^{min}$. The Cartesian components of momentum thus become

$$k_x = \frac{(m-n)}{2\left|\mathbf{C_h}\right|}\left(aq_T\right), \tag{3.26}$$

$$k_y = \pm\frac{4\pi}{3a} + \frac{\sqrt{3}}{2\left|\mathbf{C_h}\right|}\left(m+n\right)\left(aq_T\right). \tag{3.27}$$

The low energy spectrum of a quasi-metallic SWNT is obtained by substituting Eqs. (3.26-3.27) into the graphene electronic spectrum Eq. (2.20). The result of performing a Taylor series expansion in q_T and retaining only first order terms is:

$$\xi_b\left(q_T\right) = sv_{\mathrm{F}}\hbar\left|q_T\right|$$

The particle's energy is linearly dependent on the electron wave vector q_T and thus it behaves as a one dimensional massless Dirac fermion. The full spectrum, obtained from this simple zone folding model, for a $(4,1)$ quasi-metallic SWNT is shown in Fig. 3.5.

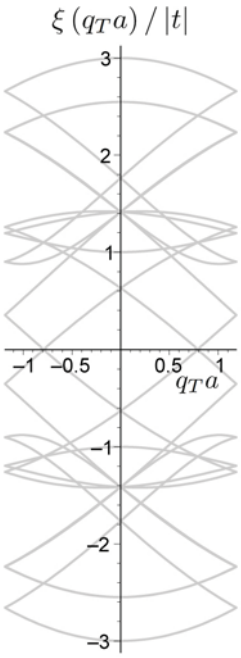

Figure 3.5: The electron energy spectrum for a quasi-metallic tube defined by (n,m) = (4,1)

3.3.3.1 The effective matrix Hamiltonian

As in the case of energy, the matrix Hamiltonian which describes quasi-metallic SWNT charge carriers motion can be obtained by applying the circumferential boundary conditions, imposed upon the system in the act of rolling, to the flat graphene sheet's matrix Hamiltonian, which was found in chapter 1 to be

$$H_{\mathrm{eff}} = -\left|t\right|\begin{bmatrix} 0 & f_k \\ f_k^{\star} & 0 \end{bmatrix}, \tag{3.28}$$

which acts on a two-component Dirac wavefunction given by

$$\begin{pmatrix} C_1 \\ C_2 \end{pmatrix}, \tag{3.29}$$

where C_1 and C_2 are the wavefunctions associated with the A and B sub-lattices of graphene respectively and

$$f_k = \left[e^{i\left(\frac{a}{\sqrt{3}}k_x\right)} + 2e^{i\left(-\frac{a}{2\sqrt{3}}k_x\right)} \cos\left(k_y \frac{a}{2}\right) \right]. \tag{3.30}$$

To obtain the charge carrier behavior at low energy, Eq. (3.30) is re-expressed in terms of q_T using the identities Eq. (3.26) and Eq. (3.27) and then a series expansion in q_T to first order is performed, this yields the simple expression

$$f_k = \left[-(m+n) + \frac{1}{\sqrt{3}}(m-n)\, i \right] (aq_T) \frac{3a}{4\left|\mathbf{C_h}\right|} \equiv -\frac{\sqrt{3}}{2} a e^{i\Theta} q_T, \tag{3.31}$$

where $\Theta = \arctan\left(-\frac{1}{\sqrt{3}}\frac{(m-n)}{(m+n)}\right)$. This allows the effective matrix Hamiltonian for all quasi-metallic nanotubes to be expressed as

$$H_{\text{eff}} = \hbar v_{\text{F}} \begin{bmatrix} 0 & e^{i\Theta} q_T \\ e^{-i\Theta} q_T & 0 \end{bmatrix}. \tag{3.32}$$

By changing the basis wavefunctions from C_1 and C_2 to $D_1 = C_1$ and $D_2 = e^{i\Theta} C_2$ the effective matrix Hamiltonian can be expressed as

$$\tilde{H}_{\text{eff}} = \hbar v_{\text{F}} \begin{bmatrix} 0 & q_T \\ q_T & 0 \end{bmatrix} \tag{3.33}$$

which now acts on the on two-component Dirac wavefunction of the form:

$$\begin{bmatrix} D_1 \\ D_2 \end{bmatrix}. \tag{3.34}$$

Hence, by appropriate transformations, one can reduce the low energy effective matrix Hamiltonian of any quasi-metallic tube to that of one describing a one dimensional massless Dirac fermion. However, due to curvature effects the nature of quasi-metallic SWNTs charge carriers changes from massless to massive, and the effective matrix Hamiltonian, Eq. (3.33) becomes of the form,

$$\tilde{H}_{\text{eff}} = \hbar v_{\text{F}} \begin{bmatrix} 0 & q_T \\ q_T & 0 \end{bmatrix} + \begin{bmatrix} m_0 v_{\text{F}}^2 & 0 \\ 0 & -m_0 v_{\text{F}}^2 \end{bmatrix}, \tag{3.35}$$

where m_0 is the effective mass due to curvature. The resulting electron energy spectrum, $\xi(q_T)$, is given by

$$\xi_b = s\sqrt{(m_0 v_{\mathrm{F}}^2)^2 + \hbar^2 q_T^2 v_{\mathrm{F}}^2}. \tag{3.36}$$

3.4 Terahertz applications

In the last decade there has been significant progress made in the development of ultra-fast laser based terahertz sources [85], quantum cascade [86] and free electron lasers [87] which operate in the terahertz range as well as Synchrotron based terahertz sources [88]. However, current terahertz sources and detectors often suffer from low output power, are often considerable in size and operate at liquid helium temperatures. For this reason, the search for ultra-bright, coherent, compact terahertz sources and detectors is one of the key areas of modern applied physics [89].

The potential applications of terahertz radiation are extensive and far reaching. For example, the vibrational breathing modes of many large molecules occur in the terahertz domain making terahertz spectroscopy a potentially powerful tool for the identification and characterization of biomolecules [90, 91, 92, 93, 94]. Furthermore, the non-ionizing nature of terahertz radiation means it is seen by many as the future of imaging technology and it also has promising applications in biomedicine and biosensing. As well as utilizing terahertz technology for pharmaceutical research [95] and biomedical diagnostic devices, other potential uses range from security applications such as the sensing and detection of biological hazards and explosives [72], through to communication technology and astrophysics.

There are several promising proposals of using carbon nanotubes for terahertz applications including: a nanoklystron utilizing extremely efficient high-field electron emission from nanotubes [77, 96, 97]; devices based on negative differential conductivity in large-diameter semiconducting nanotubes [98, 99]; high-frequency resonant-tunneling diodes [100] and Schottky diodes [101, 102, 103, 104]; as well as electric-field-controlled carbon nanotube superlattices [78]; frequency multipliers [105, 106]; terahertz amplifiers [107], switches [108] and antennas [109]. In the forthcoming sections three proposals for terahertz applications are presented: two using quasi-metallic tubes and one using graphene.

3.5 Generation of terahertz radiation by hot electrons in carbon nanotubes

3.5.1 Introduction

Applying a voltage across the ends of a quasi-metallic carbon nanotube results in the emission of terahertz radiation. This scheme is based on the electric-field induced heating of an electron gas, which results in a population inversion of optically active states with an energy difference within the terahertz spectrum range. It is well-known that the elastic backscattering processes in metallic SWNTs are strongly suppressed [110, 111] and in a high enough electric field charge carriers can be accelerated up to the energy allowing the emission of optical/zone-boundary phonons. At this energy, corresponding to a frequency of about 40 terahertz, the major scattering mechanism switches on abruptly, resulting in current saturation [112, 113, 114, 115]. In what follows it is shown that, for certain types of carbon nanotubes, the heating of electrons to energies below the high-energy phonon emission threshold results in spontaneous terahertz emission whose peak frequency is controlled by an applied voltage.

3.5.2 Population inversion of optically active states

The ballistic transport of carriers in sub-micron CNTs at room temperature for bias voltages up to 0.16 V is perhaps one of most well-known features of metallic CNTs. When a voltage, V, is applied between the ends of a quasi-metallic SWNT, the whole voltage drop occurs within the narrow regions close to the contacts, while in the inner regions of the carbon nanotube the voltage is constant [71]. The non-equilibrium carriers, which are generated ("injected") and accelerated in the narrow high-field areas near the contacts, travel ballistically through the nanotube interior, where they have a chance to recombine, emitting terahertz photons. In the ballistic or so-called "low-bias" regime [113, 114], (which persists for sub-micron SWNTs for applied voltages up to $V \approx 0.16\,\mathrm{V}$) the experimentally observed current, I, is,

$$I \approx 4\frac{e^2}{h}V. \tag{3.37}$$

When the bias voltage exceeds 0.16 V the fast emission of high-energy phonons causes the current to saturate at $I_s \approx 4\,(e/h)\,\hbar\Omega$, where $\hbar\Omega = 0.16$ eV is the energy of zone-edge phonons associated with ultrafast electron-phonon scattering rates [114]. For the case of ideal Ohmic contacts [113], which we will suppose from now on, conservation of energy requires that an electron moving from one contact to another gains a total energy $\Delta\varepsilon = eV$, hence

$$I = 4\frac{e}{h}\Delta\varepsilon. \tag{3.38}$$

The energy spectrum near the crossing of the valence and conduction bands in single walled metallic CNTs is linear, therefore, the speed of all charged particles, which corresponds to the slope of the spectrum $v = \frac{1}{\hbar}\frac{\partial\varepsilon}{\partial q}$, is the same ($v = v_F$). This speed does not depend on energy (or momentum) in a broad range of energies (up to 0.5 eV for CNTs of small enough radii). Herein the zero of energy is defined as the Fermi energy position in the absence of an external field. Since all electrons have the same speed v_{F}, the electron component of the total current is given by

$$I_e = \frac{ev_{\mathrm{F}}}{L}\left|\triangle N_e\right|, \tag{3.39}$$

where L is the nanotube length and $\triangle N_e$ is the difference between the number of electrons moving towards one end of the nanotube and its other end. In turn, $|\triangle N_e|$ is given by

$$\left|\triangle N_e\right| = 4 \times \frac{L}{2\pi}\int f_e\left(k\right)dk, \tag{3.40}$$

where the factor 4 reflects the degeneracy of electronic states in carbon nanotubes (two-fold spin degeneracy and two-fold "valley" degeneracy) therefore,

$$I_e = 4\frac{ev_{\mathrm{F}}}{2\pi}\int f_e\left(k\right)dk. \tag{3.41}$$

Due to electron-hole symmetry, the contribution to the total current from holes is exactly the same as that from electrons. For Eq. (3.41) to be equal to $I_e = 2\left(e/h\right)\triangle\varepsilon$ the hot electron distribution function must be of the form,

$$f_e\left(q_T\right) = \begin{cases} 1, & 0 < q_T < \Delta\varepsilon/2\hbar v_{\mathrm{F}}, \\ 0, & q_T > \Delta\varepsilon/2\hbar v_{\mathrm{F}}, \end{cases} \tag{3.42}$$

and the distribution function for hot holes, $f_h\left(q_T\right)$, has the same form as $f_e\left(q_T\right)$. This distribution simultaneously satisfies conservation of energy and sustains the experimentally observed values of current in the low-bias regime. In fact, using this distribution is the only way to explain the observed transport properties of metallic nanotubes shorter than $l_{ac} \approx 2\mu$m at bias voltages below the 0.16 V threshold. Therefore, applying a bias voltage across the ends of a quasi-metallic SWNT results in the electron distribution being shifted, in the way shown by the heavy lines in Fig. 3.6 which correspond to the filled electron states.

This shift causes a population inversion which results in optical transitions between the filled

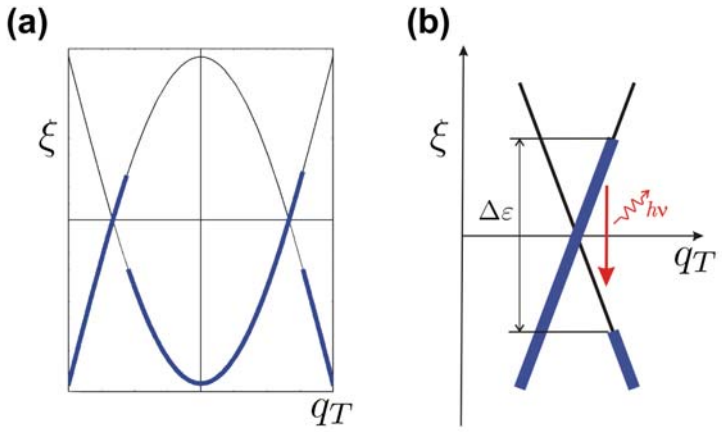

Figure 3.6: (a) Crossing valence and conduction subbands in metallic SWNTs. The thick lines show the states occupied by electrons in the presence of an applied bias voltage. (b) The scheme of terahertz photon generation by hot carriers. Figure adapted from Ref. [39]

states in the conduction band and empty states in the valence band. The spectrum of optical transitions is determined by the distribution function of hot carriers, which in turn depends on the applied voltage and scattering processes in the SWNT. In high-quality nanotubes disorder-mediated scattering is known to be weaker than electron-phonon scattering [112, 113, 114, 115]. Since the scattering processes erode the inversion of the electron population, an optimal condition for observing the discussed optical transitions takes place when the length of the SWNT, $L < l_{ac}$, where the electron mean-free path for acoustic phonon scattering is $l_{ac} \approx 2.4\ \mu m$ [114]. Below we shall consider only short SWNTs in the ballistic transport regime, where the total shift, $\Delta\varepsilon$, of the electron distribution (see Fig. 3.6 (b)) does not exceed the value of $\hbar\Omega = 0.16\ e\mathrm{V}$.

Let us select a SWNT with the crystal structure most suitable for the observation of terahertz emission from a biased nanotube. First, the required nanotube should have metallic conductivity and second, the optical transitions between the lowest conduction subband and the top valence subband should be allowed. The only SWNTs with a truly metallic energy band structure are the armchair (n, n) SWNTs [70, 116, 117, 118, 119] . However, the optical transitions between the first conduction and valence subbands are strictly forbidden by symmetry [120, 121]. The next logical candidate to use for the observation of terahertz generation are the so-called quasi-metallic (n, m) SWNTs with $n - m = 3p$, where p is an non-zero integer. These nanotubes are gapless within the frame of a simple zone-folding model of the π-electron graphene spectrum [35], but are in fact narrow-gap semiconductors due to curvature effects. Their band gap is given by [116, 119]:

$$\xi_g = \frac{\hbar v_F a_{CC} \cos 3\theta}{8R^2}, \tag{3.43}$$

where R is the nanotube radius, and $\theta = \arctan[\sqrt{3}m/(2n+m)]$ is the chiral angle [35]. In ballistic

one-dimensional structures the whole voltage drop occurs in the narrow regions close to the contacts where the carriers are accelerated [71]. The presence of a band gap imposes a threshold voltage which must be exceeded in order for current to flow through the carbon nanotube. For Zener break down to occur the potential energy of the particle must exceed the band gap, thereby allowing quantum tunneling from the valence band into the conduction band.

Let us assume that the electric field in the narrow regions close to the contacts is constant, therefore the electrostatic potential is given by $U = eEx$. Due to curvature effects the energy spectrum near the band edge is given by $\xi_b = s\sqrt{\xi_g^2/4 + \hbar^2 v_F^2 q_T^2}$. In this instance the probability of tunneling across the band gap is given by

$$\exp\left(-2\int_{x_1}^{x_2} |\kappa|\, dx\right), \tag{3.44}$$

where $|\kappa| = \sqrt{\xi_g^2/4 - (U-\xi)^2}/\hbar v_F$ and x_1 and x_2 are the classical turning points . By taking U and ε to be zero at $x = 0$ the tunneling probability becomes

$$\exp\left(-\frac{2}{\hbar v_F}\int_{x_1}^{x_2} \sqrt{\xi_g^2/4 - U^2}dx\right), \tag{3.45}$$

where the classical turning points are defined as $x_1 = -\varepsilon_g/2eE$ and $x_2 = \varepsilon_g/2eE$. The probability of tunneling can be re-expressed in terms of purely potential energy yielding

$$\exp\left(-\frac{4}{eE\hbar v_F}\int_{0}^{\varepsilon_g/2} \sqrt{\xi_g^2/4 - U^2}dU\right), \tag{3.46}$$

invoking the change of variable $U = (\xi_g/2)\sin(t)$ results in

$$\exp\left(-\frac{\xi_g^2}{eE\hbar v_F}\int_{0}^{\pi/2} \cos^2(t)\, dt\right). \tag{3.47}$$

Hence the tunneling probability is given by

$$\exp\left(-\frac{\pi}{4}\frac{\xi_g^2}{eE\hbar v_F}\right). \tag{3.48}$$

It can be seen from Eq. (3.43) that the gap decreases rapidly with increasing nanotube radius. Hence for large values of R this gap can be neglected even in the case of moderate applied voltages, due to the Zener tunneling of electrons across the gap. For example, for a zig-zag $(30, 0)$ SWNT the gap is $\xi_g \approx 6$ meV and the Zener breakdown takes place when the electric field , $E \sim 10^{-1}$ V/μm.

Since almost the whole voltage drop in the ballistic regime occurs within the few-nanometer regions near the contacts [71, 122], a typical 0.1 V bias voltage corresponds to an electric field which is more than sufficient to achieve a complete breakdown. The results presented herein are for quasi-metallic SWNTs ($n - m = 3p$ where p is a non-zero integer), of large enough radius R and for an applied bias exceeding the Zener breakdown voltage, such that the finite-gap effects can be neglected.

3.5.3 Optical selection rules

Optical transitions in SWNTs have been a subject of extensive research (see, e.g., Refs. [38, 120, 121, 123, 124, 125, 126]; comprehensive reviews of earlier work can be found in Refs. [69, 70]). The optical selection rules are obtained using the nearest-neighbor orthogonal π-electron tight binding model [35]. Despite its apparent simplicity and well-known limitations, this model has been extremely fruitful in describing low-energy optical spectra and electronic properties of SWNTs (see, e.g., Ref. [127]). The goal is to calculate the spectral density of spontaneous emission, I_ν, which is the probability of optical transitions per unit time with photon frequencies in the interval $(\nu,\ \nu + d\nu)$ divided by $d\nu$. In the dipole approximation [128] this spectral density is given by:

$$I_\nu = \frac{8\pi e^2 \nu}{3c^3} \sum_{i,f} f_e\left(k_i\right) f_h\left(k_f\right) \left|\mathbf{e} \cdot \left\langle \psi_f \left| \hat{v}_z \right| \psi_i \right\rangle\right|^2 \delta\left(\xi_i - \xi_f - h\nu\right), \tag{3.49}$$

where ψ_i and ψ_f are the eigenfunctions of the electrons in the initial and final states, ξ_i and ξ_f are their associated energies, and k_i and k_f are their associated wave-vectors. $\mathbf{e}$ is the polarization of the excitation which we take to be propagating along the carbon nanotube axis. Eq. (3.49) contains the matrix element of the projection of electron velocity along the nanotube axis, which can be derived from graphene's matrix element of velocity by applying the circumferential boundary condition. In the frame of the tight binding model, graphene's matrix element of velocity is given by (see Appendix A.2);

$$\left\langle \psi^C \left| \hat{\mathbf{v}} \right| \psi^V \right\rangle = i \frac{at}{\hbar\sqrt{f_k^2}} \left\{ \frac{1}{\sqrt{3}} \left[\cos\left(\frac{\sqrt{3}a}{2} k_x \right) \cos\left(k_y \frac{a}{2} \right) - \cos\left(k_y a\right) \right] \mathbf{i} \right.$$
$$\left. + \sin\left(k_x \frac{\sqrt{3}a}{2} \right) \sin\left(k_y \frac{a}{2} \right) \mathbf{j} \right\}. \tag{3.50}$$

In section 3.3.3 the following relations for the lowest conduction and highest valence band where found:

$$k_x = \frac{(m-n)}{2\left|\mathbf{C_h}\right|} \left(a q_T\right), \tag{3.51}$$

$$k_y = \left[\frac{4\pi}{3a} + \frac{\sqrt{3}}{2\left|\mathbf{C_h}\right|}\left(m+n\right)\left(aq_T\right)\right]. \tag{3.52}$$

These relations allow the velocity operator between the lowest conduction and highest valence band to be expressed as;

$$\begin{aligned} i\frac{at}{\hbar\sqrt{f_k^2}}\Bigg\{ & \frac{1}{\sqrt{3}}\cos\left(\frac{\sqrt{3}\left(m-n\right)a}{4\left|\mathbf{C_h}\right|}\left(aq_T\right)\right)\cos\left(\frac{2\pi}{3}+\frac{\sqrt{3}a}{4\left|\mathbf{C_h}\right|}\left(m+n\right)\left(aq_T\right)\right)\mathbf{i} \\ & -\frac{1}{\sqrt{3}}\cos\left(\frac{4\pi}{3}+\frac{\sqrt{3}a}{2\left|\mathbf{C_h}\right|}\left(m+n\right)\left(aq_T\right)\right)\mathbf{i} \\ & +\sin\left(\frac{\sqrt{3}\left(m-n\right)a}{4\left|\mathbf{C_h}\right|}\left(aq_T\right)\right)\sin\left(\frac{2\pi}{3}+\frac{a\sqrt{3}}{4\left|\mathbf{C_h}\right|}\left(m+n\right)\left(aq_T\right)\right)\mathbf{j}\Bigg\} \end{aligned} \tag{3.53}$$

The polarization of incident light can be decomposed into two components, that which lies along the nanotube axis and that which is perpendicular to it. Each polarization results in drastically different optical selection rules. Namely, for light polarized along the nanotube axis, transitions occur between subbands with the same angular momentum, whereas for light polarized perpendicular to the axis, transitions occur between subbands which differ in angular momentum by one. For light polarized along the nanotube axis the polarization vector is given by,

$$\mathbf{e} = \frac{\mathbf{T}}{\left|\mathbf{T}\right|} = \frac{1}{\left|\mathbf{T}\right|}\left(t_1\mathbf{a_1} + t_2\mathbf{a_2}\right). \tag{3.54}$$

Using the relations Eqs. (3.6, 3.5, 2.1) allows the polarization vector to be expressed as:

$$\mathbf{e} = \frac{1}{\sqrt{3}\left|\mathbf{C_h}\right|}\left[\left(2m+n\right)\mathbf{a_1} - \left(2n+m\right)\mathbf{a_2}\right] = \frac{a}{2\left|\mathbf{C_h}\right|}\left[\left(m-n\right)\mathbf{i} + \sqrt{3}\left(m+n\right)\mathbf{j}\right]. \tag{3.55}$$

Therefore, the projection of velocity along a quasi metallic nanotube axis, $\hat{\mathbf{T}}\cdot\left\langle\psi^C\left|\hat{\mathbf{v}}\right|\psi^V\right\rangle$, is:

$$\begin{aligned} i\frac{at}{2\hbar}\frac{a}{\sqrt{f_k^2}\left|\mathbf{C_h}\right|}\Bigg[& \sqrt{3}\sin\left(\frac{a\sqrt{3}}{4\left|\mathbf{C_h}\right|}\left(m-n\right)\left(aq_T\right)\right)\sin\left(\frac{2\pi}{3}+\frac{a\sqrt{3}}{4\left|\mathbf{C_h}\right|}\left(m+n\right)\left(aq_T\right)\right)\left(m+n\right) \\ & +\frac{1}{\sqrt{3}}\cos\left(\frac{a\sqrt{3}}{4\left|\mathbf{C_h}\right|}\left(m-n\right)\left(aq_T\right)\right)\cos\left(\frac{2\pi}{3}+\frac{a\sqrt{3}}{4\left|\mathbf{C_h}\right|}\left(m+n\right)\left(aq_T\right)\right)\left(m-n\right) \\ & -\frac{1}{\sqrt{3}}\cos\left(\frac{4\pi}{3}+\frac{\sqrt{3}a}{2\left|\mathbf{C_h}\right|}\left(m+n\right)\left(aq_T\right)\right)\left(m-n\right)\Bigg]. \end{aligned} \tag{3.56}$$

It is clear from Eq. (3.56) that the projection of electron velocity along the tube is zero if $n = m$, hence by symmetry, all armchair CNTs are optically inactive. While for a zig-zag CNT ($C_h = (n, -n)$) Eq. (3.56) reduces to the simple analytic expression:

$$i\frac{2v_{\mathrm{F}}}{3\sqrt{3}aq_T}\left[1-\cos\left(\frac{\sqrt{3}}{2}aq_T\right)\right]. \tag{3.57}$$

Performing a Taylor series in expansion in q_T, and retaining only first order terms, allows the matrix element for optical transitions between the lowest conduction and the highest valence subbands of a quasi-metallic SWNT to be written as:

$$\hat{\mathbf{T}}\cdot\left\langle\psi^C\left|\hat{\mathbf{v}}\right|\psi^V\right\rangle = iv_{\mathrm{F}}\frac{1}{\sqrt{3}}\left(m+2n\right)\left(2m+n\right)\left(m-n\right)\left(\frac{a}{2\left|\mathbf{C_h}\right|}\right)^3\left(aq_T\right). \tag{3.58}$$

For brevity Eq. (3.58) can be expressed as:

$$i\frac{t_1t_2\left(m-n\right)a^2}{4\left|\mathbf{T}\right|N}v_{\mathrm{F}}q_T. \tag{3.59}$$

For a zig-zag quasi-metallic nanotube the matrix element of optical transition Eq. (3.58) becomes,

$$\hat{\mathbf{T}}\cdot\left\langle\psi^C\left|\hat{\mathbf{v}}\right|\psi^V\right\rangle = -i\frac{v_{\mathrm{F}}}{4}a_{CC}q_T \tag{3.60}$$

These derived transitions rules are in agreement with the general selection rules for SWNTs [120, 39].

Treating q_T as a continuous variable allows the the sum over all q_T in Eq. (3.49) to be replaced by an integral over all q_T states:

$$\sum_{q_T}\Longrightarrow\frac{L}{2\pi}\int dq_T\times 2=\frac{L}{\pi}\int\frac{1}{\frac{d\varepsilon}{dq_T}}d\varepsilon, \tag{3.61}$$

where the additional factor of two accounts for the two valleys. Conservation of energy requires $\xi_C-\xi_V-h\nu=0$ and for direct transitions $\xi_C=-\xi_V$, hence:

$$\xi_C=\frac{h\nu}{2}=\hbar v_{\mathrm{F}}q_T, \tag{3.62}$$

Substituting Eq. (3.58) into Eq. (3.49) and integrating over all states yields:

$$I_\nu = Lf_e\left(\frac{\pi\nu}{v_{\mathrm{F}}}\right)f_h\left(\frac{\pi\nu}{v_{\mathrm{F}}}\right)\frac{\pi^2e^2a_{cc}^2\nu^3}{24\hbar v_{\mathrm{F}}c^3}\frac{\left(m+2n\right)^2\left(2m+n\right)^2\left(n-m\right)^2}{\left(n^2+m^2+nm\right)^3}. \tag{3.63}$$

For a zig-zag quasi-metallic nanotube this becomes

$$I_\nu = Lf_e\left(\frac{\pi\nu}{v_{\mathrm{F}}}\right)f_h\left(\frac{\pi\nu}{v_{\mathrm{F}}}\right)\frac{\pi^2e^2a_{CC}^2\nu^3}{6c^3\hbar v_{\mathrm{F}}}. \tag{3.64}$$

Equation Eq. (3.63) has broader applicability limits than the considered case of $L<l_{ac}$ and

$eV < \hbar\Omega$, in which the distribution functions for electrons and holes are given by Eq. (3.42). In the general case there is a strong dependence of I_ν on the distribution functions, which have to be calculated taking into account all the relevant scattering mechanisms [112, 113, 114, 115, 122, 129].

In the discussed ballistic regime, the spectral density has a universal dependence on the applied voltage and photon frequency for all quasi-metallic SWNTs. In Fig. 3.7 the spectral density for a quasi-metallic zig-zag tube is shown for two values of voltage. It is clearly seen that the maximum of the spectral density of emission has a strong voltage dependence and lies in the terahertz frequency range for experimentally attainable voltages. Spectrally integrating I_ν yields the total photon emission rate. For a single zig-zag SWNT with length $L = 2\ \mu m$ and applied voltage of 0.16 V, this rate is approximately 3000 photons per second. This number can be significantly increased for an array [130] of similarly-biased nanotubes, for which stimulated emission will occur.

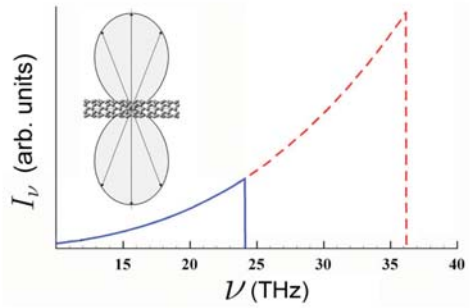

Figure 3.7: The spectral density of spontaneous emission as a function of frequency for two values of applied voltage: solid line for $V = 0.1$ V; dashed line for $V = 0.15$ V. The inset shows the directional radiation pattern of the terahertz emission with respect to the nanotube axis. Figure adapted from Ref. [39].

The directional radiation pattern, shown in the inset of Fig. 3.7, is given by $\cos^2\varphi$, where φ is the angle between the light propagation direction and the nanotube axis. It reflects the fact that the emission of light polarized normally to the nanotube axis is forbidden by the selection rules for optical transitions between the lowest conduction subband and the top valence subband.

For some device applications it might be desirable to emit photons propagating along the nanotube axis, which is possible in optical transitions between the SWNT subbands characterized by angular momenta differing by one [70, 120]. To achieve the emission of these photons by electron heating, it is necessary to have an intersection of such subbands within the energy range accessible to electrons accelerated by attainable voltages. It has been show that this intersection is possible, for example the lowest conduction subbands in several semiconducting zig-zag nanotubes and in all armchair nanotubes [79]. However, for an effective terahertz emission from these nanotubes it is necessary to move the Fermi level very close to the subband intersection point. Therefore, obtaining

terahertz emission propagating along the nanotube axis is a much more difficult technological problem compared to the generation of the emission shown in Fig. 3.7.

3.5.4 Conclusion

In conclusion, it has been demonstrated that a quasi-metallic carbon nanotube can emit terahertz radiation when a potential difference is applied to its ends. The typical required voltages and nanotube parameters are similar to those available in the state-of-the-art transport experiments. The maximum of the spectral density of emission is shown to have a strong voltage dependence, which is universal for all quasi-metallic carbon nanotubes in the ballistic regime. Therefore, the discussed effect can be used for creating a terahertz source whose frequency is controlled by the applied voltage. Appropriately arranged arrays of these nanotubes should be considered as promising candidates for active elements of amplifiers and generators of coherent terahertz radiation. In such an array all biased quasi-metallic SWNTs will emit in a similar fashion, whereas semiconducting and armchair nanotubes will be optically inactive in the terahertz and mid-infrared range; therefore, no special selection of the nanotube type is needed. In addition, the discussed effect provides a spectroscopic tool allowing us to distinguish between quasi-metallic and true metallic (armchair) nanotubes and to verify the validity of the ballistic transport picture for short SWNTs at elevated temperatures and non-vanishing bias voltages.

3.6 Terahertz absorption and emission in quasi-metallic carbon nanotubes

3.6.1 Introduction

In what follows, it shall be shown that the same intrinsic curvature of semi-metallic carbon nanotubes which opens the gap in the nanotube energy spectrum also allows strong optical transitions in the terahertz range. This method is analogous to subjecting an armchair SWNT to a strong magnetic field [81]. Namely, the intrinsic curvature of the nanotube plays the role of a strong magnetic field. Finally, a scheme using the intrinsic curvature of semi-metallic carbon nanotubes to generate terahertz radiation is proposed.

To illustrate that intrinsic curvature allows strong terahertz transitions, we shall study a subclass of these tubes, known as zig-zag quasi-metallic SWNTs, defined by $(3p, 0)$. However, the approach used herein can be generalized to all quasi-metallic tubes, all of which are expected to be optically active, since it is the curvature-induced gap which gives rise to the strong terahertz transitions.

3.6.2 The band structure of narrow-gap single walled nanotubes with curvature

Rolling a graphene sheet to form a carbon nanotube decreases the bond length to the nearest neighbors and rotates the $2p_z$ orbitals, this results in the re-hybridization of the π and σ orbitals. All of the aforementioned effects result in the modification of the hopping parameters of the tight-binding Hamiltonian. In what follows we shall consider the dominant effect, that of bond length contraction. A full calculation taking into account re-hybridization shall be a subject of future study. Let us begin with the electron energy spectrum of graphene:

$$\xi(k) = s\sqrt{\left|\tilde{f}_k\right|^2}, \tag{3.65}$$

where

$$\tilde{f}_k = \sum_{i=1}^{3} t_i \exp(i\mathbf{k}\cdot\mathbf{u}_i) \tag{3.66}$$

and $\mathbf{u}_i$ are the nearest neighbors vectors, which for a graphene sheet are

$$\mathbf{u}_i = \left(\frac{a}{\sqrt{3}}, 0\right), \left(-\frac{a}{2\sqrt{3}}, -\frac{a}{2}\right), \left(-\frac{a}{2\sqrt{3}}, \frac{a}{2}\right). \tag{3.67}$$

t_i are the tight-binding matrix elements associated with the i^{th} nearest neighbor, which for graphene are equivalent i.e., $t_i = t \approx -3$ eV. For convenience, we shall construct our zig-zag SWNTs such that motion is quantized along k_y i.e. $(n, -n)$. The electron energy spectrum for a zig-zag SWNT is obtained from Eq. (3.65) by applying the periodic boundary condition:

$$k_y = 2\pi\frac{l}{n}, \tag{3.68}$$

where l is an integer and for the lowest conduction subband and the highest valence subband is given by Eq. (3.24). Which in the case of a zig-zag SWNT becomes:

$$l = \frac{2}{3}n. \tag{3.69}$$

Hence, the electron energy spectrum for a zig-zag SWNT is given by:

$$\xi(k) = s|t|\sqrt{2 - 2\cos\left(\frac{\sqrt{3}}{2}k_x a\right)}. \tag{3.70}$$

In the terahertz regime Eq. (3.70) becomes:

$$\xi(k) = s\hbar v_{\mathrm{F}} |k_x| \,. \tag{3.71}$$

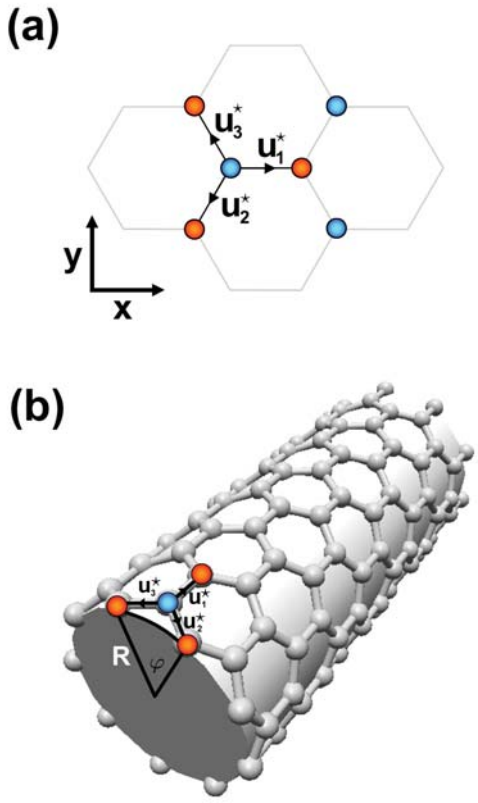

Figure 3.8: (a) The zig-zag quasi-metallic nanotube as an unrolled graphene sheet, represented by the set of effective nearest neighbor vectors $\mathbf{u}_i^\star$, $i = 1, 2, 3$. (b) The zig-zag quasi-metallic nanotube.

Let us now consider the role of curvature. In rolling a graphene sheet to form a carbon nanotube one decreases the length of the nearest neighbor vectors. This is because the new distance is given by the chord between the two sites. One can see from Fig. 3.8 that upon rolling a zig-zag SWNT, $|\mathbf{u}_1|$ remains unchanged whereas the magnitude of $\mathbf{u}_2$ and $\mathbf{u}_3$ are reduced in comparison to that of a planar graphene sheet. The chord length, $|\mathbf{u_2}|$, is given by:

$$|\mathbf{u}_2| = \sqrt{a_y^2 + \left(\frac{a}{2\sqrt{3}}\right)^2}, \tag{3.72}$$

where $a_y = \sqrt{A_1^2 + A_2^2}$. Using simply geometry $A_1$and A_2 are found to be

$$|A_1| = R \sin\left(\frac{a}{2R}\right);$$

$$|A_2| = R\left[1 - \cos\left(\frac{a}{2R}\right)\right],$$

where R is the radius of the nanotube given by $R = an/2\pi$. To understand the effects of including curvature, one can imagine the nanotube as an unrolled graphene sheet, which is described by the same coordinate system as the non-curved case, but differs by a modified set of nearest neighbor vectors, $\mathbf{u}_i^\star$, defined as:

$$\mathbf{u}_i^\star = \left(\frac{a}{\sqrt{3}}, 0\right), \left(-\frac{a}{2\sqrt{3}}, -a_y\right), \left(-\frac{a}{2\sqrt{3}}, a_y\right) \tag{3.73}$$

The effect of curvature is to break the symmetry between the nearest neighbor vectors, thereby breaking the former equivalency of t_1, t_2 and t_3. By symmetry, the hopping parameter t_1 does not change i.e. $t_1 = t$. The probability of hopping between sites is inversely proportional to the distance squared between hoping sites i.e. $t_i \propto \frac{1}{|\mathbf{u_i}|^2}$ [131]. Hence, t_2 and t_3 are modified in the same way. The modified matrix elements of hopping, $t_i^\star$, are related to the original elements, t_i, by the simply relation:

$$\frac{t_i^\star}{t_i} = \left(\frac{|\mathbf{u}_i|}{|\mathbf{u}_i^\star|}\right)^2. \tag{3.74}$$

Hence $\tilde{f}_k$ in the presence of curvature becomes:

$$\tilde{f}_k = t \exp\left(i\frac{k_x a}{\sqrt{3}}\right) + 2t_2^\star \exp\left(-i\frac{k_x a}{2\sqrt{3}}\right) \cos\left(k_y a_y\right) \tag{3.75}$$

and the modified electron energy spectrum for a zig-zag SWNT is now given by:

$$\xi\left(k_x\right) = s\left|t\right| \sqrt{1 + 4\frac{t_2^\star}{t} \cos\left(\frac{\sqrt{3}}{2} k_x a\right) \cos\left(k_y a_y\right) + 4\left(\frac{t_2^\star}{t}\right)^2 \cos^2\left(k_y a_y\right)} \tag{3.76}$$

With the inclusion of curvature the spectrum is no longer linear near the crossing point (see Fig. 3.9), a band gap, ξ_g, has been opened which is given by

$$\xi_g = 2\left|t + 2t_2^\star \cos\left(k_y a_y\right)\right|. \tag{3.77}$$

For a $(30, 0)$ SWNT this gap corresponds to ≈ 5.7 terahertz. In the vicinity of the point $k_x = 0$ the low energy spectrum takes the form

$$\xi\left(k_x\right) = s\sqrt{\left(\frac{\xi_g}{2}\right)^2 - 2\frac{t_2^\star}{t}\cos\left(k_y a_y\right)\left(v_{\mathrm{F}}\hbar k_x\right)^2}, \tag{3.78}$$

which is similar in form to that of a one dimensional, massive, relativistic Dirac fermion, and in the limit that $a_y \to \frac{a}{2}$ (i.e. neglecting the effects of curvature) Eq. (3.78) restores the massless answer $\xi\left(k_x\right) = s\hbar v_{\mathrm{F}}\left|k_x\right|$.

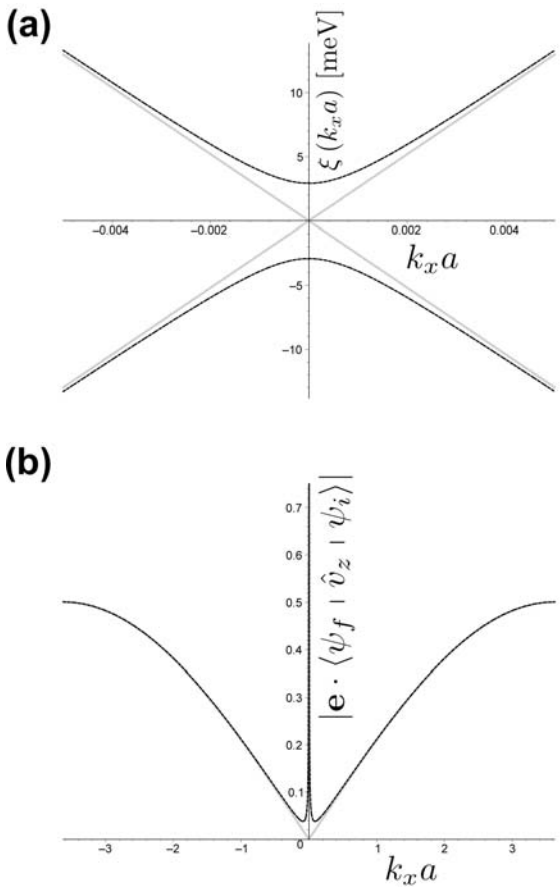

Figure 3.9: (a) Detailed view of the gap, which is opened between the top valence subband and the lowest conduction subband, for a SWNT defined by $(30, 0)$. (b) Dependence of the dipole matrix element for the transition (between the top valence subband and the lowest conduction subband) on the 1D wave vector k_x, with (black dashed line) and without (grey line) curvature, ploted in arbitrary units. The only appreciable change is in the appearance of a high, narrow peak associated with the transition between the top valence subband and the lowest conduction subband, which is not allowed in the absence of curvature.

3.6.3 Optical selection rules

In the dipole approximation, the spectral density, I_ν, is given by

$$I_\nu = \frac{8\pi e^2 \nu}{3c^3}\sum_{i,f} f_e\left(k_i\right) f_h\left(k_f\right)\left|\mathbf{e}\cdot\left\langle\psi_f \mid \hat{v}_z \mid \psi_i\right\rangle\right|^2 \delta\left(\xi_i - \xi_f - h\nu\right), \tag{3.79}$$

where ψ_i and ψ_f are the eigenfunctions of the electrons in the initial and final states, ξ_i and ξ_f are their associated energies, and k_i and k_f are their associated wave vectors and $\mathbf{e}$ is the polarization of the excitation which we take to be propagating along the carbon nanotube axis. In the frame of the tight binding model, the matrix element $\mathbf{e} \cdot \langle \psi_f \mid \hat{v}_z \mid \psi_i \rangle$ can be written as

$$\frac{i}{\hbar}\mathbf{e} \cdot \Re \left[\frac{\tilde{f}_k^\star}{\sqrt{\left|\tilde{f}_k\right|^2}} \sum_{i=1}^{3} e^{i\mathbf{k}\cdot\mathbf{u}_i^\star} t_i^\star \mathbf{u}_i^\star \right] \tag{3.80}$$

(c.f. Eq (2.62)). The matrix element of the electron velocity operator Eq. (3.80) in the absence of curvature between the lowest conduction and the highest valence subbands of the $(3p, 0)$ zig-zag SWNT can be written as (cf. [39])

$$\langle \psi_f \mid v \mid \psi_i \rangle = i\frac{a_{cc}}{8}\omega_{if} \tag{3.81}$$

where $\hbar\omega_{if} = \xi_i - \xi_f$ is the energy difference between the initial (i) and the final (f) states and the result of substituting Eq. (3.81) into Eq. (3.79) and performing the necessary summation was found in section 3.5.3 to be:

$$I_\nu = L f_e\left(\frac{\pi\nu}{v_\mathrm{F}}\right) f_h\left(\frac{\pi\nu}{v_\mathrm{F}}\right) \frac{\pi^2 e^2 a_{cc}^2 \nu^3}{6c^3\hbar v_\mathrm{F}} \tag{3.82}$$

In what follows we shall see how the matrix element Eq. (3.81) and the spectral density Eq. (3.82) are drastically modified when curvature is taken into account. In the presence of curvature the matrix element Eq. (3.80) becomes,

$$i\frac{4\hbar v_F^2}{3\sqrt{3}a} \frac{1}{\sqrt{\left|\tilde{f}_k\right|^2}} \left[1 - 2\left(\frac{t_2^\star}{t}\right)^2 \cos^2\left(k_y a_y\right) + \frac{t_2^\star}{t}\cos\left(\frac{\sqrt{3}k_x a}{2}\right)\cos\left(k_y a_y\right) \right]. \tag{3.83}$$

Which in the terahertz regime becomes:

$$i\frac{4\hbar v_F^2}{3\sqrt{3}a} \frac{1}{\sqrt{\left|\tilde{f}_k\right|}} \left[\frac{3}{4} - 3\left(\frac{t_2^\star}{t}\right)^2 \cos^2\left(k_y a_y\right) + \frac{1}{4}\left(\frac{\xi}{t}\right)^2 \right] \tag{3.84}$$

where ξ is given by Eq. (3.78). For the full derivation of Eq. (3.83) see Appendix B.1. Notably, the matrix element Eq. (3.83) remains finite at $k_x = 0$ in the presence of any asymmetry between $\mathbf{U}_1$ and $\mathbf{U}_2$ and is zero for the case of $\mathbf{U}_1 = \mathbf{U}_2$. Curvature not only opens the gap in the zig-zag SWNT spectrum, but also allows dipole optical transitions at $k_x = 0$ between the highest valence subband and the lowest conduction subband. In this regime the result should hold true across the entire class of quasi-metallic SWNTs, differing only by geometrical factors. In Fig. 3.9 we show

how the matrix elements of the dipole optical transitions polarized along the nanotube axis are modified by taking into account curvature.

The spectral density for a zig-zag SWNT taking into account curvature effects is obtained by substituting Eq. (3.83) into Eq. (3.79), after performing the necessary summation one obtains:

$$I_\nu = L\frac{32}{27}\frac{e^2\nu v_F}{c^3\hbar}\frac{t}{\xi}\frac{\left[\frac{3}{4}-3\left(\frac{t_2^\star}{t}\right)^2\cos^2\left(k_y a_y\right)+\frac{1}{4}\left(\frac{\xi}{t}\right)^2\right]^2}{\sqrt{-2\frac{t_2^\star}{t}\cos\left(k_y a_y\right)\left[\left(\frac{\xi}{t}\right)^2-\left(\frac{\xi_g}{2t}\right)^2\right]}} f_e\left(\frac{\pi\nu}{v_\mathrm{F}}\right) f_h\left(\frac{\pi\nu}{v_\mathrm{F}}\right)\delta\left(\xi_i-\xi_f-h\nu\right), \tag{3.85}$$

where ξ is defined by Eq. (3.76) and $s = 1$. A full derivation of Eq. (3.85) is given in Appendix B.1. The electronic (hole) energy spectrum near the bottom (top) of the gap produced by curvature is non-parabolic as a function of carrier momentum along the nanotube axis. This dispersion results in a van-Hove singularity in the reduced density of states, which in turn leads to a very sharp absorption maximum near the band edge and correspondingly to a very high sensitivity of the photocurrent to photon frequency, see Fig. 3.10.

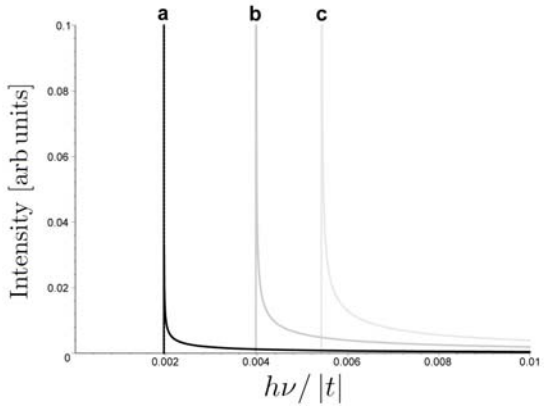

Figure 3.10: The calculated photon absorption spectra for a zig-zag SWNT defined by: (a) $(30, 0)$, (b) $(21, 0)$ and (c) $(18, 0)$, these correspond to intensity peaks at (a) 1.4, (b) 2.9 and (c) 3.9 THz.

3.6.4 Tunable terahertz emitter

The same effect can be used for the generation of a very narrow emission line where the peak frequency is dictated by the radius of the SWNT. The absorption of light polarized normal to the nanotube axis is only possible by optical transitions between SWNT subbands characterized by angular momenta differing by one [70, 120], i.e. for this polarization, transitions between the lowest conduction subband and the top valence subband are forbidden. Therefore a population inversion can be achieved by optical pumping, with the exciting light polarized normally to the

nanotube axis, as shown in Fig. 3.11. Therefore, appropriately arranged arrays of quasi-metallic nanotubes, placed inside a suitable chosen optical resonator, should be considered as promising candidates for active elements of amplifiers and generators of coherent terahertz radiation. An additional benefit of this scheme is that all quasi-metallic SWNTs will emit in a similar fashion, whereas semiconducting and armchair nanotubes will be optically inactive in the terahertz and mid-infrared range; therefore, no special selection of nanotube type is needed. Furthermore, the band gap of quasi-metallic nanotubes can also be controlled by an applied magnetic field [132], therefore allowing such devices to be tunable. Arrays of quasi-metallic SWNTs may also be used as building blocks in terahertz radiation detectors, which would have a high sensitivity in the photocurrent to photon frequency.

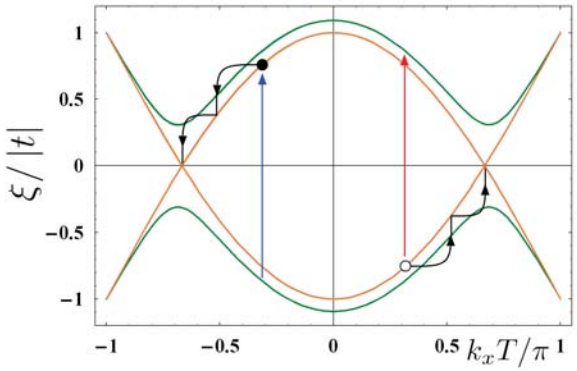

Figure 3.11: A scheme for creating a population inversion between the lowest conduction subband and the top valence subband of an zig-zag SWNT. The right plot shows several energy subbands closest to the Fermi level and illustrates the creation of photoexcited carriers and their non-radiative thermalization. Figure adapted from Ref. [81]

3.6.5 Conclusion

In the absence of curvature, at $k_x = 0$, optical transitions between the top valence subband and the bottom conduction subband in quasi-metallic SWNTs are strictly forbidden by symmetry within the simple zone-folding model of the π-electron graphene spectrum. However, for zig-zag quasi-metallic SWNTs, dipole optical transitions are indeed allowed due to the gap opened in their energy spectrum by intrinsic curvature, which is of the order of terahertz. This result is expected to be true for all quasi-metallic tubes.

3.7 Excitons in narrow-gap carbon nanotubes

3.7.1 Introduction

As was mentioned in the previous sections, the energy spectrum of a carbon nanotube is determined by the way it is rolled and is characterized by two integers (n, m). For most combinations of n and m the energy spectrum of the nanotube is characterized by the gap, whose value is comparable to those in semiconductor materials. However, for a third of n and m combinations, namely when $m-n = 3p,\ p = 0, 1, 2, ...$ the value of the gap is drastically reduced and lies in terahertz frequency range. Moreover, for $m = n$ the gap vanishes in zero magnetic field, and opens only after the application of the magnetic field parallel to the nanotube axis [35, 133, 135].

Optical properties of carbon nanotubes have been investigated by many authors [136, 137, 138, 139, 140]. It was shown that the excitonic effect plays an important role and that the properties of the excitonic resonance can be modulated by applying external fields [83, 141, 142]. However, excitons were theoretically studied mostly for semiconductor carbon nanotubes with sufficiently large gaps [143, 144, 145]. For metallic nanotubes only the excitons associated with high branches of the nanotube spectrum, separated by the energy of about 1 eV, were considered [146, 147, 148]. On the other hand, the analysis of the optical properties of narrow band nanotubes is also of high interest, as there is a growing number of proposals using carbon nanotubes of this type for THz applications, including several schemes put forward by the authors of the present work [39, 80, 81].

In this section we shall consider theoretically the exciton formed by an electron and a hole excited across a narrow gap in a quasi-metallic carbon nanotube, for which the effective mass approximation can not be applied and the effects of the non-parabolicity of the electron and hole dispersion play the major role.

3.7.2 Attractive model potential for excitons

The Hamiltonian for a single free electron in this case can be written as

$$\widehat{H}_0 = \hbar v_{\mathrm{F}}(b\widehat{\sigma}_x\widehat{q} + \widehat{\sigma}_y\Delta) = \hbar v_{\mathrm{F}} \begin{bmatrix} 0 & b\widehat{q} - i\Delta \\ b\widehat{q} + i\Delta & 0 \end{bmatrix}, \tag{3.86}$$

where $\widehat{q}$ is the operator of the wave vector along the nanotube axis and we use the basis $|\psi_A\rangle$, $|\psi_B\rangle$ with indices A, B corresponding to the carbon atoms of two different sublattices in the honeycomb lattice (see Appendix B.2). Here v_{F} is the Fermi velocity in graphene, connected to the tight-binding matrix element of electron hopping $|t| \approx 3$ eV and the graphene lattice constant a by $\hbar v_{\mathrm{F}} = \frac{\sqrt{3}}{2}|t|a$, where $a = |\mathbf{a}_1| = |\mathbf{a}_2| = 2.46$ Å [35]. For the (n, n) armchair nanotube the value

of the band gap $2\hbar v_{\mathrm{F}}|\Delta|$ is determined by the external magnetic field, $\Delta = \frac{2}{a\sqrt{3}} \sin\left(\frac{\pi\Phi}{n\Phi_0}\right)$, where Φ is the magnetic flux through the nanotube cross section, $\Phi_0 = ch/e$ is the flux quantum and $b = \sqrt{\frac{4}{3} - \frac{1}{3}\cos^2\left(\frac{\pi\Phi}{n\Phi_0}\right)}$. For experimentally accessible magnetic fields $\Phi/\Phi_0 \ll 1$, hence herein we shall set $b = 1$. A similar Hamiltonian can be written for a narrow gap carbon nanotube with a gap opened by curvature [116] or for a certain type of graphene nanoribbon [46]. Diagonalization of Eq. (3.86) gives a quasi-relativistic dispersion, $\xi = \pm\hbar v_{\mathrm{F}}\sqrt{\Delta^2 + q^2}$. To go from the case of electrons to the case of holes $|\psi_i^e\rangle \to |\psi_i^h\rangle$, one should use the substitution $\widehat{q} \to -\widehat{q},\ \Delta \to -\Delta$. For the interacting electron-hole pair, the total Hamiltonian can be written in the form of a 4×4 matrix, and the stationary Schrödinger equation for determining the binding energy written in the basis $|\Psi_{ij}\rangle = |\psi_i^e\rangle|\psi_j^h\rangle$ reads

$$\hbar v_{\mathrm{F}} \begin{bmatrix} 0 & \widehat{q}_e - i\Delta & -\widehat{q}_h + i\Delta & 0 \\ \widehat{q}_e + i\Delta & 0 & 0 & -\widehat{q}_h + i\Delta \\ -\widehat{q}_h - i\Delta & 0 & 0 & \widehat{q}_e - i\Delta \\ 0 & -\widehat{q}_h - i\Delta & \widehat{q}_e + i\Delta & 0 \end{bmatrix} \begin{bmatrix} \Psi_{AA} \\ \Psi_{BA} \\ \Psi_{AB} \\ \Psi_{BB} \end{bmatrix} = [\xi - V(x_e - x_h)] \begin{bmatrix} \Psi_{AA} \\ \Psi_{BA} \\ \Psi_{AB} \\ \Psi_{BB} \end{bmatrix}. \tag{3.87}$$

where indices e and h correspond to the electrons and holes, $\widehat{q}_{e,h} = -i\frac{\partial}{\partial x_{e,h}}$. In the absence of interaction this Hamiltonian yields four energy eigenvalues corresponding to a pair of non-interacting quasi-particles: $\xi = \hbar v_{\mathrm{F}}(\pm\sqrt{\Delta^2 + q_e^2} \pm \sqrt{\Delta^2 + q_h^2})$ and the band gap of the two-particle system is given by $\xi_g = 4|\Delta|$. In what follows, we shall consider the case where the Fermi level lies in the middle of the gap (i.e. equilibrium) and all the states above it are empty and all the states below it are fully occupied. In this instance the creation of a quasi-particle (either an electron or a hole) with a negative energy is forbidden by the Pauli principle. Indeed you can not promote a hole into an empty conduction band or create an extra electron in a completely full valence band. Therefore, henceforth only bound states in the energy range 0 to 2Δ shall be considered.

As the potential of electron-hole interaction $V(x_e - x_h)$ depends only on the distance between the electron and hole, it is convenient to move to the center of mass and relative motion coordinates, $X = (x_e + x_h)/2$, $x = x_e - x_h$, $\widehat{q}_e = \widehat{K}/2 + \widehat{k}$, $\widehat{q}_h = \widehat{K}/2 - \widehat{k}$, and represent the exciton wavefunctions as $\Psi_{ij}(X, x) = e^{iKX}\phi_{ij}(x)$, which permits the substitution of the operator $\widehat{K}$ by a number K having the physical meaning of the wave vector of the exciton as a whole. Considering the case of $K = 0$ corresponding to a static exciton, the equation for the wavefunction of relative motion reads

$$\begin{bmatrix} 0 & \widehat{k}-i\Delta & \widehat{k}+i\Delta & 0 \\ \widehat{k}+i\Delta & 0 & 0 & \widehat{k}+i\Delta \\ \widehat{k}-i\Delta & 0 & 0 & \widehat{k}-i\Delta \\ 0 & \widehat{k}-i\Delta & \widehat{k}+i\Delta & 0 \end{bmatrix} \begin{bmatrix} \phi_{AA} \\ \phi_{BA} \\ \phi_{AB} \\ \phi_{BB} \end{bmatrix} = \left[\varepsilon - \tilde{V}(x)\right] \begin{bmatrix} \phi_{AA} \\ \phi_{BA} \\ \phi_{AB} \\ \phi_{BB} \end{bmatrix}, \tag{3.88}$$

where $\varepsilon = \xi/\hbar v_{\mathrm{F}},\ \tilde{V}(x) = V(x)/\hbar v_F,\ \widehat{k} = -i\partial/\partial x$.

Eq. (3.88) represents a system of the first order differential equations, which can be reduced to a single second order equation for ψ_{AA}:

$$\frac{d^2\phi_{AA}}{dx^2} + \frac{1}{\left(\varepsilon - \tilde{V}(x)\right)}\frac{d\tilde{V}(x)}{dx}\frac{d\phi_{AA}}{dx} + \left[\left(\frac{\varepsilon - \tilde{V}(x)}{2}\right)^2 - \Delta^2\right]\phi_{AA} = 0. \tag{3.89}$$

Before solving Eq. (3.89), we need to specify the interaction potential. It needs to possess the following properties: first, due to the finite diameter of the nanotube d it should remain finite at $x \to 0$ for small x and scale as $V(x) \approx -e^2/\sqrt{x^2+d^2}$; second, for large x it should decay exponentially due to the effects of the screening necessarily present in nanotubes of the metallic type [146]. The convenient choice of the potential is

$$\tilde{V}(x) = -\frac{\alpha}{\cosh(\beta x)}, \tag{3.90}$$

where $\alpha = e^2/(\hbar v_{\mathrm{F}} d),\ \beta \sim 1/d$. The additional advantage of the choice of the potential given by Eq. (3.90) is that it admits some analytical results in the context of graphene physics as was shown in Ref. [24].

The results of the numerical solution are shown in Fig. 3.12, Fig. 3.13 and Fig. 3.14. Figures 3.12 and 3.13 show the dependence of the binding energy ε_b calculated as an absolute value of the difference between the eigenenergy of Eq. (3.89) and the energy of the pair of non-interacting electron and hole, $\varepsilon_b = |\varepsilon - 2\Delta|$ measured in the units of β on the effective strength of the interaction α/β for two different values of $\Delta/\beta = 1$ and $\Delta/\beta = 0.01$ corresponding to the cases of semiconductor and narrow-gap quasi-metallic nanotube respectively. For both of these cases, for small values of α/β there is only one bound s-type state, whose binding energy increases with the increase of the interaction strength, until it reaches the value $\varepsilon_b = \varepsilon_g = 4\Delta$ after which it goes to the continuum of states with negative energies and thus unbinds. On the other hand, the increase of α leads to the appearance of the higher order solutions, corresponding to p, d, etc excitons, so that for any value of α there always exists a bound state with energy lying inside the gap.

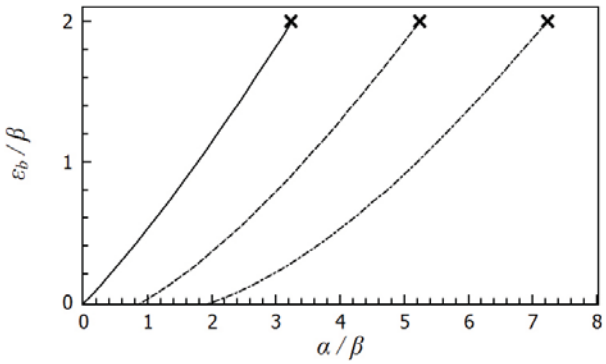

Figure 3.12: The dependence of the exciton binding energy on the interaction strength for a semiconductor nanotube with $\Delta/\beta = 1$. Different lines correspond to different excitonic states. Crosses show the exact analytic result for mid-gap states.

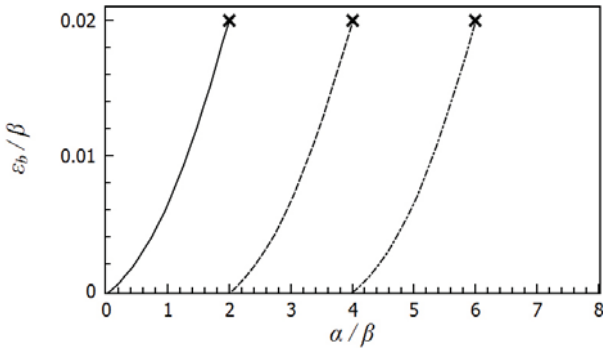

Figure 3.13: The dependence of the exciton binding energy ε_b/β on the interaction strength for a quasi-metallic nanotube with $\Delta/\beta = 0.01$. Different lines correspond to different excitonic states. Crosses show exact the analytic result for mig-gap states.

Note also, that one can find the analytical expression for the values of the parameters when the binding energy is exactly equal to the half of the band gap 2Δ, which can be obtained by reducing Eq. (3.89) to the hypergeometric equation for $\varepsilon = 0$ (see Appendix B.3):

$$\frac{\alpha}{\beta} = 1 + 2n + \sqrt{1 + 4\frac{\Delta^2}{\beta^2}}, \tag{3.91}$$

where $n = 0, 1, 2, ...$ These exact values are shown by crosses in Figs. 3.12 and 3.13.

Fig. 3.14 shows the dependence of the ratio of the binding energy of the 1s exciton to the value of the gap on the interaction strength for the cases of the semiconductor and narrow gap nanotubes. One can see that for small interaction strength the ratio $\varepsilon_b/\varepsilon_g$ is a universal linear function of α/β (for $\alpha/\beta \lesssim 0.6$). It should be noted that for a zero-range attractive potential between the electron and hole this universality holds for all the range of interaction strengths (see Appendix B.4). However, for the smooth interaction potential considered here the universality breaks for sufficiently large interaction strength. The difference between the case of semiconductor and quasi-metallic nanotubes is not, however, as large as one could expect. Namely, the value of

α/β for which the 1s-exciton binding energy is equal exactly to the half of the gap is about 3.2 for the case of a semiconductor nanotube with $\Delta/\beta = 1$ and about 2 for quasi-metallic nanotube with $\Delta/\beta = 0.01$. Also, the calculations of the binding energy in semiconductor nanotubes give values of 20-30 percent of the band gap [143], which according to Fig. 3.14 corresponds to the values of $\alpha/\beta \approx 2$ and ensures that for quasi-metallic nanotubes of similar geometry the 1s excitonic bound state lies within the gap as well.

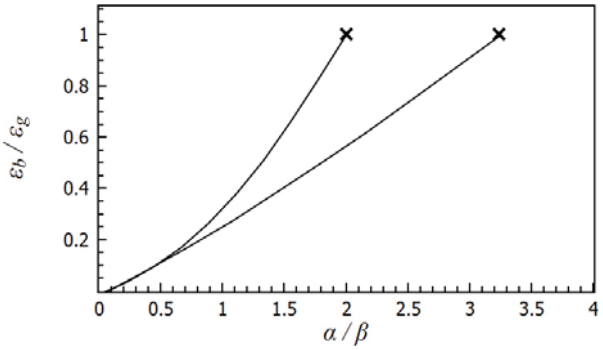

Figure 3.14: The dependence of the ratio of the exciton binding energy to the nanotube band gap on the interaction strength for a quasi-metallic carbon nanotube with $\Delta/\beta = 0.01$ (upper line) and a semiconductor nanotube with $\Delta/\beta = 1$. Only s-states are shown.

Fig. 3.15 shows the square modulus of the excitonic wavefunction in real space for a quasi-metallic nanotube. One sees that for the 1s state the density in the center of mass has a local minimum, which differs strikingly from the result obtained earlier for semiconductor nanotubes in the effective-mass approximation [139], in which the probability density in the exciton center of mass has a maximum. This is related to the complex matrix structure of the Hamiltonian (3.86) resulting in the multi-component structure of the eigenfunctions. A similar dip in the ground-state density was previously reported for graphene-based waveguides [24, 149].

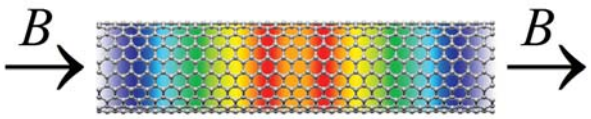

Figure 3.15: Density of the 1s-exciton for a (10,10) carbon nanotube with the magnetic-field induced gap of 10 meV (2.5 THz) corresponding to a magnetic field of 15 T along the nanotube axis. The density represents the probability of finding the electron and hole composing the exciton at the indicated relative separation. Red and blue colors correspond to the highest and lowest values of the density, respectively.

It should be noted that taking into account the valley and spin quantum numbers increases the number of different types of excitons associated with a given carbon nanotube spectrum branch to 16 [145]. Their consideration, however, can be done along the lines described above, the only difference being the modified interaction strength α/β. The lowest in energy exciton in semicon-

ductor nanotubes is known to be optically inactive (dark). The difference between the energy of the dark and bright excitons is proportional to the exciton binding energy and exceeds $k_{\mathrm{B}}T$ at room temperature causing significant suppression of optical emission from semiconductor nanotubes. As is shown above, for narrow-gap nanotubes the binding energy is drastically reduced and there should be no noticeable difference in the population of dark and bright excitonic states at any experimentally attainable temperature. At room temperature, all dark and bright excitons in narrow-gap nanotubes should be fully ionized and the direct inter-band transitions [39, 80, 81] govern the emission in the terahertz range.

3.7.3 Conclusion

In conclusion, we considered the formation of the exciton in narrow gap carbon nanotubes characterized by the quasi-relativistic spectrum of free particles. It was shown that the exciton binding energy scales with the band gap and vanishes as the gap decreases, even for strong electron-hole attraction. Therefore, excitonic effects including strongly-bound dark excitons, which explain poor electroluminescent properties of semiconducting nanotubes, should not dominate for narrow-gap carbon nanotubes. This opens the possibility of using quasi-metallic carbon nanotubes for various terahertz applications.

3.8 Graphene as a terahertz detector

As a gapless semiconductor with ultra-high carrier mobility, graphene is a natural material for detecting terahertz radiation. Graphene p-n junctions structures [19, 20, 21, 22, 150, 151, 152] can be created using two gates placed above and below the graphene layer. In such structures, with high enough top and bottom gate voltages, terahertz absorption is only possible in the junction area. The Fermi level in graphene-based devices can be easily controlled by the gate voltage, which allows a certain degree of tunability in the lower limit of absorbed radiation frequency via the Moss-Burstein effect. In conjunction with an extremely strong angular dependence of the tunneling probability for graphene p-n junctions [14, 18, 25], optical alignment of momenta raises the possibility of using recently fabricated graphene p-n junction structures in polarization-sensitive terahertz detectors, with sub-wave length resolution.

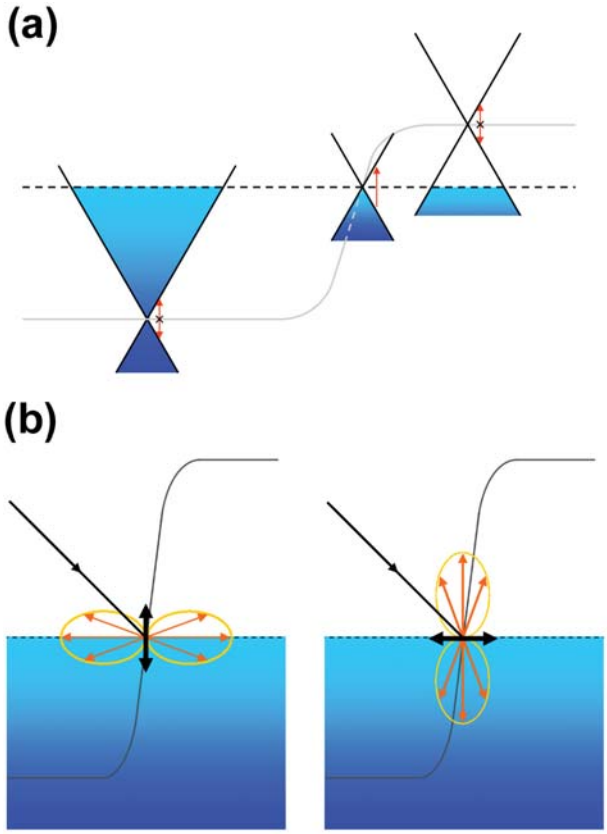

Figure 3.16: A scheme for a proposed polarization-sensitive terahertz detector. The grey line represents the electrostatically defined potential created by a graphene top gate and the dotted line represents the Fermi-level which can be controlled by varying the back gate. (a) shows the allowed region of terahertz absorption. (b) Polar plots of the momentum distribution function of photo-excited carriers of two different polarizations are shown (gold lines). The black arrows represent the polarizations of the excitations. The strong angular dependence of particles traversing the barrier allows the device to be polarization discriminant.

3.9 Conclusion

Within the frame of a simple zone-folding model of the π-electron graphene spectrum, quasi-metallic SWNTs can be considered as one-dimensional analogs of graphene, since in this model the electron low-energy spectrum is linearly dependent on the electron wave vector. Using this model the selection rules for optical transitions caused by light polarized along the nanotube axis was derived. It was demonstrated that quasi-metallic nanotubes can emit terahertz radiation when a potential difference is applied to their ends. The maximum of the spectral density of emission is shown to have a strong voltage dependence, which is universal for all quasi-metallic carbon nanotubes in the ballistic regime. However, due to curvature effects quasi-metallic SWNTs are in fact narrow-gap semiconductors whose band gaps can be of the order of terahertz. For the case of zig-zag quasi-metallic carbon nanotubes, it has been shown that the same intrinsic curvature which opens the gap in the quasi-metallic carbon nanotubes spectrum also allows optical transitions in the terahertz range. This result is expected to be true for all quasi-metallic tubes. In narrow-gap carbon nanotubes, it has been shown that the exciton binding energy scales with the band gap and vanishes as the gap decreases, even for strong electron-hole attraction. Hence, excitonic effects, which explain the poor electroluminescent properties of semiconducting nanotubes, should not dominate for narrow-gap carbon nanotubes. Therefore, arrays of quasi-metallic tubes are promising candidates as active elements of amplifiers and generators of coherent terahertz radiation or as building blocks in terahertz radiation detectors.

Chapter 4

Steering electrons in graphene by electrostatic potentials

4.1 Introduction

Klein proposed that relativistic particles do not experience exponential damping within a barrier like their non-relativistic counterparts, and that as the barrier height tends towards infinity, the transmission coefficient approaches unity [153]. This inherent property of relativistic particles makes confinement non-trivial. Carriers within graphene behave as two-dimensional (2D) massless Dirac fermions, exhibiting relativistic behavior at sub-light speed [12, 13] owing to their linear dispersion, which leads to many optical analogies [25, 154, 155, 156, 157]. Klein tunneling through p-n junction structures in graphene has been studied both theoretically [14, 18, 23, 149, 154, 158, 159, 160, 161, 162], and experimentally [19, 20, 21, 22, 150, 151, 152]. Quasi-bound states were considered in order to study resonant tunneling through various sharply terminated barriers [149, 154, 158, 159, 162]. A change in the geometry of the problem is proposed in order to study the propagation of fully confined modes along a smooth electrostatic potential, much like photons moving along an optical fiber.

So far quasi-one-dimensional channels have been achieved within graphene nanoribbons [13, 163], however the control of their transport properties requires precise tailoring of edge termination [46, 164, 165], currently unachievable. In this chapter it shall be shown that truly bound modes can be created within bulk graphene by top gated structures [19, 20, 21, 22, 151, 152], such as the one shown in Fig. 4.8 (a). In an ideal graphene sheet at half-filling, the Fermi level is at the Dirac point and the density of states for a linear 2D dispersion vanishes. In realistic graphene devices the Fermi level can be set using the back gate. This is key to the realization of truly bound

modes within a graphene waveguide as zero-energy modes cannot escape into the bulk as there are no states to tunnel into. Moreover the electrostatic confinement isolates carriers from the sample edges, which are considered as a major source of inter-valley scattering in clean graphene [166].

In this chapter we obtain an exact analytical solution for bound modes within a smooth electrostatic potential in pristine graphene at half-filling, count the number of modes and calculate the conductance of the channel. The conductance carried by each of these modes is comparable to the minimal conductivity of a realistic disordered graphene system [12, 167, 168, 169]. For the considered model potential we show that there is a threshold potential characteristic strength (the product of the potential strength with its width), for which bound modes appear. Whereas a symmetric quantum well always contains a bound mode for non-relativistic particles, we show that it is not the case for charge carriers in graphene.

4.2 Background theory

4.2.1 Klein tunneling

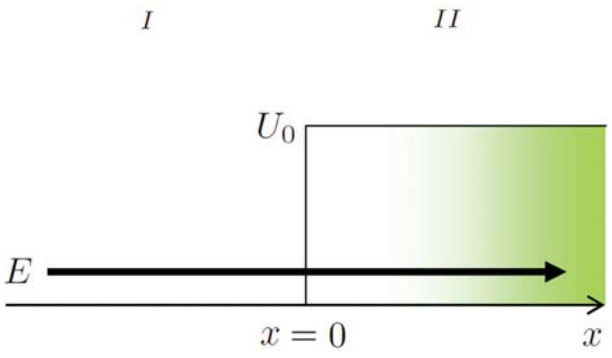

Figure 4.1: Klein tunneling of a particle, characterized with incident energy, E, tunneling through an electrostatically defined potential, $U(x)$. The y-axis represents energy.

Consider a two-dimensional massless Dirac fermion impinging upon an electrostatic potential, $U(x)$ of the form (Fig. 4.1)

$$U(x) = \begin{cases} U_0, & \text{for } x > 0, \\ 0, & \text{for } x < 0, \end{cases} \tag{4.1}$$

whose energy, E, is less than that of the barrier. The particles Hamiltonian is given by,

$$\hbar v_{\mathrm{F}} \left(\sigma_x \hat{\mathbf{q}}_x + \sigma_y \hat{\mathbf{q}}_y\right) \psi = \left[E - U(x)\right] \psi \tag{4.2}$$

where $\hat{\mathbf{q}}_x = -i\frac{\partial}{\partial x}$ and $\hat{\mathbf{q}}_y = -i\frac{\partial}{\partial y}$, σ_x and σ_y are the Pauli spin matrices:

$$\sigma_x = \begin{bmatrix} 0 & 1 \\ 1 & 0 \end{bmatrix}; \quad \sigma_y = \begin{bmatrix} 0 & -i \\ i & 0 \end{bmatrix}. \tag{4.3}$$

When Eq. (4.2) is applied to a two-component Dirac wavefunction of the form:

$$\mathrm{e}^{iq_y y} \begin{bmatrix} C_1(x) \\ C_2(x) \end{bmatrix}, \tag{4.4}$$

where $C_1(x)$ and $C_2(x)$ are the wavefunctions associated with the A and B sub-lattices of graphene respectively and the free motion in the y-direction is characterized by the wave vector q_y measured with respect to the Dirac point, the following coupled first-order differential equations are obtained:

$$\frac{1}{[\varepsilon - V(x)]}\left(-i\frac{\partial C_2}{\partial x} + -iq_y C_2\right) = C_1; \tag{4.5}$$

$$\frac{1}{[\varepsilon - V(x)]}\left(-i\frac{\partial C_1}{\partial x} + iq_y C_1\right) = C_2, \tag{4.6}$$

where $\varepsilon = E/\hbar v_{\mathrm{F}}$ and $V = U/\hbar v_{\mathrm{F}}$. Eliminating C_2 reduces the system of Eqs. (4.5-4.6) to a single second order differential equation for C_1, which for the potential given by Eq. (4.1) becomes:

$$\frac{\partial^2 C_1}{\partial x^2} + \left\{[V(x) - \varepsilon]^2 - q_y^2\right\} C_1 = 0, \tag{4.7}$$

which has the solution

$$C_1 = A_{\pm} e^{i\kappa x}. \tag{4.8}$$

where $\kappa = \pm\sqrt{[V(x) - \varepsilon]^2 - q_y^2}$. C_2 is obtained by substituting Eq. (4.8) into Eq. (4.6):

$$C_2 = \frac{1}{[\varepsilon - V(x)]}(\kappa + iq_y) C_1. \tag{4.9}$$

The wavefunction in region I is given by

$$\psi_I = A_1 \begin{bmatrix} 1 \\ \frac{|\kappa_I| + iq_y}{\varepsilon} \end{bmatrix} e^{i|\kappa_I|x} + A_2 \begin{bmatrix} 1 \\ \frac{-|\kappa_I| + iq_y}{\varepsilon} \end{bmatrix} e^{-i|\kappa_I|x}, \tag{4.10}$$

where $\kappa_I = \pm\sqrt{\varepsilon^2 - q_y^2}$. Whereas the wavefunction in region II is given by

$$\psi_{II} = A_3 \begin{bmatrix} 1 \\ \frac{|\kappa_{II}|+iq_y}{(\varepsilon-V_0)} \end{bmatrix} e^{i|\kappa_{II}|x} + A_4 \begin{bmatrix} 1 \\ \frac{-|\kappa_{II}|+iq_y}{(\varepsilon-V_0)} \end{bmatrix} e^{-i|\kappa_{II}|x}, \tag{4.11}$$

where $\kappa_{II} = \pm\sqrt{(V_0 - \varepsilon)^2 - q_y^2}$.

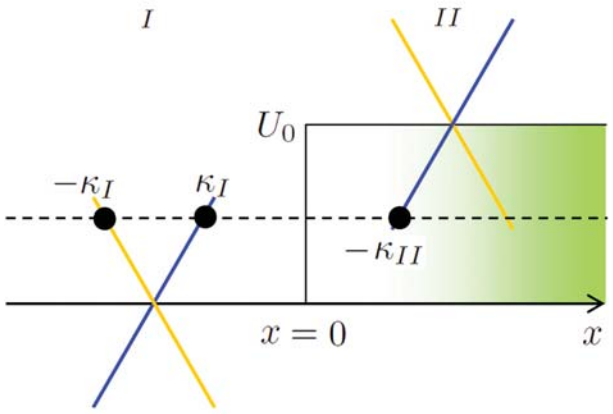

Figure 4.2: A depiction of the spatial dependence of the dispersion relation, the y-axis represents energy.

For a particle to propagate from the left hand side to right hand side of the barrier, its x-component of group velocity must be positive. Therefore, inside the barrier we must take the $\kappa_{II} < 0$ solution and discard the $\kappa_{II} > 0$ solution (see Fig. 4.1). This results in the following choice of wavefunctions for region I (ψ_I) and II (ψ_{II})

$$\psi_I = \begin{bmatrix} 1 \\ \frac{|\kappa_I|+iq_y}{\varepsilon} \end{bmatrix} e^{i|\kappa_I|x} + r \begin{bmatrix} 1 \\ \frac{-|\kappa_I|+iq_y}{\varepsilon} \end{bmatrix} e^{-i|\kappa_I|x}; \tag{4.12}$$

$$\psi_{II} = t \begin{bmatrix} 1 \\ \frac{-|\kappa_{II}|+iq_y}{(\varepsilon-V_0)} \end{bmatrix} e^{-i|\kappa_{II}|x}, \tag{4.13}$$

where r and t are the probabilities amplitudes of reflection and transmission respectively. Note, the incident flux of particles from the left has been normalized to unity. The continuity of the wave function at the boundary requires:

$$1 + r = t; \tag{4.14}$$

$$\frac{(|\kappa_I| + iq_y)}{\varepsilon} + r\frac{(-|\kappa_I| + iq_y)}{\varepsilon} = t\frac{(-|\kappa_{II}| + iq_y)}{(\varepsilon - V_0)}. \tag{4.15}$$

Eliminating t reduces the system of Eqs.(4.14-4.15) to a single expression:

$$r = \frac{|\kappa_I|\,(\varepsilon - V_0) + \varepsilon\,|\kappa_{II}| - iq_yV_0}{|\kappa_I|\,(\varepsilon - V_0) - \varepsilon\,|\kappa_{II}| + iq_yV_0}. \tag{4.16}$$

For a particle of normal incidence i.e., $q_y = 0$, $r = 0$. Therefore, these massless particles exhibit no reflection upon striking the potential barrier V_x. During the tunneling process, the particle changes from electron-like behavior outside the barrier to hole-like behavior inside the barrier. This electron-hole conjugation allows the particles to continue moving in the same direction with no reflection. It is this property which gives rise to many of graphene's highly desirable electronic and thermal properties. However, this same effect also presents a problem for device realization, namely the seemingly impossible task of true confinement and thus a total lack of device switchability.

4.2.2 "Sharp but smooth" potentials

The above analysis is true for 2D Dirac fermions. However, directly applying this atomically abrupt electrostatically defined potential to graphene's charge carriers engenders certain problems. One must be cautious, since one has made an implicit assumption that the potential is in fact smooth (here smooth refers to a potential which varies on a scale far larger than that of the graphene crystal lattice primitive unit cell) despite being atomically abrupt. Features which are on the same scale as the lattice constant give rise to large changes in charge carrier momenta, which allows particles to be scattered into another valley. This process is known as intervalley scattering and is commonly neglected in "sharp but smooth" potentials.

Indeed atomic detail is important, for example in graphene nanoribbons, the precise nature of the edge structure dictates the strips properties. This is a result of the unique boundary conditions each edge type has [33, 46, 170, 171]. This is highlighted by the two highest symmetry edges; the zig-zag and armchair edge. The former is able to support edge surface states and resonances whereas as later can not. Hence, by considering truly smooth potentials one can avoid the statement "sharp but smooth" potentials, which is commonly used to neglect inter valley mixing for the tunneling problem [14, 18, 149, 158, 159].

4.2.3 Introduction to graphene p-n junctions

Traditionally, top gate structures are formed by the deposition of a layer of insulating dielectric on top of which is laid a metal structure, shaped to requirement by electron-beam lithography (the procedure is described in Refs. [19, 20, 151, 152]). The application of a voltage between the top gate and the sample below changes the potential profile locally within the sample, creating a p-n-p or n-p-n junction. In traditional semiconductor samples the conducting layer, a 2D electron gas, is found deep in the sample within a quantum well formed by the growth of a semiconducting

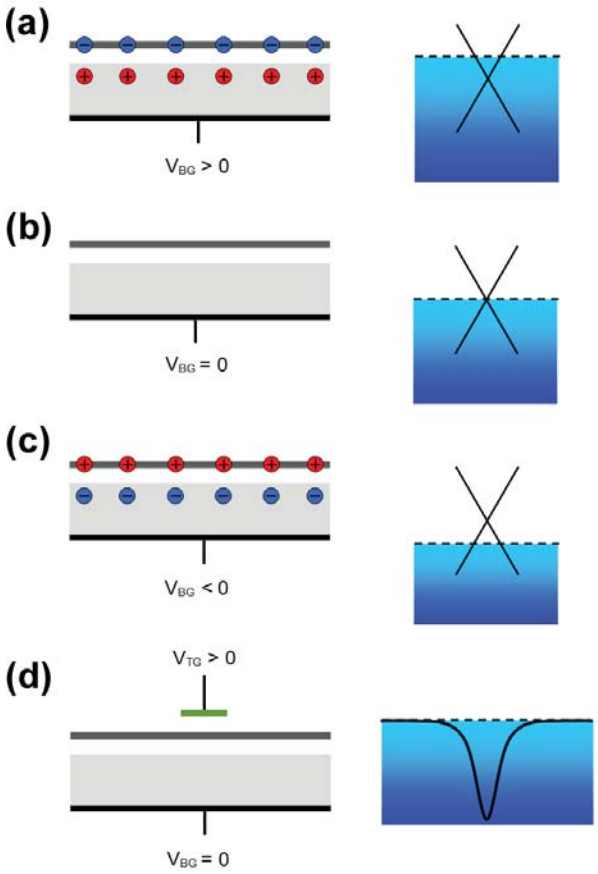

Figure 4.3: A schematic diagram representing a variety of graphene-gated structures. The effect of modulating the top (V_{TG}) and back gate voltages (V_{BG}) on the charge carrier concentration in both graphene (dark grey) and the silicon substrate (light grey) is shown. The blue (red) circles represent electrons (holes) and the resulting change in the Fermi level (dashed line) is shown on the right hand side. In the instance of: (a) a positive back gate voltage, the electrons are drawn from the earth into the graphene sheet, thereby rasing the Fermi level; (b) no applied gate voltage, the Fermi level remains at the Dirac point; (c) a negative back gate voltage, the electrons are driven from the graphene sheet, thereby lowering the Fermi level. The last figure (d) represents a typical top-gated structure with zero applied back gate voltage. The electrostatic potential generated by the top gate is shown by the thick black line.

material, like gallium arsenide, sandwiched between two layers of a wider band gap material, e.g. aluminum arsenide. In this case the top gate can be deposited directly on top of the larger band gap material.

In graphene, one has direct physical contact with the 2D conducting layer and in a similar fashion to conventional systems its carrier density can be manipulated via external gates as shown in Fig. 4.3. Ballistic field effect devices such as p-n and p-n-p junctions have been fabricated [19, 20, 21, 22, 150, 151, 152] however, their behavior is markedly different to that of conventional hetero-structures. Namely, graphene's charge carries behave as two-dimensional massless Dirac fermions and therefore exhibit an absence of backscattering from smooth electrostatically defined potentials [16].

It is well known that graphene is prone to doping from the substrate and materials with which it has contact [172]. In this case, one must ask what effect an insulating dielectric layer deposited on the surface of the graphene will have. In fact, it is known that a dielectric layer decreases the mobility of carriers below it, which makes achieving the ballistic transport regime difficult [19]. Whilst top gate structures deposited upon dielectric layers have been used in graphene [19, 20, 151, 152] there has been active research in achieving "air-bridge" top gates [21, 22]: top gates that have an air gap below them to remove the effect of the dielectric layer.

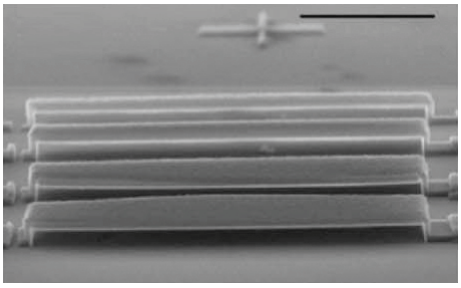

Figure 4.4: A series of top gates of varying sizes separated from the substrate with an air gap. The scale bar is 2μm. From Liu *et al.* in Ref. [22]

"Air-bridge" top gate structures are produced using lift-off resist; the top gate is deposited upon a layer that can be removed using solvents [21, 22]. The top gate is now suspended above the graphene sheet, separated by an air gap (see Fig. 4.4) and removes the problem with the reduction in mobility due to the dielectric layer. There are, however, other problems associated with "air-bridge" structures, including sagging of the top gate; with a large suspension distance, the top gate begins to sag under its own weight [21, 22], see Fig. 4.5.Furthermore, due to this, "air

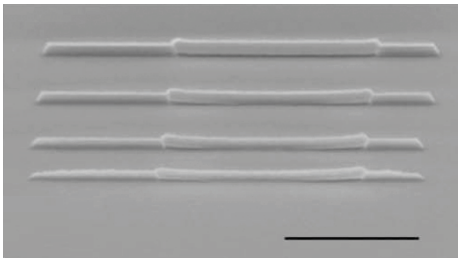

Figure 4.5: Top gate structures are shown to sag with decreasing width. The scale bar is 2μm. From Liu *et al.* in Ref. [22]

bridge" top gates have to be wider than conventional top gates to increase their rigidity [21, 22].

4.3 Fully confined modes in graphene

4.3.1 Optical analogies

However, in light of the proceeding analogy it is not surprising that confinement is impossible using the current geometry employed in top gated devices to study resonant tunneling. Owing to graphene's linear dispersion one can liken graphene's charge carriers to that of photons. Such an analogy has led to many proposed effects such as the Goos-Hänchen effect [155, 156] and using the Veslago's lens for electron beam focusing [25]. Fiber optic cables are used to guide and confine photons, light entering normal to the fiber easily passes through as shown in Fig. 4.6 (a), whereas light propagating along the fiber can be confined as shown in Fig 4.6 (b), providing the waveguide is constructed from materials of appropriate refractive indices. The electrostatic equivalent of such structures is the p-n-p junction. Here the quantum well acts as the higher index material and traps the electrons and of course, a smooth well is required to avoid inter-valley scattering. The described geometry is therefore akin to a waveguide formed by a smoothly graduated refractive index.

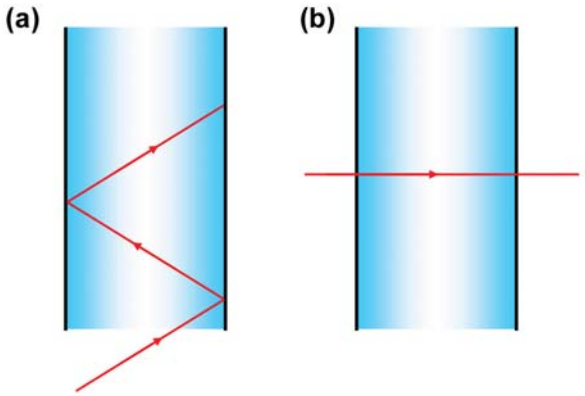

Figure 4.6: Light propagating: (a) along a fiber optic cable, (b) through a fiber optic cable.

4.3.2 Observation of modes

In the low energy regime, graphene's dispersion is given by

$$E = \pm v_{\mathrm{F}} \hbar \left| \mathbf{q} \right|, \tag{4.17}$$

where $\mathbf{q}$ is the particles momentum relative to the Dirac point. From Eq. (4.17) the density of states per unit volume, D, is found to be

$$D\left(E\right) = \frac{2E}{\pi} \left(\frac{1}{\hbar v_F} \right)^2. \tag{4.18}$$

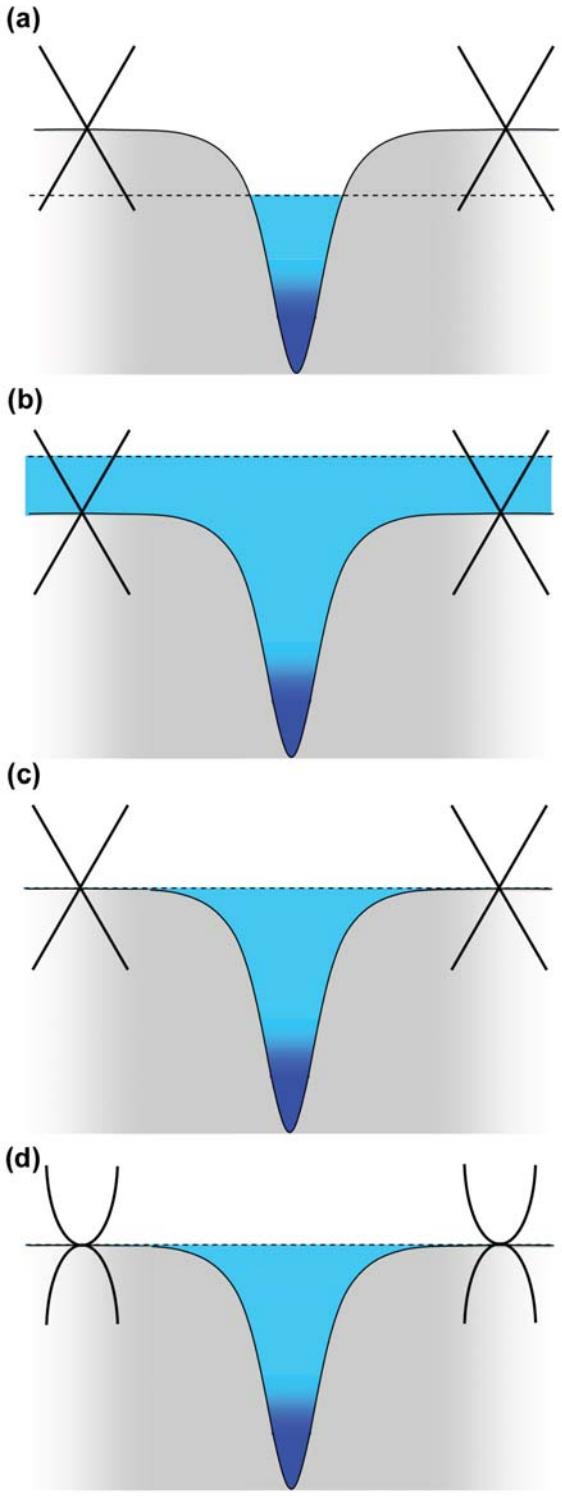

Figure 4.7: A depiction of graphene's dispersion relation (thick black line) outside the influence of an electrostatic potential (represented by the thin black line) created by a top gate. The dotted line shows the Fermi level position at: (a) $\epsilon_F < 0$, (b) $\epsilon_F > 0$ and (c) $\epsilon_F = 0$. (d) represents a waveguide in bi-layer graphene.

The density of states is linear in energy, hence as $E \to 0$ the density of states vanishes, whereas for a conventional two-dimensional system, the of density of states per unit volume, given by

$$D(E) = \frac{m}{\pi\hbar^2} \tag{4.19}$$

remains finite.

Let us now consider a one-dimensional symmetric potential, which is both smooth and vanishing as $x \to \infty$. For a conventional system, inside the well there exists discrete energy levels, whereas outside the well the particles are free, their spectra continuous. The transverse degree of freedom (i.e. motion along the well) allows the coupling of states inside and outside of the well. Hence any mode contained within such a waveguide has a finite lifetime and are referred to as "leaky modes". For both conventional and graphene systems when the Fermi energy, ϵ_F, is non-zero, the conductivity will be dominated by the 2D Fermi sea of electrons throughout the sample, as can be seen in Fig. 4.7, thus making the observation of confined modes difficult.

Let us now consider the case of $E = 0$. For conventional systems the density of states outside the well is finite, therefore the bound states inside the well can leak into the continuum states outside of the well. In contrast to conventional systems, graphene's density of states is zero at $E = 0$; there are no accessible states outside the well at $E = 0$, therefore fully confined modes in graphene can exist. For an ideal sample, at low temperatures, the conductivity of the channel would be the only contribution to sample conductance. In contrast to this, bi-layer graphene's dispersion is parabolic and therefore any modes propagating along the waveguide would be leaky and their contribution to sample conductivity would be swamped by the sea of Fermi electrons outside the well c.f. Fig. 4.7 (d).

4.4 Fully confined modes in a model potential

The Hamiltonian of graphene for a two-component Dirac wavefunction in the presence of a one-dimensional potential $U(x)$ is

$$\hat{H} = v_F\left(\sigma_x\hat{p}_x + \sigma_y\hat{p}_y\right) + U(x) \tag{4.20}$$

where $\sigma_{x,y}$ are the Pauli spin matrices, $\hat{p}_x = -i\hbar\frac{\partial}{\partial x}$ and $\hat{p}_y = -i\hbar\frac{\partial}{\partial y}$ are the momentum operators in the x and y directions respectively and $v_F \approx 1 \times 10^6$m/s is the Fermi velocity in graphene. In what follows we will consider smooth confining potentials, which do not mix the two inequivalent valleys. All the results herein can be easily reproduced for the other valley. When Eq. (4.20) is

applied to a two-component Dirac wavefunction of the form:

$$\begin{bmatrix} \Psi_A(x) \\ \Psi_B(x) \end{bmatrix} e^{iq_y y} \tag{4.21}$$

where $\Psi_A(x)$ and $\Psi_B(x)$ are the wavefunctions associated with the A and B sub-lattices of graphene respectively and the free motion in the y-direction is characterized by the wave vector q_y measured with respect to the Dirac point, the following coupled first-order differential equations are obtained:

$$\left[V(x) - \epsilon\right] \Psi_A(x) - i\left(\frac{\partial}{\partial x} + q_y\right) \Psi_B(x) = 0 \tag{4.22}$$

$$-i\left(\frac{\partial}{\partial x} - q_y\right) \Psi_A(x) + \left[V(x) - \epsilon\right] \Psi_B(x) = 0 \tag{4.23}$$

Here $V(x) = U(x)/\hbar v_F$ and energy ϵ is measured in units of $\hbar v_F$. For the treatment of confined modes within a symmetric electron waveguide, $V(x) = V(-x)$, it is convenient to consider symmetric and anti-symmetric modes. One can see from Eqs.(4.5-4.6) that $\Psi_A(x)$ and $\Psi_B(x)$ are neither even or odd, so we transform to symmetrized functions:

$$\Psi_1 = \Psi_A(x) - i\Psi_B(x), \quad \Psi_2 = \Psi_A(x) + i\Psi_B(x) \tag{4.24}$$

The wavefunctions Ψ_1 and Ψ_2 satisfy the following system of coupled first-order differential equations:

$$\left[V(x) - (\epsilon - q_y)\right] \Psi_1 - \frac{\partial \Psi_2}{\partial x} = 0 \tag{4.25}$$

$$\frac{\partial \Psi_1}{\partial x} + \left[V(x) - (\epsilon + q_y)\right] \Psi_2 = 0 \tag{4.26}$$

It is clear from Eqs.(4.25-4.26) that Ψ_1 and Ψ_2 have opposite parity.

Notably, upon exchanging x for y and p_x for p_y, the system of equations Eqs.(4.25-4.26) can be written in the compact form:

$$\left(v_F \sigma_y \hat{p}_y + m_{eff} v_{\mathrm{F}}^2 \sigma_z\right) \psi = \left[E - U(y)\right] \psi, \tag{4.27}$$

where

$$\psi = \begin{bmatrix} \Psi_1(y) \\ \Psi_2(y) \end{bmatrix} e^{iq_x x}, \tag{4.28}$$

σ_z is the Pauli spin matrix and $m_{eff} = |p_x| / v_{\mathrm{F}}$. Eq. (4.27) is none other than the 1D Dirac equation

with mass, and for a particle with mass, confinement is the natural expectation. Furthermore, it can be seen from Eq. (4.27) that a particle impinging normal to the barrier will become massless, and according to the Klein paradox will be transmitted with a probability of unity.

For an ideal graphene sheet at half-filling the conductivity is expected to vanish due to the vanishing density of states. When the Fermi energy is at the Dirac point ($\epsilon = 0$) there are no charge carriers within the system, so graphene is a perfect insulator. However all available experiments demonstrate non-vanishing minimal conductivity [12, 13, 167] of the order of e^2/h which is thought to be due to disorder within the system [13, 168, 169, 173] or finite-size effects [174, 175].

In order to study confined states within and conductance along an electron waveguide it is necessary to use the back gate to fix the Fermi energy (ϵ_F) at zero, as shown in Fig. 4.8 (b). Note that Fig. 4.8 (a) is just a schematic of the proposed experimental geometry and that side contacts may be needed to maintain the "bulk" Fermi level at zero energy. The conductivity of the graphene sheet is a minimum and for a square sample the conductance is of the order of the conductance carried by a single mode within a waveguide. Thus the appearance of confined modes within the electron waveguide will drastically change the conductance of a graphene flake. Indeed each mode will contribute $4e^2/h$, taking into account valley and spin degeneracy. For device applications the sample should be designed in such a way that the contribution to the conductance from the confined modes is most prominent. In the ideal case, the conductivity of the channel would be the only contribution to that of the graphene sheet. When $\epsilon_F \neq 0$, the conductivity will be dominated by the 2D Fermi sea of electrons throughout the graphene sheet. Henceforth, we shall consider the modes for $\epsilon = 0$.

We shall consider truly smooth potentials, allowing us to avoid the statement of "sharp but smooth" potentials, which is commonly used to neglect inter-valley mixing for the tunneling problem [14, 18, 149, 158, 159]. Furthermore, we are interested in potentials that vanish at infinity and have at least two fitting parameters, characterizing their width and strength, in order to fit experimental potential profiles [19, 20, 21, 22, 151, 152]. Let us consider the following class of potentials, which satisfy the aforementioned requirements:

$$V(x) = -\frac{\alpha}{\cosh^{\lambda}(\beta x)} \tag{4.29}$$

where α, β and λ are positive parameters. The negative sign in Eq. (4.29) reflects a potential well for electrons, and similar results can easily be obtained for holes by changing the sign of $V(x)$. Notably $\lambda = 2$ is the familiar case of the Pöschl-Teller potential, which has an analytic solution for the non-relativistic case [176].

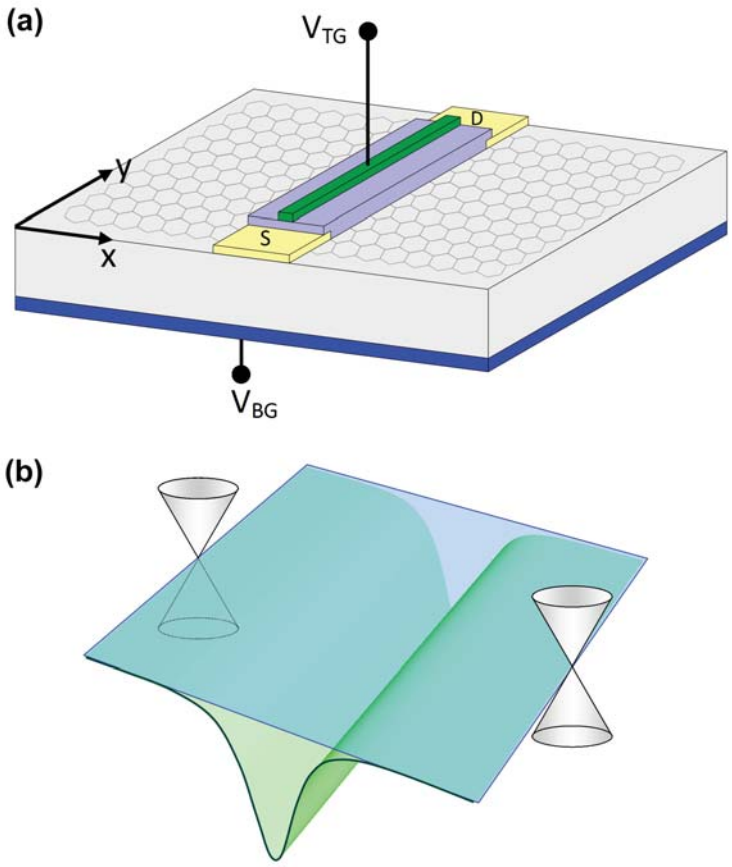

Figure 4.8: (a) A schematic diagram of a Gedankenexperiment for the observation of localized modes in graphene waveguides, created by the top gate (V_{TG}). The Fermi level is set using the back gate (V_{BG}) to be at the Dirac point ($\epsilon_F = 0$). (b) The electrostatic potential created by the applied top gate voltage. The plane shows the Fermi level position at $\epsilon_F = 0$.

4.4.1 Accuracy of the model potential

To illustrate the relevance of the chosen model potential to realistic top-gate structures a simple calculation of the potential distribution in the graphene plane for a simplified top-gate structure is presented. Fig. 4.9 shows the model used in the estimate. We shall consider a wire of radius r_0, separated by distance h from a metallic substrate (i.e. doped Si). We are interested in the potential profile in the graphene plane elevated by distance d from the same substrate. As we are interested in the case when the Fermi level in graphene is at zero energy (the Dirac point), we assume the absence of free carriers in graphene. We also assume the absence of any dielectric layers, but the problem can be generalized in such an instance.

The potential generated by the wire ϕ_1 and the potential due to the image charge within the doped Si ϕ_2 are

$$\phi_1 = -\frac{\Gamma}{2\pi\epsilon} \ln\left(\frac{r}{h}\right) \tag{4.30}$$

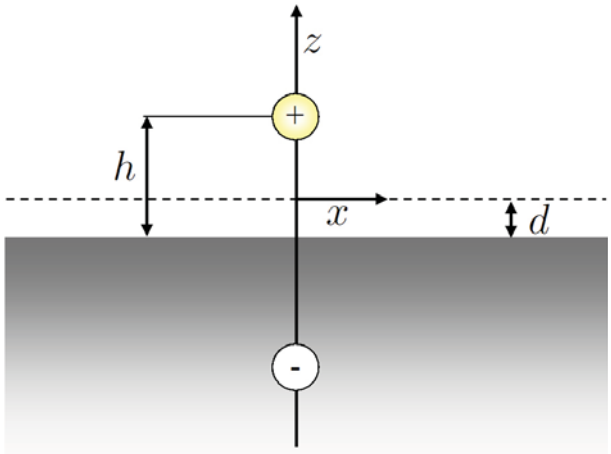

Figure 4.9: The simplified geometry used to obtain the model potential. The image charge is shown for convenience.

and

$$\phi_2 = \frac{\Gamma}{2\pi\epsilon} \ln\left(\frac{l}{h}\right) \tag{4.31}$$

respectively, where r and l are the distances from the wire and image charge respectively, and ϵ is the permittivity of air. The total potential along the z-axis is found (using $l = 2h - z$ and $r = z$) to be:

$$\phi = \frac{\Gamma}{2\pi\epsilon}\left[\ln\left(\frac{2h-z}{h}\right) - \ln\left(\frac{z}{h}\right)\right] = \frac{\Gamma}{2\pi\epsilon}\ln\left(\frac{2h-z}{z}\right), \tag{4.32}$$

thus the applied potential at the wire (e.g. $z = r_0$) is

$$\phi_{appl} = \frac{\Gamma}{2\pi\epsilon}\ln\left(\frac{2h-r_0}{r_0}\right), \tag{4.33}$$

where

$$\Gamma = 2\pi\epsilon\left[\frac{\phi_{appl}}{\ln\left(\frac{2h-r_0}{r_0}\right)}\right]. \tag{4.34}$$

The potential in the graphene sheet can be found using the fact that $r^2 = x^2 + (h-d)^2$ and $l^2 = x^2 + (h+d)^2$ and is easily shown to be:

$$U(x) = \frac{e\widetilde{\phi_0}}{2}\ln\left[\frac{x^2+(h-d)^2}{x^2+(h+d)^2}\right], \tag{4.35}$$

where $\widetilde{\phi_0} = \phi_0 / \ln\left[(2h-r_0)/r_0\right]$ and ϕ_0 is the voltage applied between the top electrode and metallic substrate. One can see that this potential behaves as:

$$\begin{aligned} U(x) &\approx -U_0 + e\widetilde{\phi_0}\tfrac{2hd}{(h^2-d^2)^2}x^2; \qquad && x \ll (h-d), \\ U(x) &\approx e\widetilde{\phi_0}\tfrac{2hd}{x^2}; && x \gg (h+d). \end{aligned} \tag{4.36}$$

The depth of the potential well is given by

$$U_0 = e\phi_0 \left[\frac{\ln\left(\frac{h+d}{h-d}\right)}{\ln\left(\frac{2h-r_0}{r_0}\right)} \right], \tag{4.37}$$

and the half-width at half-maximum (HWHM) is given by $x_0 = \sqrt{h^2 - d^2}$. In Fig. 4.10 we show a comparison between the potential given by Eq. (4.35) and the potential $-U_0/\cosh(\beta x)$ with the same HWHM and potential strength. Clearly the potential given by $-U_0/\cosh(\beta x)$ provides a significantly better approximation than that of the square well potential.

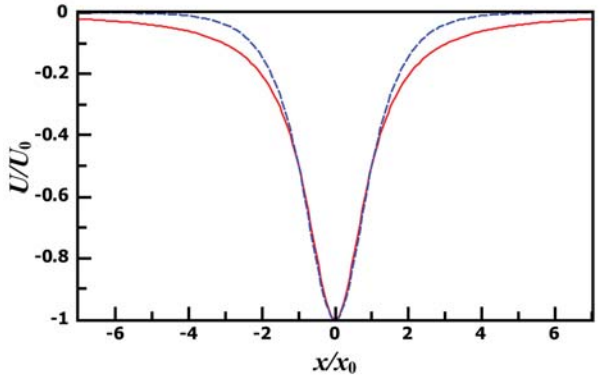

Figure 4.10: A comparison between the potential created by a wire suspended above the graphene plane (solid line) and the $-U_0/\cosh(\beta x)$ potential with the same half width at half maximum (dashed line).

4.4.2 Solution of the 2D Dirac equation for $-U_0/\cosh(\beta x)$

Eliminating Ψ_2 (Ψ_1) reduces the system of Eqs. (4.25-4.26) to a single second-order differential equation for Ψ_1 (Ψ_2), which for the potential given by Eq. (4.29) and $\epsilon = 0$ becomes

$$\frac{\partial^2 \Psi_{1,2}}{\partial z^2} + \lambda \tanh(z) \frac{\omega \cosh^{-\lambda}(z)}{\omega \cosh^{-\lambda}(z) \pm \Delta} \frac{\partial \Psi_{1,2}}{\partial z} + \left(\omega^2 \cosh^{-2\lambda}(z) - \Delta^2\right) \Psi_{1,2} = 0, \tag{4.38}$$

where the dimensionless variables $z = \beta x$, $\Delta = q_y/\beta$ and $\omega = \alpha/\beta$ are used. For $\lambda = 1$, the change of variable $\xi = \tanh(z)$ allows Eq. (4.38) to be reduced to a set of hypergeometric equations yielding the following non-normalized bound solutions for $\Delta > 0$:

$$\begin{aligned} \Psi_{1,2} = &\pm (1+\xi)^p (1-\xi)^q \; {}_2\mathrm{F}_1\left(p+q-\omega,\, p+q+\omega;\, 2p+\frac{1}{2};\, \frac{1+\xi}{2}\right) \\ &+(-1)^n (1+\xi)^q (1-\xi)^p \; {}_2\mathrm{F}_1\left(p+q-\omega,\, p+q+\omega;\, 2p+\frac{1}{2};\, \frac{1-\xi}{2}\right), \end{aligned} \tag{4.39}$$

where in order to terminate the hypergeometric series it is necessary to satisfy $p = \frac{1}{2}(\omega - n) + \frac{1}{4}$, $q = \frac{1}{2}(\omega - n) - \frac{1}{4}$ and $\Delta = \omega - n - \frac{1}{2}$, where n is a positive integer. Though it has been assumed that ω is positive, one can see that the structure of the solutions in Eq. (4.39) remains unchanged with the change of sign of ω, reflecting electron-hole symmetry. In order to avoid a singularity at $\xi = \pm 1$ we require that both $p > 0$ and $q > 0$ and obtain the condition that $\omega - n > \frac{1}{2}$. It should be noted that this puts an upper limit on n, the order of termination of the hypergeometric series. Notably the first mode occurs at $n = 0$, thus there is a lower threshold of $\omega > \frac{1}{2}$ for which bound modes appear. Hence within graphene, quantum wells are very different to the non-relativistic case; bound states are not present for any symmetric potential, they are only present for significantly strong or wide potentials, such that $\omega = \alpha/\beta > \frac{1}{2}$.

Let us consider the first mode ($n = 0$) in Eq. (4.39) which appears within the electronic waveguide with increasing ω. In this case the hypergeometric function is unity, and the normalized wavefunctions are:

$$\Psi_{1,2} = A_1 \left[(1+\xi)^{\frac{\omega}{2}-\frac{1}{4}} (1-\xi)^{\frac{\omega}{2}+\frac{1}{4}} \pm (1+\xi)^{\frac{\omega}{2}+\frac{1}{4}} (1-\xi)^{\frac{\omega}{2}-\frac{1}{4}} \right] \tag{4.40}$$

where $A_{1,2}$ is given by:

$$A_{1,2} = \left\{ \frac{\beta\ (2\omega - 1)\, \Gamma(\omega)\, \Gamma\left(\omega + \frac{1}{2}\right)}{4\sqrt{\pi} \left[2\Gamma^2\left(\omega + \frac{1}{2}\right) \pm (2\omega - 1)\, \Gamma^2(\omega) \right]} \right\}^{\frac{1}{2}} \tag{4.41}$$

where $\Gamma(z)$ is the Gamma function. As expected, the two functions given by Eq. (4.40) are of different parity, thus unlike the non-relativistic case there is an odd function corresponding to the first confined mode. This leads to a threshold in the characteristic potential strength ω at which the first confined mode appears; much like in the conventional quantum well, where the first odd state appears only for a sufficiently deep or wide potential well. Fig. 4.11 shows Ψ_1, Ψ_2 and the corresponding electron density profiles for the first and second bound modes for the case of $\omega = 2$. The shape of the confinement potential is shown for guidance within the same figure. The charge density profile for these modes differs drastically from the non-relativistic case. The first mode ($n = 0$) has a dip in the middle of the potential well, whereas the second mode ($n = 1$) has a maximum. This is a consequence of the complex two-component structure of the wavefunctions.

For negative values of Δ , Ψ_1 and Ψ_2 switch parity such that $\Psi_{1,2}(-\Delta) = \Psi_{2,1}(\Delta)$. This means backscattering within a channel requires a change of parity of the wavefunctions in the x-direction. Notably, when another inequivalent Dirac valley is considered, one finds that there are modes of the same parity propagating in the opposite direction. However inter-valley scattering requires a very short-range potential or proximity to the sample edges. Thus for smooth scattering potentials

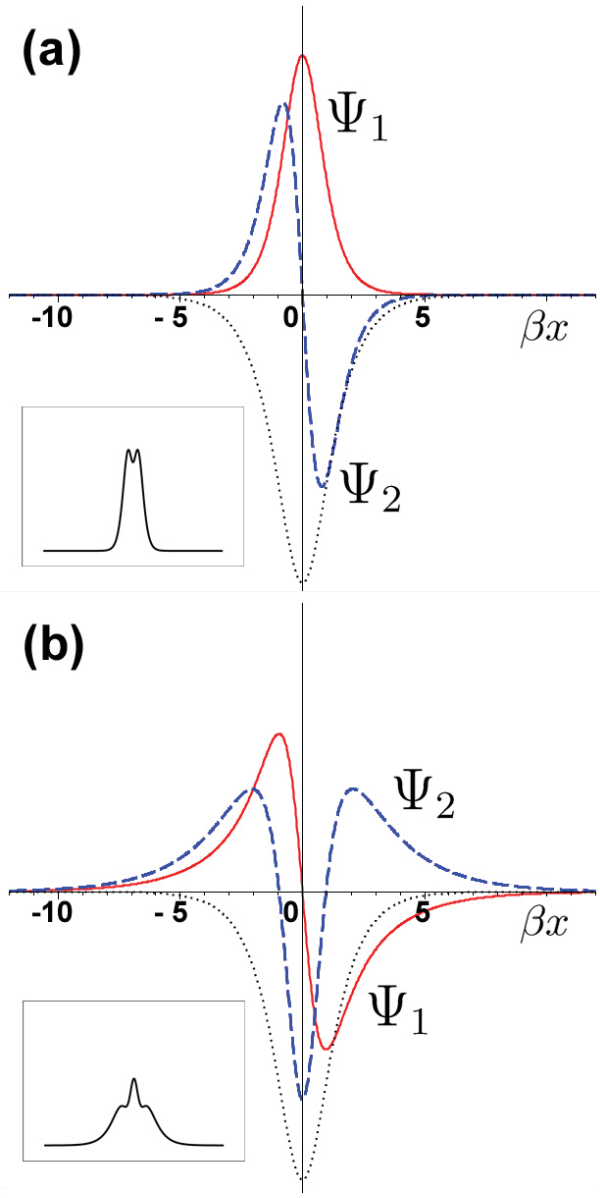

Figure 4.11: The wavefunctions Ψ_1 (solid line) and Ψ_2 (dashed line) are shown for $\omega = 2$ for (a) the first ($n = 0$) mode and (b) the second ($n = 1$) mode. A potential profile is provided as a guide for the eye (dotted line). The insets show the electron density profile for the corresponding modes.

backscattering should be strongly suppressed. Such suppression should result in an increase in the mean free path of the channel compared to that of graphene. This is similar to the suppression of backscattering in carbon nanotubes [16], where the ballistic regime is believed to persist up to room temperature with a mean free path exceeding one micrometer [39, 71]. In some sense the considered waveguide can be thought of as a carbon nanotube-like structure with parameters controlled by the top gate.

Notably, the results obtained are also applicable for the case of a one-dimensional massive particle which is confined in the same potential. This can be achieved by the substitution $|q_y| \to mv_F/\hbar$ into Eqs.(4.25-4.26), where the gap is given by $2mv_F^2$. Hence in the massless 2D case the momentum along the waveguide plays the same role as the gap in the massive one-dimensional case. Therefore, in a massive one-dimensional Dirac system (such as a narrow gap carbon nanotube) there exists a bound state in the middle of the gap for certain values of the characteristic strength of the potential. This problem is considered in more detail in Ref. [177].

The number of modes N_ω at a fixed value of ω is the integer part of $\omega + \frac{1}{2}$ herein denoted $N_\omega = \left\lfloor \omega + \frac{1}{2} \right\rfloor$. The conductance of an ideal one-dimensional channel characterized by ω is found using the Landauer formula to be $G_\omega = 4N_\omega e^2/h$. By modulating the parameters of the potential, one can increase the conductance of the channel from zero in jumps of $4e^2/h$. The appearance of the first and further confined modes within the conducting channel modifies both the strength and the profile of the potential. This nonlinear screening effect [23, 160] is neglected in the above expression for G_ω and shall be a subject of future investigation.

4.4.3 Discussion and conclusions

All the results obtained in this section have been for a specific potential. However, general conclusions can be drawn from these results for any symmetric potential. Namely, the product of the potential strength and its width dictates the number of confined modes within the channel [178]. Moreover, this product has a threshold value for which the first mode appears. The width of the potential is defined by the geometry of the top gate structure, and the strength of the potential is defined by the voltage applied to the top gate. The mean free path of electrons within graphene is of the order of 100 nm and sub-100 nm width gates have been reported in the literature [19, 20, 21, 22, 151, 152], making quantum effects relevant. The number of modes within such top-gated structures is governed by the strength of the potential, with new modes appearing with increasing potential strength. In a top gate structure modeled by our potential with a width at half maximum of 50nm, the first bound mode should appear for a potential strength of approximately 17 meV and further modes should appear with increasing potential strength in steps of 34 meV,

which corresponds to 395 K. Therefore a noticeable change in conductivity should be observed in realistic structures even at room temperature. This is similar to the quantum Hall effect which is observed in graphene at room temperature [179]. Thus by changing the geometry from normal transmission to propagation along a potential, we establish the ability of graphene to be used as a switching device.

In summary, it has been shown that contrary to widespread belief, truly confined (non-leaky) modes are possible in graphene in a smooth electrostatic potential vanishing at infinity. Full confinement is possible for zero-energy modes due to the vanishing density of states at the charge neutrality point. Exact analytical solutions for fully confined zero-energy modes in the potential $V(x) = -\alpha/\cosh(\beta x)$ have been obtained. Such a potential provides a reasonable fit to experimental potential profiles in existing top gate structures [19, 20, 21, 22, 151, 152]. Within such a potential there is a threshold value of $\omega = \alpha/\beta$ for which bound modes first appear, which is contrary to conventional non-relativistic systems. A simple relation between the number of confined modes and the characteristic potential strength ω has been found. The threshold potential strength enables on/off behavior within the graphene waveguide, and suggests future device applications. The existence of bound modes within smooth potentials in graphene may provide an additional argument in favor of the mechanism for minimal conductivity, where charge puddles lead to a percolation network of conducting channels [173].

There are experimental challenges which need to be resolved in order to observe confined modes in graphene waveguides. These include creating narrow gates and thin dielectric layers as well as optimizing the geometry of the sample. Our work also poses further theoretical problems, including the study of non-linear screening, many-body effects, parity changing backscattering and inter-valley scattering within the channel.

The study of quasi-one-dimensional channels within conventional semiconductor systems has led to many interesting effects. Many problems are still outstanding, including the 0.7 anomaly in the ballistic conductance which is a subject of extensive experimental and theoretical study [180]. It is envisaged that the ability to produce quasi-one-dimensional channels within graphene, containing quasi-relativistic carriers, will reveal new, interesting and non-trivial physics.

Chapter 5

Conclusion

A linearly polarized excitation is shown to create a strongly anisotropic distribution of photoexcited carriers in graphene, where the momenta of photoexcited carriers are aligned preferentially normal to the polarization plane, allowing one to effectively steer the electrons in graphene by light. The alignment is due to the pseudo-spin. Namely, the ratio of the two components of the spinor-like graphene wavefunction depends on momentum which influences the optical transition selection rules. The alignment phenomena offers an experimental tool to generate highly directional photoexcited carriers which could assist in the investigation of "direction-dependent phenomena" in graphene-based nanostructures.

The effect of momentum alignment in graphene also provides a contact-free method of characterizing energy and momentum relaxation. It was shown that in the weak pumping regime, the HPL is completely de-polarized after relaxing via the interaction with long-wavelength optical phonons intrinsic to graphene, whereas the relaxation of hot electrons via the coupling to bulk optical phonons in silicon carbide does not. Studying the depolarization of HPL in a magnetic field, allows one to obtain the momentum relaxation times of hot electrons.

In the presence of trigonal warping one must take into account contributions from both Dirac points to fully describe graphene's optical transition selection rules. This warping has also been shown to be a means to spatially separate carriers belonging to different valleys, therefore opening the door to an optical means of controlling valley polarization (optovalleytronics) and quantum computing in graphene.

Within the frame of a simple zone-folding model of the π-electron graphene spectrum, it was demonstrated that quasi-metallic carbon nanotubes can emit terahertz radiation when a potential difference is applied to their ends. The maximum of the spectral density of emission is shown to have a strong voltage dependence, which is universal for all quasi-metallic carbon nanotubes in the

ballistic regime.

For the case of zig-zag quasi-metallic carbon nanotubes, it was shown that the same intrinsic curvature which opens the gap in the spectrum also allows optical transitions in the terahertz range. This result is expected to be true for all quasi-metallic tubes. In such narrow-gap carbon nanotubes, it has been shown that the exciton binding energy scales with the band gap and vanishes as the gap decreases, even for strong electron-hole attraction. Hence, excitonic effects, which explain the poor electroluminescent properties of semiconducting nanotubes, should not dominate for narrow-gap carbon nanotubes. Therefore, arrays of quasi-metallic tubes are promising candidates as active elements of amplifiers and generators of coherent terahertz radiation or as building blocks in terahertz radiation detectors.

Not only can the electrons in graphene be steered by light, but they can also be confined and steered by electrostatic potentials. It has been shown that contrary to widespread belief, truly confined modes are possible in graphene in a smooth electrostatic potential vanishing at infinity. Full confinement is possible for zero-energy modes due to the vanishing density of states at the charge neutrality point. Exact analytical solutions for fully confined zero-energy modes in the potential $V(x) = -\alpha/\cosh(\beta x)$ have been obtained. Such a potential provides a reasonable fit to experimental potential profiles in existing top gate structures . Within such a potential there is a threshold value of $\omega = \alpha/\beta$ for which bound modes first appear, which is contrary to conventional non-relativistic systems. A simple relation between the number of confined modes and the characteristic potential strength ω has been found. The threshold potential strength enables on/off behavior within the graphene waveguide and could serve as a basis for future device applications.

Appendix A

Appendices to chapter 1

A.1 Graphene's dispersion in polar coordinates

Graphene's electron energy spectrum can be described by the expression:

$$\xi_s = s\,|t|\sqrt{3 + 4\cos\left(\frac{\sqrt{3}}{2}ak_x\right)\cos\left(\frac{1}{2}ak_y\right) + 2\cos\left(k_y a\right)}. \tag{A.1}$$

Since we are interested in optical transitions which occur in the vicinity of the Dirac point, it is natural to re-express Eq. (A.1) in terms of $\mathbf{q}$, defined as the momentum measured relative to the $\mathbf{K}_+$ or $\mathbf{K}_-$ point. i.e. $\mathbf{k} = \mathbf{q} + \mathbf{K}_\pm$, thus Eq. (A.1) can be expressed by

$$\xi_s = s\,|t|\left[3 - 2\cos\left(q_y a \pm \frac{\pi}{3}\right) \mp \sqrt{3}\sin\left(\frac{1}{2}aq_y + \frac{\sqrt{3}}{2}aq_x\right) \mp \sqrt{3}\sin\left(\frac{1}{2}q_y a - \frac{\sqrt{3}}{2}aq_x\right)\right.$$
$$\left. - \cos\left(\frac{1}{2}q_y a - \frac{\sqrt{3}}{2}aq_x\right) - \cos\left(\frac{1}{2}q_y a + \frac{\sqrt{3}}{2}aq_x\right)\right]^{\frac{1}{2}}. \tag{A.2}$$

Upon moving to polar coordinates Eq. (A.2) becomes

$$\xi_s = s\,|t|\left\{3 - 2\cos\left[aq\sin\left(\varphi_{\mathbf{q}}\right) \pm \frac{\pi}{3}\right] \mp \sqrt{3}\sin\left[aq\sin\left(\varphi_{\mathbf{q}} - \frac{\pi}{3}\right)\right] - \cos\left[aq\sin\left(\varphi_{\mathbf{q}} - \frac{\pi}{3}\right)\right]\right.$$
$$\left. \mp\sqrt{3}\sin\left[aq\sin\left(\varphi_{\mathbf{q}} + \frac{\pi}{3}\right)\right] - \cos\left[aq\sin\left(\varphi_{\mathbf{q}} + \frac{\pi}{3}\right)\right]\right\}^{\frac{1}{2}},$$

where $q = \sqrt{q_x^2 + q_y^2}$ and $\varphi_{\mathbf{q}} = \arctan\left(q_y/q_x\right)$. Further simplification results in

$$\xi_s = s\,|t|\sqrt{3 - 2\cos\left[\frac{\pi}{3} \mp aq\sin\left(\varphi_{\mathbf{q}} - \frac{\pi}{3}\right)\right] - 2\cos\left[\frac{\pi}{3} \mp aq\sin\left(\varphi_{\mathbf{q}} + \frac{\pi}{3}\right)\right] - 2\cos\left[\frac{\pi}{3} \pm aq\sin\left(\varphi_{\mathbf{q}}\right)\right]}.$$

A.2 Matrix element of optical transitions

In section 2.3.3 the matrix element of velocity between the valence and conduction bands was found to be

$$i\frac{t}{\hbar}\left[\left(C_1^C\right)^\star\left(C_2^V\right)\sum_{i=1}^{3}e^{i\mathbf{k}\cdot\mathbf{u}_i}\mathbf{u}_i-\left(C_2^C\right)^\star\left(C_1^V\right)\sum_{i=1}^{3}e^{-i\mathbf{k}\cdot\mathbf{u}_i}\mathbf{u}_i\right]. \tag{A.3}$$

Using the identity $-\left(C_2^C\right)^\star\left(C_1^V\right)=\left\{\left(C_1^C\right)^\star\left(C_2^V\right)\right\}^\star$ Eq. (A.3) can be reduced to

$$i2\frac{t}{\hbar}\Re\left[\left(C_1^C\right)^\star\left(C_2^V\right)\sum_{i=1}^{3}e^{i\mathbf{k}\cdot\mathbf{u}_i}\mathbf{u}_i\right]. \tag{A.4}$$

Eqs.(2.21, A.4) yield;

$$i\frac{at}{\hbar\sqrt{|f_k|^2}}\Re\left\{\frac{1}{\sqrt{3}}\left[1-2\cos^2\left(\frac{1}{2}ak_y\right)+2e^{i\frac{\sqrt{3}}{2}ak_x}\cos\left(\frac{1}{2}ak_y\right)-e^{-i\frac{\sqrt{3}}{2}ak_x}\cos\left(\frac{1}{2}ak_y\right)\right]\mathbf{i}\right.$$

$$\left.+i\sin\left(k_y\frac{a}{2}\right)\left[e^{-i\frac{\sqrt{3}}{2}ak_x}+\cos\left(\frac{1}{2}ak_y\right)\right]\mathbf{j}\right\}.$$

Retaining the real part only, the matrix element becomes

$$i\frac{at}{\hbar\sqrt{|f_k|^2}}\left\{\frac{1}{\sqrt{3}}\left[\cos\left(\frac{\sqrt{3}}{2}ak_x\right)\cos\left(\frac{1}{2}ak_y\right)-\cos\left(ak_y\right)\right]\mathbf{i}+\sin\left(\frac{\sqrt{3}}{2}ak_x\right)\sin\left(\frac{1}{2}ak_y\right)\mathbf{j}\right\}.$$

The projection of the electron velocity along the direction of the polarization vector, $\mathbf{e}$, is given by $\mathbf{e}\cdot\left\langle\psi^C\left|\hat{\mathbf{v}}\right|\psi^V\right\rangle$:

$$i\frac{at}{\hbar\sqrt{|f_k|^2}}\left\{\frac{1}{\sqrt{3}}\left[\cos\left(\frac{\sqrt{3}}{2}ak_x\right)\cos\left(\frac{1}{2}ak_y\right)-\cos\left(ak_y\right)\right]e_x+\sin\left(\frac{\sqrt{3}}{2}ak_x\right)\sin\left(\frac{1}{2}ak_y\right)e_y\right\}. \tag{A.5}$$

Since we are interested in optical transitions which occur in the vicinity of the Dirac point, it is natural to re-express Eq. (A.5) in terms of $\mathbf{q}$, defined as the momentum measured relative to the $\mathbf{K}_+$ or $\mathbf{K}_-$ point. i.e. $\mathbf{k}=\mathbf{q}+\mathbf{K}_\pm$, thus Eq. (A.5) can be expressed as

$$i\frac{at}{2\hbar\sqrt{|f_k|^2}}\left\{\frac{1}{\sqrt{3}}\left[-\cos\left(\frac{\pi}{3}\pm\left[\frac{\sqrt{3}}{2}aq_x-\frac{1}{2}aq_y\right]\right)-\cos\left(\frac{\pi}{3}\mp\left[\frac{\sqrt{3}}{2}aq_x+\frac{1}{2}aq_y\right]\right)+2\cos\left(aq_y\pm\frac{\pi}{3}\right)\right]e_x\right.$$

$$+\left[\cos\left(\frac{\pi}{3}\mp\left[\frac{\sqrt{3}}{2}aq_x+\frac{1}{2}aq_y\right]\right)-\cos\left(\frac{\pi}{3}\pm\left[\frac{\sqrt{3}}{2}aq_x-\frac{1}{2}aq_y\right]\right)\right]e_y\Bigg\}. \tag{A.6}$$

Upon moving to polar coordinates Eq. (A.6) becomes

$$i\frac{at}{2\hbar\sqrt{|f_k|^2}}\left[\left\{\cos\left[\frac{\pi}{3}\mp aq\sin\left(\frac{\pi}{3}+\varphi_{\mathbf{q}}\right)\right]-\cos\left[\frac{\pi}{3}\pm aq\sin\left(\frac{\pi}{3}-\varphi_{\mathbf{q}}\right)\right]\right\}\sin\left(\varphi_{\mathbf{e}}\right)\right.$$

$$\left.+\frac{1}{\sqrt{3}}\left\{-\cos\left[\frac{\pi}{3}\pm aq\sin\left(\frac{\pi}{3}-\varphi_{\mathbf{q}}\right)\right]-\cos\left[\frac{\pi}{3}\mp aq\sin\left(\frac{\pi}{3}+\varphi_{\mathbf{q}}\right)\right]+2\cos\left[aq\sin\left(\varphi_{\mathbf{q}}\right)\pm\frac{\pi}{3}\right]\right\}\cos\left(\varphi_{\mathbf{e}}\right)\right], \tag{A.7}$$

where $q=\sqrt{q_x^2+q_y^2}$, $\varphi_{\mathbf{q}}=\arctan\left(q_y/q_x\right)$ and $\varphi_{\mathbf{e}}=\arctan\left(e_y/e_x\right)$. Further manipulation yields

$$\mathbf{e}\cdot\left\langle\psi^C\left|\hat{\mathbf{v}}\right|\psi^V\right\rangle=-iv_{\mathrm{F}}\frac{2}{3\sqrt{|f_k|^2}}\left\{\cos\left(\varphi_{\mathbf{e}}\right)\cos\left[qa\sin\left(\varphi_{\mathbf{q}}\right)\pm\frac{\pi}{3}\right]\right.$$

$$\left.-\cos\left(\frac{\pi}{3}+\varphi_{\mathbf{e}}\right)\cos\left[\frac{\pi}{3}\mp aq\sin\left(\frac{\pi}{3}+\varphi_{\mathbf{q}}\right)\right]-\cos\left(\frac{\pi}{3}-\varphi_{\mathbf{e}}\right)\cos\left[\frac{\pi}{3}\pm aq\sin\left(\frac{\pi}{3}-\varphi_{\mathbf{q}}\right)\right]\right\}. \tag{A.8}$$

A.3 Derivation of α_1/α_0 due to intrinsic optical phonons

The intraband transition rate of an electron from a state with wave vector $\mathbf{q}$ at energy E_0 to state $\mathbf{q}'$ at energy $E_1=E_0-E_{ph}$ is:

$$w_\mu\left(\mathbf{q},\mathbf{q}'\right)\propto\left[1-s_\mu\cos\left(\varphi_{\mathbf{q}}+\varphi_{\mathbf{q}'}-2\varphi_{\mathbf{p}}\right)\right]\delta_{\mathbf{q},\mathbf{q}'+\mathbf{p}}, \tag{A.9}$$

where $\mathbf{p}$ is the phonon wave-vector, $\mu=l$ and t denote the transverse and longitudinal modes respectively, and $s_l=1$ while $s_t=-1$. Introducing the variables $\theta=\varphi_{\mathbf{q}}-\varphi_{\mathbf{q}'}$ and $\Theta=\varphi_{\mathbf{q}'}-\varphi_{\mathbf{p}}$ allows Eq. (A.9) to be written as

$$w_\mu\left(\mathbf{q},\mathbf{q}'\right)\propto\left[1-s_\mu\cos\left(\theta+2\Theta\right)\right]\delta_{\mathbf{q},\mathbf{q}'+\mathbf{p}}. \tag{A.10}$$

Our goal is to express Eq. (A.10) as purely a function of θ.

Momentum conservation requires that $\mathbf{p}\cdot\mathbf{p}=\left(\mathbf{q}-\mathbf{q}'\right)\cdot\left(\mathbf{q}-\mathbf{q}'\right)$, which results in the expression

$$p^2=q^2+q'^2-2qq'\cos\left(\theta\right). \tag{A.11}$$

Similarly $\mathbf{q}\cdot\mathbf{q}=\left(\mathbf{q}'+\mathbf{p}\right)\cdot\left(\mathbf{q}'+\mathbf{p}\right)$ yields

$$q^2=q'^2+p^2+2q'p\cos\left(\Theta\right). \tag{A.12}$$

From Eq. (A.11) and Eq. (A.12) we obtain:

$$\cos(2\Theta) = \frac{2\left[q' - q\cos(\theta)\right]^2}{\left[q^2 + q'^2 - 2qq'\cos(\theta)\right]} - 1 \tag{A.13}$$

Momentum conservation also requires that $\mathbf{p} \times \mathbf{q}' = \mathbf{q} \times \mathbf{q}'$, which leads to the usefully identity

$$\sin(\Theta) = -\frac{q}{p}\sin(\theta). \tag{A.14}$$

Therefore the sine of the double angle Θ is given by

$$\sin(2\Theta) = -2\frac{q}{p}\sin(\theta)\cos(\Theta). \tag{A.15}$$

Using Eq. (A.11) and Eq. (A.12) this can be re-expressed as

$$\sin(2\Theta) = \sin(\theta)\frac{2q'q - 2q^2\cos(\theta)}{\left[q^2 + q'^2 - 2qq'\cos(\theta)\right]} \tag{A.16}$$

Eqs. (A.9, A.13, A.16) yield;

$$w_\mu(\mathbf{q}, \mathbf{q}') \propto 1 - s_\mu\left[\frac{\left(q^2 + q'^2\right)\cos(\theta) - 2q'q}{q^2 + q'^2 - 2qq'\cos(\theta)}\right]. \tag{A.17}$$

Introducing the variable $r = \frac{2qq'}{q^2+q'^2}$ Eq. (A.17) becomes

$$w_\mu(\mathbf{q}, \mathbf{q}') \propto 1 + s_\mu\left[\frac{r - \cos(\theta)}{1 - r\cos(\theta)}\right]. \tag{A.18}$$

After simplification, the individual intraband transition rates can be expressed as

$$w_l(\mathbf{q}, \mathbf{q}') \propto (1 + r)\frac{1 - \cos(\theta)}{1 - r\cos(\theta)}; \tag{A.19}$$

$$w_t(\mathbf{q}, \mathbf{q}') \propto (1 - r)\frac{1 + \cos(\theta)}{1 - r\cos(\theta)}. \tag{A.20}$$

The total transition rates are found by integrating Eqs.(A.19-A.20) over all possible θ:

$$W_\mu = \int_{-\pi}^{\pi} w_\mu(\mathbf{q}, \mathbf{q}')\, d\theta \propto 1 - s_\mu\left[\frac{1 - r^2 - \sqrt{1 - r^2}}{r\sqrt{1 - r^2}}\right] = 1 + s_\mu\frac{q'}{q}$$

The distribution function after one transition is as follows

$$\mathcal{F}_1(\mathbf{q}') \propto \int_{-\pi}^{\pi} w(\mathbf{q}, \mathbf{q}')\left[1 + \alpha_0\cos(2\phi_1 - 2\theta)\right] d\theta, \tag{A.21}$$

where ϕ_1 is the angle between $\hat{\mathbf{e}}$ and $\mathbf{q}'$. Substituting Eq. (A.18) into Eq. (A.21) followed by integration yields

$$\mathcal{F}_1(\mathbf{q}') \propto 2\pi \left[1 + s_\mu \frac{1}{r}\left(1 - \sqrt{1-r^2}\right)\right] + 2\pi s_\mu \alpha_0 \frac{1}{r^3}\left[2\left(1-r^2\right) - \left(2-r^2\right)\sqrt{1-r^2}\right]\cos(2\phi) \tag{A.22}$$

Eq. (A.22) can be expressed in the form

$$\mathcal{F}_1(\mathbf{q}') = F_1(r)\left[1 + \alpha_1 \cos(2\phi)\right],$$

where

$$\alpha_1 = \alpha_0 s_\mu \frac{1}{r^3} \frac{\left[2\left(1-r^2\right) - \left(2-r^2\right)\sqrt{1-r^2}\right]}{\left[1 + s_\mu \frac{1}{r}\left(1 - \sqrt{1-r^2}\right)\right]},$$

which upon substitution for r becomes

$$\alpha_1 = -\alpha_0 s_\mu \frac{1}{2}\left(\frac{q'}{q}\right) \frac{1 - \left(\frac{q'}{q}\right)^2}{1 + s_\mu\left(\frac{q'}{q}\right)}$$

A.4 Derivation of α_1/α_0 due to SiC optical phonons

The distribution function of photoexcited carriers after an interaction with a bulk optical phonon in silicon carbide is given by the expression

$$\mathcal{F}_1(\mathbf{q}') = \int_{-\infty}^{\infty} dp_z \int_{-\pi}^{\pi} d\theta w(\mathbf{q}, \mathbf{q}')\left[1 + \alpha_0 \cos(2\phi_1 - 2\theta)\right],$$

where $\phi_1 = \varphi_{\mathbf{e}} - \varphi_{\mathbf{q}'}$ and $\theta = \varphi_{\mathbf{q}} - \varphi_{\mathbf{q}'}$. Expanding the above expression one obtains

$$\mathcal{F}_1(\mathbf{q}') \propto \int_{-\infty}^{\infty} dp_z \int_{-\pi}^{\pi} d\theta w(\mathbf{q}, \mathbf{q}')\left\{1 + \alpha_0\left[\cos(2\phi_1)\cos(2\theta) - \sin(2\phi_1)\sin(2\theta)\right]\right\}. \tag{A.23}$$

Since $w(\mathbf{q}, \mathbf{q}')$ is an even function of the angle θ, Eq. (A.23) can be expressed as

$$\mathcal{F}_1(\mathbf{q}') \propto \int_{-\infty}^{\infty} dp_z \int_{-\pi}^{\pi} d\theta w(\mathbf{q}, \mathbf{q}')\left[1 + \alpha_0 \cos(2\phi_1)\cos(2\theta)\right]. \tag{A.24}$$

Assuming that $\mathcal{F}_1(\mathbf{q}')$ can be written in the same form as Eq. (2.75):

$$\mathcal{F}_1(\mathbf{q}') \propto \left[1 + \alpha_1 \cos(2\phi_1)\right], \tag{A.25}$$

where α_1 is a dimensionless coefficient to be determined, which represents the degree of anisotropy. Using Eqs. (A.24) and (A.25), the ratio of the degrees of polarizations is found to be

$$\frac{\alpha_1}{\alpha_0} = \frac{\int_{-\infty}^{\infty} dp_z \int_{-\pi}^{\pi} d\theta w\left(\mathbf{q}, \mathbf{q}'\right) \cos\left(2\theta\right) d\theta}{\int_{-\infty}^{\infty} dp_z \int_{-\pi}^{\pi} d\theta w\left(\mathbf{q}, \mathbf{q}'\right) d\theta}. \tag{A.26}$$

This ratio is always less than one, hence the momentum distribution function becomes more isotropic after each phonon interaction. Let $I_1 = \int_{-\infty}^{\infty} dp_z \int_{-\pi}^{\pi} d\theta w\left(\mathbf{q}, \mathbf{q}'\right) \cos\left(2\theta\right) d\theta$ and $I_2 = \int_{-\infty}^{\infty} dp_z \int_{-\pi}^{\pi} d\theta w\left(\mathbf{q}, \mathbf{q}'\right) d\theta$, upon substitution of Eqs. (2.107) and (2.109) into I_1 and I_2, we obtain

$$I_1 = \int_{-\pi}^{\pi} \left[\int_{-\infty}^{\infty} \frac{\cos\left(2\theta\right)}{p_z^2 + q^2 + q'^2 - 2qq' \cos\left(\theta\right)} dp_z \right] d\theta; \tag{A.27}$$

$$I_2 = \int_{-\pi}^{\pi} \left[\int_{-\infty}^{\infty} \frac{1}{p_z^2 + q^2 + q'^2 - 2qq' \cos\left(\theta\right)} dp_z \right] d\theta. \tag{A.28}$$

Integrating with respect to p_z, using the fact that $\int_{-\infty}^{\infty} 1/\left(p_z^2 + \varepsilon^2\right) dp_z = \frac{\pi}{\varepsilon}$, results in the following expressions for integrals I_1 and I_2:

$$I_1 = 2\pi \int_{0}^{\pi} \left[\frac{\cos\left(2\theta\right)}{\sqrt{\left(q+q'\right)^2 - 4qq' \cos^2\left(\frac{\theta}{2}\right)}} \right] d\theta; \tag{A.29}$$

$$I_2 = 2\pi \int_{0}^{\pi} \left[\frac{1}{\sqrt{\left(q+q'\right)^2 - 4qq' \cos^2\left(\frac{\theta}{2}\right)}} \right] d\theta. \tag{A.30}$$

Making the change of variable $\frac{\theta}{2} = \left(\frac{\pi}{2} - \alpha\right)$ allows the ratio of the anisotropy parameters of the distribution functions (the degree of linear depolarization) , Eq. (A.26), to be expressed as

$$\frac{\alpha_1}{\alpha_0} = \frac{\int_0^{\frac{\pi}{2}} \left[\frac{\cos(4\alpha)}{\sqrt{1 - R^2 \sin^2(\alpha)}} \right] d\alpha}{\int_0^{\frac{\pi}{2}} \left[\frac{1}{\sqrt{1 - R^2 \sin^2(\alpha)}} \right] d\alpha} = \frac{\int_0^{\frac{\pi}{2}} \left[\frac{\cos(4\alpha)}{\sqrt{1 - R^2 \sin^2(\alpha)}} \right] d\alpha}{\boldsymbol{K}\left(R\right)}, \tag{A.31}$$

where $R^2 = \frac{4qq'}{(q+q')^2}$ and $\boldsymbol{K}$ is the complete elliptic integral of the first kind. In fact, I_1 can be expressed in terms of elliptic integrals of the first and second kind. Eq (A.29) can be expressed as

$$I_1 = 4\pi \int_{0}^{\pi} \left[\frac{\cos^2\left(\theta\right)}{\sqrt{q^2 + q'^2 - 2qq' \cos\left(\theta\right)}} \right] d\theta - I_2 \tag{A.32}$$

and I_2 in terms of the variable $\alpha = \frac{\pi}{2} - \frac{\theta}{2}$ is given by,

$$I_2 = \frac{4\pi}{(q+q')} \int_0^{\frac{\pi}{2}} \left[\frac{1}{\sqrt{1 - \frac{4qq'}{(q+q')^2} \sin^2(\alpha)}} \right] d\alpha = \frac{4\pi}{(q+q')} \boldsymbol{K}(R). \tag{A.33}$$

The integral $\int_0^{\pi} \frac{\cos^2(\theta)}{\sqrt{q^2+q'^2-2qq'\cos(\theta)}} d\theta$ contained within Eq. (A.32) has the known solution [182]

$$\frac{2}{3b^2\sqrt{a+b}} \left[\left(2a^2 + b^2\right) \boldsymbol{K}(R) - 2a(a+b) \boldsymbol{E}(R) \right], \tag{A.34}$$

where $a = q^2 + q'^2$, $b = 2qq'$ and $\boldsymbol{E}$ is the complete elliptic integral of the second kind. Substituting for a and b into Eq. (A.34) yields

$$\frac{2}{3(2qq')^2(q+q')} \left\{ \left[2\left(q^2+q'^2\right)^2 + (2qq')^2 \right] \boldsymbol{K}(R) - 2\left(q^2+q'^2\right)(q+q')^2 \boldsymbol{E}(R) \right\}. \tag{A.35}$$

This result allows the integral, I_1 to be expressed as

$$I_1 = \frac{4\pi}{3(q+q')(qq')^2} \left\{ \left[\left(q^2+q'^2\right)^2 - (qq')^2 \right] \boldsymbol{K}(R) - \left(q^2+q'^2\right)(q+q')^2 \boldsymbol{E}(R) \right\}. \tag{A.36}$$

Thus the ratio of the anisotropy parameters is given by

$$\frac{\alpha_1}{\alpha_0} = \frac{1}{3q^2q'^2} \left[\left(q^2+q'^2\right)^2 - q^2q'^2 - \left(q^2+q'^2\right)(q+q')^2 \frac{\boldsymbol{E}(R)}{\boldsymbol{K}(R)} \right]. \tag{A.37}$$

Appendix B

Appendices to chapter 2

B.1 Matrix element of optical transitions incorporating curvature

In the frame of the tight binding model, the matrix element $\mathbf{e}\cdot\langle\psi_f\mid\hat{v}_z\mid\psi_i\rangle$ can be written as

$$\frac{i}{\hbar}\mathbf{i}\cdot\Re\left[\frac{\tilde{f}_k^\star}{\sqrt{\left|\tilde{f}_k\right|^2}}\sum_{i=1}^{3}e^{i\mathbf{k}\cdot\mathbf{u_i}^\star}t_i^\star\mathbf{u}_i^\star\right], \tag{B.1}$$

where $\mathbf{i}$ is the unit vector of $\mathbf{x}$,

$$\tilde{f}_k = t\exp\left(i\frac{k_x a}{\sqrt{3}}\right)+2t_2^\star\exp\left(-i\frac{k_x a}{2\sqrt{3}}\right)\cos\left(k_y a_y\right)$$

and

$$\mathbf{u}_i^\star=\left(\frac{a}{\sqrt{3}},0\right),\left(-\frac{a}{2\sqrt{3}},-a_y\right),\left(-\frac{a}{2\sqrt{3}},a_y\right).$$

Substituting for $\mathbf{u}_i^\star$ and $\tilde{f}_k$, Eq. (B.1) becomes

$$\begin{aligned}i\frac{at^2}{\sqrt{3}\hbar}\frac{1}{\sqrt{|f_k|}}\Re\Bigg[1-\left(\frac{t_2^\star}{t}\right)\exp\left(-i\frac{\sqrt{3}}{2}k_x a\right)\cos\left(k_y a_y\right)\\ +2\left(\frac{t_2^\star}{t}\right)\exp\left(i\frac{\sqrt{3}}{2}k_x a\right)\cos\left(k_y a_y\right)-2\left(\frac{t_2^\star}{t}\right)^2\cos^2\left(k_y a_y\right)\Bigg]\end{aligned} \tag{B.2}$$

and retaining the real terms only, Eq. (B.2) reduces to

$$i\frac{4\hbar v_F^2}{3\sqrt{3}a}\frac{1}{\sqrt{\left|\tilde{f}_k\right|}}\left[1-2\left(\frac{t_2^\star}{t}\right)^2\cos^2\left(k_y a_y\right)+\frac{t_2^\star}{t}\cos\left(\frac{\sqrt{3}}{2}k_x a\right)\cos\left(k_y a_y\right)\right]. \tag{B.3}$$

By expanding and retaining first order terms only we obtain

$$i\frac{4\hbar v_F^2}{3\sqrt{3}a}\frac{1}{\sqrt{\left|\tilde{f}_k\right|}}\left[1+\frac{t_2^\star}{t}\cos\left(k_y a_y\right)-2\left(\frac{t_2^\star}{t}\right)^2\cos^2\left(k_y a_y\right)-\frac{t_2^\star}{t}\frac{1}{2}\left(\frac{\sqrt{3}}{2}k_x a\right)^2\cos\left(k_y a_y\right)\right]. \tag{B.4}$$

In the vicinity of the point $k_x = 0$ the low energy spectrum takes the form

$$\xi = s\sqrt{\left(\frac{\xi_g}{2}\right)^2-2\frac{t_2^\star}{t}\cos\left(k_y a_y\right)\left(v_{\mathrm{F}}\hbar k_x\right)^2}, \tag{B.5}$$

using this definition Eq. (B.4) can be re-expressed in terms of ξ:

$$i\frac{2\hbar v_F^2}{3\sqrt{3}a}\frac{1}{\sqrt{\left|\tilde{f}_k\right|}}\left[2+2\frac{t_2^\star}{t}\cos\left(k_y a_y\right)-4\left(\frac{t_2^\star}{t}\right)^2\cos^2\left(k_y a_y\right)+\frac{1}{2t^2}\left\{\xi^2-\left[t+2t_2^\star\cos\left(k_y a_y\right)\right]^2\right\}\right]. \tag{B.6}$$

With further simplification we obtain

$$i\frac{4\hbar v_F^2}{3\sqrt{3}a}\frac{1}{\sqrt{\left|\tilde{f}_k\right|}}\left[\frac{3}{4}-3\left(\frac{t_2^\star}{t}\right)^2\cos^2\left(k_y a_y\right)+\frac{1}{4}\left(\frac{\xi}{t}\right)^2\right]. \tag{B.7}$$

In the dipole approximation [128] the spectral density is given by:

$$I_\nu = \frac{8\pi e^2\nu}{3c^3}\sum_{i,f} f_e\left(k_i\right) f_h\left(k_f\right)\left|\mathbf{e}\cdot\left\langle\psi_f\left|\hat{v}_z\right|\psi_i\right\rangle\right|^2\delta\left(\xi_i-\xi_f-h\nu\right), \tag{B.8}$$

where ψ_i and ψ_f are the eigenfunctions of the electrons in the initial and final states, ξ_i and ξ_f are their associated energies, and k_i and k_f are their associated wave vectors. By changing the sum, appearing in Eq. (B.8), to an integral over equi-energy surfaces, Eq. (B.8) can be re-expressed as

$$I_\nu = 2\times\left(\frac{L}{2\pi}\right)\times\frac{8\pi e^2\nu}{3c^3} f_e\left(k_i\right) f_h\left(k_f\right)\left|\mathbf{e}\cdot\left\langle\psi_f\left|\hat{v}_z\right|\psi_i\right\rangle\right|^2\frac{1}{\frac{d\xi}{dk_x}}\delta\left(\xi_i-\xi_f-h\nu\right), \tag{B.9}$$

where the additional factor of two takes into account valley degeneracy. Let us now consider $\frac{d\xi}{dk_x}$ given by the expression

$$\frac{d\xi}{dk_x} = -2\frac{1}{\xi}\hbar^2 v_{\mathrm{F}}^2\left(\frac{t_2^\star}{t}\right)\cos\left(k_y a_y\right)k_x, \tag{B.10}$$

which in terms of energy becomes

$$\frac{d\xi}{dk_x} = \frac{\hbar v_{\mathrm{F}}}{\xi}\sqrt{-2\frac{t_2^\star}{t}\cos\left(k_y a_y\right)\left[\xi^2 - \left(\frac{\xi_g}{2}\right)^2\right]}. \tag{B.11}$$

Eqs. (B.7, B.11, B.9) yield;

$$I_\nu = L\frac{32}{27}\frac{e^2\nu v_F}{c^3\hbar}\frac{t}{\xi}\frac{\left[\frac{3}{4} - 3\left(\frac{t_2^\star}{t}\right)^2\cos^2\left(k_y a_y\right) + \frac{1}{4}\left(\frac{\xi}{t}\right)^2\right]^2}{\sqrt{-2\frac{t_2^\star}{t}\cos\left(k_y a_y\right)\left[\left(\frac{\xi}{t}\right)^2 - \left(\frac{\xi_g}{2t}\right)^2\right]}} f_e\left(\frac{\pi\nu}{v_{\mathrm{F}}}\right) f_h\left(\frac{\pi\nu}{v_{\mathrm{F}}}\right)\delta\left(\xi_i - \xi_f - h\nu\right), \tag{B.12}$$

B.2 Armchair carbon nanotube in a magnetic field

Graphene's effective matrix Hamiltonian following the notations of Ref. [35] is given by

$$H = t\begin{bmatrix} 0 & f_k \\ f_k^\star & 0 \end{bmatrix}$$

and the corresponding eigenvalues are

$$\xi = \pm\left|t\right|\sqrt{\left|f_k\right|^2},$$

where

$$f_k = \exp\left(i\frac{a}{\sqrt{3}}k_x\right) + 2\exp\left(-i\frac{a}{2\sqrt{3}}k_x\right)\cos\left(k_y\frac{a}{2}\right). \tag{B.13}$$

For an armchair carbon nanotube defined by (n, n), k_x is quantized in the following manner

$$k_x = \frac{2\pi}{a\sqrt{3}}\frac{l}{n},$$

where l is an integer. Defining k_T as the projection of the wave vector along the nanotube axis Eq. (B.13) can be expressed as

$$f_k = \exp\left(i\frac{2\pi}{3}\frac{l}{n}\right) + 2\exp\left(-i\frac{\pi}{3}\frac{l}{n}\right)\cos\left(k_T\frac{a}{2}\right). \tag{B.14}$$

In the presence of a magnetic field, $l \to l + \mathcal{F}$ (here $\mathcal{F} = \Phi/\Phi_0$) and the armchair carbon

nanotube energy spectrum becomes

$$\xi = \pm |t| \sqrt{1 + 4\cos\left(\pi \frac{l+\mathcal{F}}{n}\right)\cos\left(k_T \frac{a}{2}\right) + 4\cos^2\left(k_T \frac{a}{2}\right)}. \tag{B.15}$$

We are solely interested in the lowest conduction and the highest valence subbands, which corresponds to $l = n$, in this instance the subbands energy spectra are

$$\xi = \pm |t| \sqrt{1 - 4\cos\left(\pi \frac{\mathcal{F}}{n}\right)\cos\left(k_T \frac{a}{2}\right) + 4\cos^2\left(k_T \frac{a}{2}\right)}, \tag{B.16}$$

where the $+$ $(-)$ sign denotes the lowest conduction (highest valence) subband. The introduction of a magnetic field along the nanotube axis shifts the minimum in the spectrum away from $k_T = 2\pi/3a$, the electrons "acquire mass" and a band gap is opened. The new minimum, $k_T^{\min}$, is obtained by differentiating Eq. (B.16) and equating it to zero, this yields:

$$\frac{1}{2}\cos\left(\pi \frac{\mathcal{F}}{n}\right) = \cos\left(k_T^{\min} \frac{a}{2}\right). \tag{B.17}$$

Since we are interested in particle behavior in the vicinity of $k_T^{\min}$, it is natural to re-express the electron energy spectrum in terms of q_T, defined as the momentum measured relative to $k_T^{\min}$ i.e. $k_T = k_T^{\min} + q_T$, thus Eq. (B.14) can be expressed by

$$f_k = \exp\left[-i\frac{\pi}{3}\left(1 + \frac{\mathcal{F}}{n}\right)\right]\left\{-\exp\left(i\pi\frac{\mathcal{F}}{n}\right) + 2\cos\left[\left(k_T^{min} + q_T\right)\frac{a}{2}\right]\right\}.$$

Using the identity Eq. (B.17) f_k becomes:

$$f_k = \exp\left[-i\frac{\pi}{3}\left(1 + \frac{\mathcal{F}}{n}\right)\right]\left[-\exp\left(i\pi\frac{\mathcal{F}}{n}\right)\right.$$

$$\left. + \cos\left(\pi\frac{\mathcal{F}}{n}\right)\cos\left(\frac{1}{2}aq_T\right) - 2\sqrt{1 - \frac{1}{4}\cos^2\left(\pi\frac{\mathcal{F}}{n}\right)}\sin\left(\frac{1}{2}aq_T\right)\right]. \tag{B.18}$$

Expanding Eq. (B.18) in terms of q_T and retaining first order terms only yields

$$f_k = \exp\left[-i\frac{\pi}{3}\left(1 + \frac{\mathcal{F}}{n}\right)\right]\left[-i\sin\left(\pi\frac{\mathcal{F}}{n}\right) - \sqrt{1 - \frac{1}{4}\cos^2\left(\pi\frac{\mathcal{F}}{n}\right)}aq_T\right]. \tag{B.19}$$

For brevity let $\Theta = \frac{\pi}{3}\left(1 + \frac{\mathcal{F}}{n}\right)$, the effective matrix Hamiltonian can therefore be written as:

$$t\begin{bmatrix} 0 & \exp\left(-i\Theta\right)\left[-i\sin\left(\pi\frac{\mathcal{F}}{n}\right)-\sqrt{1-\frac{1}{4}\cos^2\left(\pi\frac{\mathcal{F}}{n}\right)}a\hat{q}\right] \\ \exp\left(i\Theta\right)\left[i\sin\left(\pi\frac{\mathcal{F}}{n}\right)-\sqrt{1-\frac{1}{4}\cos^2\left(\pi\frac{\mathcal{F}}{n}\right)}a\hat{q}\right] & 0 \end{bmatrix}, \tag{B.20}$$

which acts on a two-component Dirac wavefunction given by

$$\begin{bmatrix} C_1\left(y\right) \\ C_2\left(y\right) \end{bmatrix}, \tag{B.21}$$

where $C_1\left(y\right)$ and $C_2\left(y\right)$ are the wavefunctions associated with the A and B sub-lattices of graphene respectively and $\hat{q}=-i\frac{\partial}{\partial y}$. By changing the basis wavefunctions from C_1 and C_2 to $\psi_A=-C_1$ and $\psi_B=-\exp\left(-i\Theta\right)C_2$, and changing the variable $y\rightarrow -x$, so that the x-coordinate is now along the nanotube axis, the effective matrix Hamiltonian can be expressed as

$$\hat{H}_0=|t|\begin{bmatrix} 0 & \sqrt{1-\frac{1}{4}\cos^2\left(\pi\frac{\mathcal{F}}{n}\right)}a\hat{q}-i\sin\left(\pi\frac{\mathcal{F}}{n}\right) \\ \sqrt{1-\frac{1}{4}\cos^2\left(\pi\frac{\mathcal{F}}{n}\right)}a\hat{q}+i\sin\left(\pi\frac{\mathcal{F}}{n}\right) & 0 \end{bmatrix}, \tag{B.22}$$

which acts on the two-component Dirac wavefunction

$$\begin{bmatrix} \psi_A \\ \psi_B \end{bmatrix}. \tag{B.23}$$

For brevity let $b=\sqrt{\frac{4}{3}-\frac{1}{3}\cos^2\left(\frac{\pi}{n}f\right)}$ and $\Delta=\frac{2}{a\sqrt{3}}\sin\left(\frac{\pi}{n}f\right)$:

$$\hat{H}_0=\hbar v_{\mathrm{F}}\begin{bmatrix} 0 & b\hat{q}-i\Delta \\ b\hat{q}+i\Delta & 0 \end{bmatrix}, \tag{B.24}$$

where now $\hat{q}=-i\frac{\partial}{\partial x}$.

B.3 Derivation of the analytic solution for $\xi=0$

For the case of $K=0$, corresponding to the static exciton, the equation for the wavefunction of relative motion reads

$$\begin{bmatrix} 0 & \hat{k}-i\Delta & \hat{k}+i\Delta & 0 \\ \hat{k}+i\Delta & 0 & 0 & \hat{k}+i\Delta \\ \hat{k}-i\Delta & 0 & 0 & \hat{k}-i\Delta \\ 0 & \hat{k}-i\Delta & \hat{k}+i\Delta & 0 \end{bmatrix}\begin{bmatrix} \phi_{AA} \\ \phi_{BA} \\ \phi_{AB} \\ \phi_{BB} \end{bmatrix}=\left[\varepsilon-\tilde{V}\left(x\right)\right]\begin{bmatrix} \phi_{AA} \\ \phi_{BA} \\ \phi_{AB} \\ \phi_{BB} \end{bmatrix}$$

where $\varepsilon = \xi/\left(\hbar v_{\mathrm{F}}\right), \tilde{V} = V/\left(\hbar v_{\mathrm{F}}\right)$. Since $\phi_{AA} = \phi_{BB}$ the system of equations reduces to

$$\phi_{BA} = \frac{2}{\left[\varepsilon - \tilde{V}\left(x\right)\right]}\left(\hat{k} + i\Delta\right)\phi_{AA} \tag{B.25}$$

$$\phi_{AB} = \frac{2}{\left[\varepsilon - \tilde{V}\left(x\right)\right]}\left(\hat{k} - i\Delta\right)\phi_{AA} \tag{B.26}$$

$$\left(\hat{k} - i\Delta\right)\phi_{BA} + \left(\hat{k} + i\Delta\right)\phi_{AB} = \left[E - V\left(y\right)\right]\phi_{AA} \tag{B.27}$$

Substituting Eq. (B.25) and Eq. (B.26) into Eq. (B.27) yields

$$\frac{d^2\phi_{AA}}{dx^2} + \frac{1}{\left[\varepsilon - \tilde{V}\left(x\right)\right]}\frac{d\tilde{V}\left(x\right)}{dx}\frac{d\phi_{AA}}{dx} + \left\{\frac{\left[\varepsilon - \tilde{V}\left(x\right)\right]^2}{4} - \Delta^2\right\}\phi_{AA} = 0. \tag{B.28}$$

Let us now consider the case of

$$\tilde{V}\left(x\right) = -\frac{\alpha}{\cosh\left(\beta x\right)}$$

and $\varepsilon = 0$. Making the change of variable $z = \beta x$, Eq. (B.28) becomes

$$\frac{d^2\phi_{AA}}{dz^2} + \tanh\left(z\right)\frac{d\phi_{AA}}{dz} + \left[-\frac{1}{4}\omega^2\tanh^2\left(z\right) + \frac{1}{4}\omega^2 - \tilde{\Delta}^2\right]\phi_{AA} = 0, \tag{B.29}$$

where $\omega = \alpha/\beta$ and $\tilde{\Delta} = \Delta/\beta$. The change of variable $\chi = \tanh\left(z\right)$ allows Eq. (B.29) to be expressed as

$$\left(\chi^2 - 1\right)^2\frac{\partial^2\phi_{AA}}{\partial\chi^2} + \chi\left(\chi^2 - 1\right)\frac{\partial\phi_{AA}}{\partial\chi} + \left(c\chi^2 + e\right)\Psi_{AA} = 0, \tag{B.30}$$

where $c = -\frac{1}{4}\omega^2$ and $e = \frac{1}{4}\omega^2 - \Delta^2$. Eq. (B.30) is of a known form and has the solution [181]

$$\phi_{AA} = A_1\left(\chi + 1\right)^p\left(\chi - 1\right)^q\eta\left[\frac{1}{2}\left(\chi + 1\right)\right], \tag{B.31}$$

where A_1 is a constant, the function $\eta\left[\frac{1}{2}\left(\chi + 1\right)\right]$ is to be found and p and q are found from the following conditions

$$4q\left(q - 1\right) + 2q + c + e = 0; \qquad \left(p - q\right)\left[2\left(p + q\right) - 1\right] = 0. \tag{B.32}$$

Eqs. (B.31, B.30, B.32) yield;

$$\left(\chi^2 - 1\right)\frac{\mathrm{d}^2\eta}{\mathrm{d}\chi^2} + \left[\left(2p + 2q + 1\right)\chi - 2\left(p - q\right)\right]\frac{\mathrm{d}\eta}{\mathrm{d}\chi} + \left[\left(p + q\right)^2 + c\right]\eta = 0. \tag{B.33}$$

Performing a change of variable $\kappa \to (\chi+1)/2$ reduces Eq. (B.33) to the hypergeometric equation

$$\kappa(\kappa-1)\frac{\mathrm{d}^2\eta}{\mathrm{d}\kappa^2} + [(a_1+a_2+1)\kappa - a_3]\frac{\mathrm{d}\eta}{\mathrm{d}\kappa} + a_1 a_2 \eta = 0,$$

where $a_1 = p+q\pm\sqrt{-c}$, $a_2 = p+q\mp\sqrt{-c}$ and $a_3 = 2p+\frac{1}{2}$. Thus the form of η is

$$\eta = {}_2\mathrm{F}_1\left(p+q-\sqrt{-c}, p+q+\sqrt{-c}; 2p+\frac{1}{2}; \kappa\right). \tag{B.34}$$

Hence the wavefunction ϕ_{AA} is given by:

$$\phi_{AA} = A_1(1+\chi)^p(1-\chi)^q\,{}_2\mathrm{F}_1\left(p+q-\frac{\omega}{2}, p+q+\frac{\omega}{2}; 2p+\frac{1}{2}; \frac{1+\chi}{2}\right). \tag{B.35}$$

From Eq. (B.32), q is found to be

$$q = \frac{1\pm\sqrt{1+4\tilde{\Delta}^2}}{4}, \tag{B.36}$$

and p can take the values

$$p = q \tag{B.37}$$

or

$$p = \frac{1}{2} - q. \tag{B.38}$$

Let us first consider the case of $p=q$. In this instance Eq. (B.35) becomes

$$\phi_{AA} = A_1\left[1-\tanh^2(z)\right]^q\,{}_2\mathrm{F}_1\left(2q-\frac{\omega}{2}, 2q+\frac{\omega}{2}; 2q+\frac{1}{2}; \frac{1+\tanh(z)}{2}\right). \tag{B.39}$$

For the function ϕ_{AA} to vanish as $z\to\infty$ we require

$$q = \frac{1\pm\sqrt{1+4\tilde{\Delta}^2}}{4} > 0 \tag{B.40}$$

and that the hypergeometric series is terminated. This can be satisfied if we take the positive root of q and restrict ω such that $2q-\frac{\omega}{2} = -n$, where n is a positive integer, thus we arrive at the condition that

$$\omega = 1+2n+\sqrt{1+4\tilde{\Delta}^2}. \tag{B.41}$$

ϕ_{BA} and ϕ_{AB}, which can be found from Eq. (B.25) and Eq. (B.26), must also vanish as $z\to\infty$. For simplicity lets analyze the linear combinations $\Psi_+ = \phi_{BA}+\phi_{AB}$ and $\Psi_- = \phi_{BA}-\phi_{AB}$:

$$\Psi_+ = i\frac{4\beta}{V(z)}\frac{\partial\phi_{AA}}{\partial z} = -i\frac{4}{\omega}\cosh(z)\frac{\partial\phi_{AA}}{\partial z} \tag{B.42}$$

$$\Psi_- = -i\frac{4\Delta}{V(z)}\phi_{AA} = i\frac{4\tilde{\Delta}}{\omega}\cosh(z)\,\phi_{AA} \tag{B.43}$$

For Eq. (B.42) and Eq. (B.43) to vanish in the limit that $z \to \infty$ we require

$$q = \frac{1+\sqrt{1+4\tilde{\Delta}^2}}{4} > \frac{1}{2}. \tag{B.44}$$

This is automatically satisfied for any finite $\tilde{\Delta}$, therefore providing ϕ_{AA} vanishes as $z \to \infty$ ϕ_{BA} and ϕ_{AB} will also vanish.

Let us now consider the case of $p+q=\frac{1}{2}$, in this instance Eq. (B.35) becomes

$$\phi_{AA} = \tilde{A}_1\left(1-\chi^2\right)^q(1+\chi)^{\frac{1}{2}-2q}\,{}_2\mathrm{F}_1\left(\frac{1}{2}-\frac{\omega}{2},\,\frac{1}{2}+\frac{\omega}{2};\,\frac{3}{2}-2q;\,\frac{1+\chi}{2}\right). \tag{B.45}$$

using the identity [182]

$$z^{1-c}\,{}_2\mathrm{F}_1(a+1-c,\,b+1-c;\,2-c;\,z) = {}_2\mathrm{F}_1(a,\,b;\,c;\,z), \tag{B.46}$$

where $a = 2q-\frac{\omega}{2}$, $b = 2q+\frac{\omega}{2}$, $c = 2q+\frac{1}{2}$ and $z = (1+\chi)/2$, Eq. (B.45) becomes

$$\phi_{AA} = \tilde{A}_2\left[1-\tanh^2(z)\right]^q\,{}_2\mathrm{F}_1\left(2q-\frac{\omega}{2},\,2q+\frac{\omega}{2};\,2q+\frac{1}{2};\,\frac{1+\tanh(z)}{2}\right), \tag{B.47}$$

where $\tilde{A}_2$ is a constant. This is of the same form as Eq. (B.39).

B.4 Excitons with an attractive delta-function potential

The problem of calculating the energy of an exciton in a carbon nanotube can be solved exactly in the case when the interaction potential between the electron and hole is taken to be a delta-function, $\tilde{V}(x) = -U_0\delta(x)$, where the strength of the potential U_0 is positive and can be estimated as a product of the depth of the potential and its width.

Consider an electron-hole pair in a narrow-gap 1D carbon nanotube, with a band gap energy $4|\Delta|$ and measuring all the quantities in the units $\hbar v_F$ as in section 3.7 one can write the Hamiltonian as

$$\widehat{H} = \sqrt{\Delta^2+\widehat{q}_e^2} + \sqrt{\Delta^2+\widehat{q}_h^2} + V(|x_e-x_h|), \tag{B.48}$$

where

$$\widehat{q}_{e,h} = -i\frac{\partial}{\partial x_{e,h}}. \tag{B.49}$$

where we retained only the eigenstates of the general graphene-type Hamiltonian with positive

energies. The Schrödinger equation for the problem we consider thus reads

$$\left[\sqrt{\Delta^2+\widehat{q}_e^2}+\sqrt{\Delta^2+\widehat{q}_h^2}+V(|x_e-x_h|)\right]\Psi(x_e,x_h)=\varepsilon\Psi(x_e,x_h). \tag{B.50}$$

Introducing new variables corresponding to the center of mass and relative motion, in the manner explained in section 3.7, and putting the wave vector of the center of mass motion equal to zero, one gets the following expression

$$2\sqrt{\Delta^2-\frac{d^2}{dx^2}}\psi(x)=\left[\varepsilon-\widetilde{V}(x)\right]\psi(x) \tag{B.51}$$

where $\psi(x)$ is a wavefunction of the relative motion. The above expression is a 1D Schrödinger equation for a particle with a complicated dispersion placed in an external potential $\widetilde{V}(x)$, which can be solved for the case when $\tilde{V}(x)=-U_0\delta(x)$. Indeed, in this case the solution of a Schrödinger equation corresponding to a bound state reads

$$\psi(x)=Ae^{\kappa(\epsilon)x},\ x<0, \tag{B.52}$$

$$\psi(x)=Ae^{-\kappa(\epsilon)x},\ x>0, \tag{B.53}$$

where $\varepsilon=2\sqrt{\Delta^2+\kappa^2}$. It is well known that the zero-range delta potential is equivalent to the introduction of the specific boundary condition for the derivative of the solution at $x=0$ (the function itself should be continuous, $\psi(+0)=\psi(-0)$). To obtain a condition for the derivative, let us integrate the Schrödinger equation

$$\left[\widehat{H}_0\left(\frac{d}{dx}\right)-\varepsilon\right]\psi(x)=U_0\delta(x)\psi(x), \tag{B.54}$$

where $\widehat{H}_0\left(\frac{d}{dx}\right)=2\sqrt{\Delta^2+\frac{d^2}{dx^2}}$ across the interval $[-0;+0]$. One has

$$\int\widehat{H}_0\left(\frac{d}{dx}\right)\psi(x)dx|_{x=+0}-\int\widehat{H}_0\left(\frac{d}{dx}\right)\psi(x)dx|_{x=-0}=U_0\psi(0). \tag{B.55}$$

Using this relation and Eqs. (B.52), (B.53) and (B.51) one gets the following expression for determining parameter κ

$$H_0(-\kappa)+H_0(\kappa)-2H_0(0)=-\kappa U_0. \tag{B.56}$$

Thus,

$$\sqrt{\Delta^2-\kappa^2}=\Delta-\frac{\kappa U_0}{4}, \tag{B.57}$$

which yields

$$\kappa = \frac{8U_0\Delta}{16 + U_0^2}, \tag{B.58}$$

where the energy is given by

$$\varepsilon = 2\sqrt{\Delta^2 - \kappa^2}. \tag{B.59}$$

Note, that this result is valid only for the case of $U_0 < 4$, as for $U_0 > 4$, the right hand side of Eq. (B.57) is negative.

The binding energy of the exciton can be determined as

$$\varepsilon_b = 2\Delta - \epsilon = 4\Delta U_0^2/(16 + U_0^2), \tag{B.60}$$

which tends to the non-relativistic result $\varepsilon_b = U_0^2\Delta/4$ for $U_0 \ll 1$. Note, that in both relativistic and non-relativistic cases the value of the binding energy is proportional to the value of the gap.

Appendix C

Appendices to chapter 3

C.1 Wavefunction derivation in the potential $V(x) = -\frac{\alpha}{\cosh(\beta x)}$

This problem is much easier to solve in the non-symmetrized Ψ_A/Ψ_B basis. Starting from the tight-binding Hamiltonian one obtains the following system of first-order differential equations

$$\begin{aligned} \left[V(x) - \epsilon\right]\Psi_A - i\left(\frac{\mathrm{d}}{\mathrm{d}x} + q_y\right)\Psi_B &= 0, \\ -i\left(\frac{\mathrm{d}}{\mathrm{d}x} - q_y\right)\Psi_A + \left[V(x) - \epsilon\right]\Psi_B &= 0. \end{aligned}$$

Where q_y characterizes the momentum in the y-direction and $\Psi_{A(B)}$ are the x-components of the $A\,(B)$ sublattice wavefunctions. For $\epsilon = 0$ elimination of Ψ_A yields

$$\frac{\mathrm{d}^2\Psi_B}{\mathrm{d}x^2} - \frac{1}{V(x)}\frac{\mathrm{d}V(x)}{\mathrm{d}x}\frac{\mathrm{d}\Psi_B}{\mathrm{d}x} + \left[V(x)^2 - q_y^2 - \frac{q_y}{V(x)}\frac{\mathrm{d}V(x)}{\mathrm{d}x}\right]\Psi_B = 0.$$

For the potential given by $V(x) = -\frac{\alpha}{\cosh(\beta x)}$ and making a change of variable, $\xi = \tanh(\beta x)$, this becomes

$$(1-\xi^2)^2\frac{\mathrm{d}^2\Psi_B}{\mathrm{d}\xi^2} - 2\xi\left(1-\xi^2\right)\frac{\mathrm{d}\Psi_B}{\mathrm{d}\xi} + \left[\omega^2\left(1-\xi^2\right) + \Delta\xi - \Delta^2\right]\Psi_B = 0,$$

where $\Delta = q_y/\beta$ and $\omega = \alpha/\beta$. This equation is reduced to the standard form

$$a(\chi^2-1)y" + b\chi\left(\chi^2-1\right)y' + \left(c\chi^2 + d\chi + e\right)y = 0, \tag{C.1}$$

where

$$a = 1,\ b = 1,\ c = -\omega^2,\ d = \Delta \text{ and } e = \omega^2 - \Delta^2. \tag{C.2}$$

Eq. (C.1) is of a known form, which has the solutions [181]

$$y = (\chi+1)^p (\chi-1)^q \eta\left[\frac{1}{2}(\chi+1)\right], \tag{C.3}$$

where the function $\eta\left[\frac{1}{2}(\chi+1)\right]$ is to be found and p and q are found from the following conditions:

$$4aq(q-1)+2bq+c+d+e=0; \quad (p-q)[2a(p+q-1)+b]=d. \tag{C.4}$$

We find the functional form of $\eta\left[\frac{1}{2}(\chi+1)\right]$ by substituting Eq. (C.3) into Eq. (C.1) which yields

$$\begin{aligned}\left(\chi^2-1\right)^2\frac{\mathrm{d}^2\eta}{\mathrm{d}\chi^2}+\left(\chi^2-1\right)[2p(\chi-1)+2q(\chi+1)+\chi]\frac{\mathrm{d}\eta}{\mathrm{d}\chi}+\\ +[2pq\left(\chi^2-1\right)+p(p-1)(\chi-1)^2+q(q-1)(\chi+1)^2 &= 0.\\ +p\chi(\chi-1)+q\chi(\chi+1)+c\chi^2+d\chi+e]\eta\end{aligned}$$

Satisfying the conditions for p and q stated in Eq. (C.4) one obtains the equation

$$\left(\chi^2-1\right)\frac{\mathrm{d}^2\eta}{\mathrm{d}\chi^2}+[(2p+2q+1)\chi-2(p-q)]\frac{\mathrm{d}\eta}{\mathrm{d}\chi}+\left[(P+q)^2+c\right]\eta=0.$$

Performing a change of variable $\kappa \to (\chi+1)/2$ one obtains

$$\kappa(\kappa-1)\frac{\mathrm{d}^2\eta}{\mathrm{d}\kappa^2}+\left[(2p+2q-1)\kappa-\left(2p+\frac{1}{2}\right)\right]\frac{\mathrm{d}\eta}{\mathrm{d}\kappa}+\left[(p+q)^2+c\right]\eta=0.$$

This is the hypergeometric equation with redefined variables

$$\kappa(\kappa-1)\frac{\mathrm{d}^2\eta}{\mathrm{d}\kappa^2}+[(a_1+a_2+1)\kappa-a_3]\frac{\mathrm{d}\eta}{\mathrm{d}\kappa}+a_1a_2\eta=0,$$

where $a_1 = p+q\pm\sqrt{-c}$, $a_2 = p+q\mp\sqrt{-c}$ and $a_3 = 2p+\frac{1}{2}$. Thus the form of η is

$$\eta = {}_2\mathrm{F}_1\left(p+q+\sqrt{-c}, p+q-\sqrt{-c}; 2p+\frac{1}{2}; \kappa\right).$$

Hence the form of the wavefunction Ψ_B is found by substitution of Eq. (C.2) to be

$$\Psi_B = (1+\xi)^p(1-\xi)^q\,{}_2\mathrm{F}_1\left(p+q+\omega, p+q-\omega; 2p+\frac{1}{2}; \frac{1+\xi}{2}\right).$$

One can perform a similar derivation for Ψ_A to find

$$\Psi_A = -i(1+\xi)^q(1-\xi)^p\,{}_2\mathrm{F}_1\left(p+q+\omega, p+q-\omega; 2p+\frac{1}{2}; \frac{1-\xi}{2}\right),$$

where in both cases $q = \frac{\omega - n}{2} - \frac{1}{4}$ and $p = \frac{\omega - n}{2} + \frac{1}{4}$. One can write the non-normalized wavefunction in the symmetrized basis as

$$\begin{aligned}\Psi_{1,2} &= (1+\xi)^p (1-\xi)^q \, {}_2\mathrm{F}_1\left(p+q+\omega, p+q-\omega; 2p+\frac{1}{2}; \frac{1+\xi}{2}\right) \\ &\quad \pm (-1)^n (1+\xi)^q (1-\xi)^p \, {}_2\mathrm{F}_1\left(p+q+\omega, p+q-\omega; 2p+\frac{1}{2}; \frac{1-\xi}{2}\right)\end{aligned}$$

Bibliography

[1] K. S. Novoselov, A. K. Geim, S. V. Morozov, D. Jiang, Y. Zhang, S. V. Dubonos, I. V. Gregorieva, and A. A. Firsov, Science **306**, 666 (2004).

[2] K. S. Novoselov, D. Jiang, F. Schedin, T. J. Booth, V. V. Khotkevich, S. V. Morozov, and A. K. Geim, PNAS **102**, 10451 (2005).

[3] A. C. Ferrari, J. C. Meyer, V. Scardaci, C. Casiraghi, M. Lazzeri, F. Mauri, S. Piscanec, D. Jiang, K. S. Novoselov, S. Roth, and A. K. Geim, Phys. Rev. Lett. **97**, 187401 (2006).

[4] D. S. L. Abergel, A. Russell and V. I. Fal'ko, Appl. Phys. Lett. **91**, 063125 (2007).

[5] P. Blake, E. W. Hill, A. H. Castro Neto, K. S. Novoselov, D. Jiang, R. Yang, T. J. Booth and A. K. Geim, Appl. Phys. Lett. **91**, 063124 (2007).

[6] R. R. Nair, P. Blake, A. N. Grigorenko, K. S. Novoselov, T. J. Booth, T. Stauber, N. M. R. Peres and A. K. Geim, Science **320**, 1308 (2008).

[7] S. Akcoeltekin, M. El Kharrazi, B. Koehler, A. Lorke, M. Schleberger, Nanotechnology **20**, 155601 (2009).

[8] L. Goa, W. Ren, F. Li, H. Cheng, ACS Nano **2**, 1625 (2008).

[9] P. R. Wallace, Phys. Rev. **71**, 622 (1947).

[10] R. E. Peierls, Ann. I. H. Poincare **5**, 177 (1935).

[11] L. D. Landau, Phys. Z. Sowjetunion **11**, 26 (1937).

[12] K. S. Novoselov, A. K. Geim, S. V. Morozov, D. Jiang, M. I. Katsnelson, I. V. Grigorieva, S. V. Dubonos, and A. A. Firsov, Nature (London) **438**, 197 (2005).

[13] A. H. Castro Neto, F. Guinea, N. M. R. Peres, K. S. Novoselov and A. K. Geim, Rev. Mod. Phys. **81**, 109 (2007).

[14] M. I. Katsnelson, K. S. Novoselov, and A. K. Geim, Nature Phys. **2**, 620 (2006).

[15] M. I. Katsnelson, and K. S. Novoselov, Solid State Commun. **143**, 3 (2007).

[16] T. Ando, T. Nakanishi, and R. Saito, J. Phys. Soc. Jpn. **67**, 2857 (1998).

[17] Y. Zhang, Y. -W. Tan, H. L. Stormer, and P. Kim, Nature **438**, 201 (2005).

[18] V. V. Cheianov and V. I. Fal'ko, Phys. Rev. B **74**, 041403 (2006).

[19] B. Huard, J. A. Sulpizio, N. Stander, K. Todd, B. Yang, and D. Goldhaber-Gordon, Phys. Rev. Lett. **98**, 236803 (2007).

[20] B. Özyilmaz, P. Jarillo-Herrero, D. Efetov, D. A. Abanin, L. S. Levitov, and P. Kim, Phys. Rev. Lett. **99**, 166804 (2007).

[21] R. V. Gorbachev, A. S. Mayorov, A. K. Savchenko, D. W. Horsell and F. Guinea, Nano Lett. **8**, 1995 (2008).

[22] G. Liu, J. Velasco, W. Bao, and C. N. Lau, Appl. Phys. Lett. **92**, 203103 (2008).

[23] L. M. Zhang and M. M. Fogler, Phys. Rev. Lett. **100**, 116804 (2008).

[24] R. R. Hartmann, N. J. Robinson and M. E. Portnoi, Phys. Rev. B. **81**, 245431 (2010).

[25] V. V. Cheianov, V. I. Fal'ko, and B. L. Altshuler, Science **315**, 1252 (2007).

[26] F. T. Vasko and V. Ryzhii, Phys. Rev. B **77**, 195433 (2008).

[27] D. N. Mirlin and V. I. Perel, Semicond. Sci. Technol. **7**, 1221 (1992).

[28] I. A. Merkulov, V. I. Perel, and M. E. Portnoi, Sov. Phys. JETP **72**, 669 (1991).

[29] I. Žutić, J. Fabian and S. Das Sarma, Rev. Mod. Phys. **76**, 323 (2004).

[30] A. Rycerz, J. Tworzydło and C. W. J. Beenakker, Nature Phys **3**, 172 (2007).

[31] J. L. Garcia-Pomar, A. Cortijo and M. Nieto-Vesperinas, Phys. Rev. Lett., **100**, 236801 (2008).

[32] J. M Pereira Jr., F. M. Peeters, R. N. Costa Filho, and G A Farias, J. Phys.: Condens. Matter **21**, 045301 (2009).

[33] A. R. Akhmerov, J. H. Bardarson, A. Rycerz, and C. W. J. Beenakker, Phys. Rev. B **77**, 205416 (2008).

[34] A. Cresti, G. Grosso, and G. Pastori Parravicini, Phys. Rev. B **77**, 233402 (2008).

[35] R. Saito, G. Dresselhaus, and M. S. Dresselhaus, *Physical Properties of Carbon Nanotubes* (Imperial College Press, London, 1998).

[36] Yu. A. Sitenko and N. D. Vlasil, Nucl. Phys. B **787**, 241 (2008).

[37] M. I. Katsnelson, EPL **84**, 37001 (2008).

[38] A. Grüneis, R. Saito, Ge. G. Samsonidze, T. Kimura, M. A. Pimenta, A. Jorio, A. G. Souza Filho, G. Dresselhaus, and M. S. Dresselhaus, Phys. Rev. B **67**, 165402 (2003).

[39] O. V. Kibis, M. Rosenau da Costa and M. E. Portnoi, Nano Lett. **7**, 3414 (2007).

[40] A. B. Kuzmenko, E. van Heumen, F. Carbone, and D. van der Marel, Phys. Rev. Lett. **100**, 117401 (2008).

[41] M. Koshino and T. Ando, Phys. Rev. B **77**, 115313 (2008).

[42] V. Ryzhii, M. Ryzhii, and T. Otsuji, J. Appl. Phys **101**, 083114 (2007).

[43] T. Stauber, N. M. R. Peres, and A. K. Geim, Phys. Rev. B **78**, 085432 (2008).

[44] E. McCann, K. Kechedzhi, V. I. Fal'ko, H. Suzuura, T. Ando, and B. L. Altshuler, Phys. Rev. Lett. **97**, 146805 (2007).

[45] F. V. Tikhonenko, D. W. Horsell, R. V. Gorbachev, and A. K. Savchenko, Phys. Rev. Lett. **100**, 056802 (2008).

[46] L. Brey and H. A. Fertig, Phys. Rev. B **73**, 235411 (2006).

[47] I. Forbeaux, J. M. Themlin, and J. M. Debever, Phys. Rev. B **58**, 16396 (1998).

[48] E. Rollings, G. -H. Gweon, S. Y. Zhou, B. S. Mun, J. L. McChesney, B. S. Hussain, A. V. Fedorov, P. N. First, W. A. der Heer, and A. Lanzara, J. Phys. Chem. Solids **67**, 2172 (2006).

[49] A. Bostwick, T. Ohta, T. Seyller, K. Horn, and E. Rotenberg, Nature Phys. **3**, 36 (2007).

[50] C. Berger, Z. Song, X. Li, X. Wu, N. Brown, C. Naud, D. Mayou, T. Li, J. Hass, A. N. Marchenkov, E. H. Conrad, P. N. First, and W. A. de Heer, Science **312**, 1191 (2006).

[51] J. Hass, C. A. Jeffrey, R. Feng, T. Li, X. Li, Z. Song, C. Berger, W. A. de Heer, P. N. First, and E. H. Conrad, Appl. Phys. Lett. **89**, 143106 (2006).

[52] T. Ohta, A. Bostwick, T. Seyller, K. Horn, and E. Rotenberg, Science **313**, 951 (2006).

[53] P. Mallet, F. Varchon, C. Naud, L. Magaud, C. Berger, and J. -Y. Veuillen, Phys. Rev. B **76**, 041403 (2007).

[54] K. S. Kim, Y. Zhao, H. Jang, S. Y. Lee, J. M. Kim, K. S. Kim, J. Ahn, P. Kim, J. Choi, and B. H. Hong, Nature **457**, 7230 (2009).

[55] T. Shen, J. J. Gu, M. Xu, Y. Q. Wu, M. L. Bolen, M. A. Capano, L. W. Engel, and P. D. Ye, Appl. Phys. Lett. **95**, 172105 (2009).

[56] X. Wu, Y. Hu, M. Ruan, N. K Madiomanana, J. Hankinson, M. Sprinkle, C. Berger and W. A. de Hee, Appl. Phys. Lett. **95**, 223108 (2009).

[57] S. Lara-Avila, A. Kalaboukhov, S. Paolillo, M. Syväjärvi, R. Yakimova, V. Fal'ko, A. Tzalenchuk, and S. Kubatkin, Nat. Nanotechnol. **5**, 186 (2010).

[58] S. V. Morozov, K. S. Novoselov, M. I. Katsnelson, F. Schedin, L. A. Ponomarenko, D. Jiang, and A. K. Geim, Phys. Rev. Lett. **97**, 016801 (2006)

[59] C. Berger, Z. Song, T. Li, X. Li, A.Y. Ogbazghi, R. Feng, Z. Dai, A. N. Marchenkov, E. H. Conrad, P. N. First, and W. A. de Heer, J. Phys. Chem. B **108**, 19912 (2004).

[60] J. Kedzierski, P. Hsu, P. Healey, P. Wyatt, and C. Keast, IEE Trans. Electron. Devices **55**, 2078 (2008).

[61] Y. M. Lin, C. Dimitrakopoulos, K. A. Jenkins, D. B. Farmer, H.Y. Chiu, A. Grill, and Ph. Avouris, Science **327**, 662 (2010).

[62] T. Ando, J. Phys. Soc. Jpn. **75**, 124701 (2006).

[63] A. H. Castro Neto and F. Guinea, Phys Rev B **75**, 045404 (2007)

[64] F. Rana, P. A. George, J. H. Strait, J. Dawlaty, S. Shivaraman, Mvs Chandrashekhar, and M. G. Spencer, Phys Rev B **79**, 115447 (2009).

[65] V. I. Perel' and M. E. Portnoi, Sov. Phys. Semicond **26**, 1185 (1992).

[66] M. I. Dyakonov and V. I. Perel, Sov. Phys. JETP Lett. **13**, 467 (1971).

[67] M. I. Dyakonov and V. I. Perel, Phys. Lett. A **35**, 459 (1971).

[68] A. V. Kavokin, G. Malpuech, and M. M. Glazov, Phys. Rev. Lett. **95**, 136601 (2005).

[69] M. S. Dresselhaus, G. Dresselhaus, and Ph. Avouris, *Carbon Nanotubes: Synthesis, Structure, Properties, and Applications* (Springer-Verlag, Berlin, 2001).

[70] S. Reich, C. Thomsen, and J. Maultzsch, *Carbon Nanotubes: Basic Concepts and Physical Properties* (Wiley, Berlin, 2004).

[71] M. P. Anantram and F. Léonard, Rep. Prog. Phys. **69**, 507 (2006) and references therein.

[72] M. Lee and M. C. Wanke, Science **316**, 64 (2007).

[73] B. Ferguson and X. C. Zhang, Nature Mater. **1**, 26 (2002).

[74] E. A. Avrutin and M. E. Portnoi, Sov. Phys. Semicond. **22**, 968 (1988).

[75] V. V. Kruglyak and M. E. Portnoi, Techn. Phys. Lett. **31**, 1047 (2005).

[76] S. A. Mikhailov, Europhys. Lett. **79**, 27002 (2007).

[77] D. Dragoman and M. Dragoman, Progress in Quantum Electronics **28**, 1 (2004).

[78] O. V. Kibis, D. G. W. Parfitt, and M. E. Portnoi, Phys. Rev. B **71**, 035411 (2005).

[79] O. V. Kibis and M. E. Portnoi, Tech. Phys. Lett. **31**, 671 (2005).

[80] M. E. Portnoi, O. V. Kibis, and M. Rosenau da Costa, Superlatt. Microstr. **43**, 399 (2008).

[81] M. E. Portnoi, M. Rosenau da Costa, O. V. Kibis, and I. A. Shelykh, Int. J. Mod. Phys. B **23**, 2846 (2009).

[82] K. G. Batrakov, O. V. Kibis, P. P. Kuzhir, S. A. Maksimenko, M. Rosenau da Costa, and M. E. Portnoi, Physica B **405**, 3054 (2010).

[83] J. Shaver and J. Kono, Laser & Photon. Rev. **1**, 260 (2007) and references therein.

[84] S. J. Tans, M. H. Devoret, H. Dai, A. Thess, R. E. Smalley, L. J. Geerligs, and C. Dekker, Nature (London) **386**, 474 (1997).

[85] A. Nahata, A. S. Weling, and T. F. Heinz, Appl. Phys. Lett. **69**, 2321 (1996).

[86] B. Xu, Q. Hu, and M. R. Melloch, Appl. Phys. Lett. **71**, 440 (1997).

[87] G. Ramian, Nucl. Instrum. Methods Phys. Res. Sect. A **318**, 225 (1992).

[88] G. L. Carr, M. C. Martin, W. R. McKinney, K. Jordan, G. R. Neil, and G. P. Williams, Nature **420**, 153 (2002).

[89] R. Köhler, A. Tredicucci, F. Beltram, H. E. Beere, E. H. Linfield, A. G. Davies, D. A. Ritchie, R. C. Iotti, and Fausto Rossi, Nature **417**, 156 (2002).

[90] T. R. Globus, D. L. Woolard, T. Khromova, T. W. Crowe, M. Bykhovskaia, B. L. Gelmont, J. Hesler, and A. C. Samuels, J. Bio. Phys. **29**, 89 (2003).

[91] R. Parthasarathy, A. Bykhovski1, B. Gelmont, T. Globus, N. Swami, and D. Woolard, Phys. Rev. Lett. **98**, 153906 (2007).

[92] J. W. Powell, G. S. Edwards, L. Genzel, F. Kremer, A. Wittlin, W. Kubasek and W. Peticolas, Phys. Rev. A **35**, 3929 (1987).

[93] D. L. Woolard, T. R. Globus, B. L. Gelmont, M. Bykhovskaia, A. C. Samuels, D. Cookmeyer, J. L. Hesler, T. W. Crowe, J. O. Jensen, J. L. Jensen, and W. R. Loerop, Phys. Rev. E **65**, 051903 (2002).

[94] D. L. Woolard, W. R. Loerop, and M. S. Shur, *Selected Topics in Electronics and Systems* (World Scientific, Singapore, 2003), Vol. 32.

[95] P. F. Taday, I. V. Bradley, D. D. Arnone, and M. Pepper, J. Pharm. Sci. **92**, 831 (2002).

[96] H. M. Manohara, M. J. Bronikowski, M. Hoenk, B. D. Hunt, and P. H. Siegel, J. Vac. Sci. Technol. B **23**, 157 (2005).

[97] A. Di Carlo, A. Pecchina, E. Petrolati, and C. Paolini, Proc. SPIE **6328**, 632808 (2006).

[98] A. S. Maksimenko and G. Ya. Slepyan, Phys. Rev. Lett. **84**, 362 (2000).

[99] G. Pennington and N. Goldsman, Phys. Rev. B **68**, 045426 (2003).

[100] D. Dragoman and M. Dragoman, Physica E **24**, 282 (2004).

[101] A. A. Odintsov, Phys. Rev. Lett. **85**, 150 (2000).

[102] F. Léonard and J. Tersoff, Phys. Rev. Lett. **85**, 4767 (2000).

[103] M. H. Yang, K. B. K. Teo, W. I. Milne, and D. G. Hasko, Appl. Phys. Lett. **87**, 253116 (2005).

[104] C. Lu, L. An, Q. Fu, J. Liu, H. Zhang, and J. Murduck, Appl. Phys. Lett. **88**, 133501 (2006).

[105] G. Ya. Slepyan, S. A. Maksimenko, V. P. Kalosha, J. Herrmann, E. E. B. Campbell, and I. V. Hertel, Phys. Rev. A **60**, R777 (1999).

[106] G. Ya. Slepyan, S. A. Maksimenko, V. P. Kalosha, A. V. Gusakov, and J. Herrmann, Phys. Rev. A **63**, 053808 (2001).

[107] D. Dragoman and M. Dragoman, Physica E **25**, 492 (2005).

[108] M. Dragoman, A. Cismaru, H. Hartnagel, and R. Plana, Appl. Phys. Lett. **88**, 073503 (2006).

[109] G. Ya. Slepyan, M. V. Shuba, S. A. Maksimenko, and A. Lakhtakia, Phys. Rev. B **73**, 195416 (2006).

[110] T. Ando, T. Nakanishi, and R. Saito, J. Phys. Soc. Jpn. **67**, 1704 (1997).

[111] S. Roche, F. Triozon, A. Rubio, Appl. Phys. Lett. **79**, 3690 (2001)

[112] Z. Yao, C.L. Kane, and C. Dekker, Phys. Rev. Lett. **84**, 2941 (2000).

[113] A. Javey, J. Guo, M. Paulsson, Q. Wang, D. Mann, M. Lundstrom, and H. Dai, Phys. Rev. Lett. **92**, 106804 (2004).

[114] J. -Y. Park, S. Resenblatt, Yu. Yaish, V. Sazonova, H. Üstünel, S. Braig, T. A. Arias, P. W. Brouwer, and P. L. McEuen, Nano Lett. **4**, 517 (2004).

[115] V. Perebeinos, J. Tersoff, and P. Avouris, Phys. Rev. Lett. **94**, 086802 (2005).

[116] C. L. Kane and E. J. Mele, Phys. Rev. Lett. **78**, 1932 (1997).

[117] M. Ouyang, J. -L. Huang, C. L. Cheung, and C. M. Lieber, Science **292**, 702 (2001).

[118] Y. Li, U. Ravaioli, and S. V. Rotkin, Phys. Rev. B **73**, 035415 (2006).

[119] D. Gunlycke, C. J. Lambert, S. W. D. Bailey, D. G. Pettifor, G. A. D. Briggs, and J. H. Jefferson, Europhys. Lett. **73**, 759 (2006).

[120] I. Milošević, T. Vuković, S. Dmitrović, and M. Damnjanović, Phys. Rev. B **67**, 165418 (2003).

[121] J. Jiang, R. Saito, A. Grüneis, G. Dresselhaus, and M. S. Dresselhaus, Carbon **42**, 3169 (2004).

[122] A. Svizhenko and M. P. Anantram, Phys. Rev. B **72**, 085430 (2005).

[123] V. N. Popov and L. Henrard, Phys. Rev. B **70**, 115407 (2004).

[124] R. Saito, A. Grüneis, G.G. Samsonidze, G. Dresselhaus, M. S. Dresselhaus, A. Jorio, L. G. Cançado, M. A. Pimenta, and A. G. Souza Filho, Appl. Phys. A **78**, 1099 (2004).

[125] S. V. Goupalov, Phys. Rev. B **72**, 195403 (2005).

[126] Y. Oyama, R. Saito, K. Sato, J. Jiang, G. G. Samsonidze, A. Grüneis, Y. Miyauchi, S. Maruyama, A. Jorio, G. Dresselhaus, and M. S. Dresselhaus, Carbon **44**, 873 (2006).

[127] M. Y. Sfeir, T. Beetz, F. Wang, L. Huang, X. M. H. Huang, M. Huang, J. Hone, S. O'Brien, J. A. Misewich, T. F. Heinz, L. Wu, Y. Zhu, L. E. Brus, Science **312**, 554 (2006).

[128] V. B. Berestetskii, E. M. Lifshitz, and L. P. Pitaevskii, *Quantum Electrodynamics* (Butterworth-Heinemann, Oxford, 1997).

[129] M. A. Kuroda, A. Cangellaris, and J. -P. Leburton, Phys. Rev. Lett. **95**, 266803 (2005).

[130] K. Hata, D. N. Futaba, K. Mizuno, T. Namai, M. Yumura, S. Iijima, Science **306**, 1362 (2004).

[131] W. A. Harrison, *Electronic Structure and the Properties of Solids* (Dover Press, New York, 1989).

[132] G. Fedorov, A. Tselev, D. Jiménez, S. Latil, N. G. Kalugin, P. Barbara, D. Smirnov, and S. Roche, Nano Lett. **7**, 960 (2007).

[133] H. Ajiki and T. Ando, J. Phys. Soc. Jpn. **62**, 1255 (1993).

[134] J. M. Luttinger, Phys. Rev. **84** 814 (1951).

[135] J.-C. Charlier, X. Blase, and S. Roche, Rev. Mod. Phys. **79**, 677 (2007).

[136] S. M. Bachilo, M. S. Strano, C. Kittrell, R. H. Hauge, R. E. Smalley, and R. B. Weisman, Science **298**, 2361 (2002).

[137] A. Hartschuh, H. N. Pedrosa, L. Novotny, and T. D. Krauss, Science **301**, 1354 (2003).

[138] F. Wang, G. Dukovic, L. E. Brus, and T. F. Heinz, Phys. Rev. Lett. **92**, 177401 (2004).

[139] F. Wang, G. Dukovic, L. E. Brus, and T. F. Heinz, Science **308**, 838 (2005).

[140] S. Berciaud, L. Cognet and B. Lounis, Phys. Rev. Lett. **101**, 077402 (2008).

[141] J. Shaver, J. Kono, O. Portugall, V. Krstic, G. L. J. A. Rikken, Y. Miyauchi, S. Maruyama, and V. Perebeinos, Nano Lett. **7**, 1851 (2007).

[142] A D. Mohite, P. Gopinath, H M. Shah, and B. W. Alphenaar, Nano Lett. **8**, 142 (2008).

[143] T. G. Pedersen, Carbon **42**, 1007 (2004).

[144] V. Perebeinos, J. Tersoff, P. Avouris, Phys. Rev. Lett. **92**, 257402 (2004).

[145] For a review see T. Ando and S. Uryu, Phys. Status Solidi (c) **6**, 173 (2009).

[146] J. Deslippe, C. D. Spataru, D. Prendergast, and S. G. Louie, Nano Lett. **7**, 1626 (2007).

[147] S. Uryu and T. Ando, Phys. Rev. B **76**, 115420 (2007).

[148] E. Malic, J. Maultzsch, S. Reich, and A. Knorr, Phys. Rev. B **82**, 035433 (2010).

[149] J. M. Pereira Jr., V. Mlinar, F. M. Peeters, and P. Vasilopoulos, Phys. Rev. B **74**, 045424 (2006).

[150] J. R. Williams, L. DiCarlo, and C. M. Marcus, Science **317**, 638 (2007).

[151] N. Stander, B. Huard, and D. Goldhaber-Gordon, Phys. Rev. Lett. **102**, 026807 (2009).

[152] A. F. Young and P. Kim, Nature Phys. **5**, 222 (2009).

[153] O. Klein, Z. Phys. **53**, 157 (1929).

[154] A. V. Shytov, M. S. Rudner, and L. S. Levitov, Phys. Rev. Lett. **101**, 156804 (2008).

[155] L. Zhao and S. Yelin, arXiv:0804.2225 (unpublished); Phys. Rev. B **81**, 115441 (2010).

[156] C. W. J. Beenakker, R. A. Sepkhanov, A. R. Akhmerov, and J. Tworzydło, Phys. Rev. Lett. **102**, 146804 (2009).

[157] F. M. Zhang, Y. He, and X. Chen, Appl. Phys. Lett. **94**, 212105 (2009).

[158] T. Ya. Tudorovskiy and A. V. Chaplik, JETP Lett. **84**, 619 (2006).

[159] J. M. Pereira Jr., P. Vasilopoulos, and F. M. Peeters, Appl. Phys. Lett. **90**, 132122 (2007).

[160] M. M. Fogler, D. S. Novikov, L. I. Glazman, and B. I. Shklovskii, Phys. Rev. B **77**, 075420 (2008).

[161] C. W. J. Beenakker, Rev. Mod. Phys. **80**, 1337 (2008).

[162] H. C. Nguyen, M. T. Hoang, and V. L. Nguyen, Phys. Rev. B **79**, 035411 (2009).

[163] M. Y. Han, B. Öezyilmaz, Y. Zhang, and P. Kim, Phys. Rev. Lett. **98**, 206805 (2007).

[164] P. G. Silvestrov and K. B. Efetov, Phys. Rev. Lett. **98**, 016802 (2007).

[165] N. M. R. Peres, J. N. B. Rodrigues, T. Stauber, and J. M. B. Lopes dos Santos, J. Phys.: Condens. Matter **21**, 344202 (2009).

[166] D. W. Horsell, A. K. Savchenko, F. V. Tikhonenko, K. Kechedzhi, I. V. Lerner, and V. I. Fal'ko, Solid State Commun. **149**, 1041 (2009).

[167] Y. -W. Tan, Y. Zhang, K. Bolotin, Y. Zhao, S. Adam, E. H. Hwang, S. Das Sarma, H. L. Stormer, and P. Kim, Phys. Rev. Lett. **99**, 246803 (2007).

[168] P. M. Ostrovsky, I. V. Gornyi, and A. D. Mirlin, Phys. Rev. Lett. **98**, 256801 (2007).

[169] S. Adam, E. H. Hwang, V. M. Galitski, and S. Das Sarma, Proc. Natl. Acad. Sci. U.S.A. **104**, 18392 (2007).

[170] K. Nakada,M. Fujita, G. Dresselhaus, and M. S. Dresselhaus, Phys. Rev. B **54**, 17954 (1996)

[171] K. M. Wakabayashi, H. A. Fujita, and M. Sigrist, Phys. Rev. B **59**, 8271 (1999).

[172] T. O. Wehling, K. S. Novoselov, S. V. Morozov, E. E. Vdovin, M. I. Katsnelson, A. K. Geim, and A. I. Lichtenstein, Nano. Lett. **8**, 173 (2008).

[173] V. V. Cheianov, V. I. Fal'ko, B. L. Altshuler, and I. L. Aleiner, Phys. Rev. Lett. **99**, 176801 (2007).

[174] M. I. Katsnelson, Eur. Phys. J. B **51**, 157 (2006).

[175] J. Tworzydło, B. Trauzettel, M. Titov, A. Rycerz, and C. W. J. Beenakker, Phys. Rev. Lett. **96**, 246802 (2006).

[176] G. Pöschl and E. Teller, Z. Phys. **83**, 143 (1933).

[177] R. R. Hartmann, N.J. Robinson, and M.E. Portnoi, unpublished.

[178] For example, in a finite square well of width d and depth U_0, new zero-energy states appear when $U_0 d/\hbar v_{\rm F} = (2n+1)\pi/2$, where n=$0, 1, 2, \ldots$.

[179] K. S. Novoselov, Z. Jiang, Y. Zhang, S. V. Morozov, H. L. Stormer, U. Zeitler, J. C. Maan, G. S. Boebinger, P. Kim, and A. K. Geim, Science **315**, 1379 (2007).

[180] I. A. Shelykh, M. Rosenau da Costa, and A. C. Seridonio, J. Phys.: Condens. Matter **20**, 164214 (2008), and references therein.

[181] E. Kamke, *Differentialgleichungen - Lösungsmethoden und lösungen* (Chelsea Publishing Company, New York, 1974).

[182] M. Abramowitz, I. A. Stegun, *Handbook of Mathematical Functions with Formulas, Graphs, and Mathematical Tables* (Dover Publications, New York, 1972).